Transfer design via bifurcated retrograde orbits around Phobos

by

Nishanth Pushparaj

Dissertation

submitted to the Department of Space and Astronautical Science

in partial fulfillment of the requirements for the degree of

Doctor of Philosophy

The Graduate University for Advanced Studies, SOKENDAI

February 2022

Acknowledgments

継続は力なり

First and foremost, I thank God almighty for guiding me throughout this quest of completing this thesis. This work is the pinnacle of the three years I spent at the Institute of Space and Astronautical Science, Japan Aerospace Exploration Agency (ISAS/JAXA).

I dedicate this work to my beloved father. If I could travel back in time, I would have tried to be with you, Dad. You were strong; therefore, I am. Even though you left us, your memories have become my heartbeats, so that I will think of you all the time to stay alive. Wholehearted and ineffable gratitude goes to my mom, and brother for their unconditional love, care, prayers and sacrifices.

I want to extend my sincere gratitude to my thesis advisor and supervisor, Prof. Yasuhiro Kawakatsu. Thank you for supporting me, encouraging me, providing me with endless opportunities throughout my time at ISAS, and shaping my research capability. Thank you, sensei, for this chance to be involved and contribute to space mission projects. I am also indebted to Dr. Nicola Baresi for his invaluable advice on my research and career. I thank Dr. Elisabet Canalias and Dr. Regis Bertrand for hosting me as visiting researcher at Centre national d'études spatiales (CNES) to carryout MMX Flight dynamics activities. I thank the department head, Prof. Tadayasu Dotani, for his support. I am incredibly grateful to Funada-san and Fukayama-san for tolerating me and helping me with all academic and research-related administrative works.

I would also like to thank my colleagues, friends and a special mention to present and past members of Kawakatsu laboratory (Naoya, Diogene, Linda, Onur, Ferran,

Roger, Tiago, Shota, Kento, Takuya, Yu, Machii, Daichi and Takuto) for their valuable support throughout. I am very grateful for the care and support by Ito-san, Sayoko-san and Iwamoto-sensei in the past years. Last but not the least, I would like to thank my family and friends from India.

This work is supported by the Ministry of Education, Culture, Sports, Science and Technology (Monbukagakusho) scholarship from the Government of Japan and SOKENDAI Academics Activities Grant. SOKENDAI Student Dispatch Program 2021 provided financial support for my 4-month visiting research stay at the Centre national d'études spatiales (CNES), Toulouse Space Center.

-Nishanth Pushparaj

Abstract

Quasi-satellite orbits (QSOs) or Distant Retrograde Orbits (DROs) are stable retrograde orbits in the restricted three-body problem that have gained attention as a viable candidate for future deep-space missions towards remote planetary satellites. JAXA's robotic sample return mission Martian Moons eXploration (MMX), will utilize QSOs to perform scientific observations of the Martian moon Phobos before landing on its surface and attempting sample retrieval. In comparison to other planetary systems, the dynamical environment around Phobos is distinctive, as a simple two-body approximation with Mars as the main body is not a good approximation in the vicinity of Phobos. Because Phobos' size causes two-body motion to be perturbed during proximity operations, MMX's proximity operations are immensely challenging and require novel and sophisticated techniques for maintaining and transferring between different quasi-satellite orbits.

This thesis uses dynamical systems theory to investigate new transfer design techniques for the proximity operations around the Martian moon Phobos. The developed transfer techniques use bifurcated QSO families to transfer spacecraft between relative QSOs in the Mars-Phobos Hill Problem with ellipsoidal gravity secondary framework. This thesis firstly introduces a systematic approach to compute the bifurcated families of retrograde orbits from in-plane and out-of-plane stability perturbations, namely Multi revolution Periodic QSOs (MP-QSOs) and Spatial QSOs (3D-QSOs). Secondly, geometric characteristics of in-plane bifurcated families of MP-QSOs are leveraged to introduce a novel and robust planar transfer design method. Transfer design strategy via MP-QSOs is explored through transfer maps that illustrate transfer design space between different altitude QSOs. It is found that transfers via MP-QSOs provide insights on minimum ΔV transfers and the parameters determining

the transfer cost between relative QSOs. This transfer methodology provides a basis for robust and stable retrograde transfer trajectories around Phobos. Even if the spacecraft skips the ΔV maneuver at the designated point, the spacecraft remains in the MP-QSO, and crossings occurring later can be used to perform the orbit injection into the target orbit. This method involves two impulse transfers, one to escape the initial QSO and another to insert into the desired lower altitude orbit. The proposed transfer method is explicitly applied to MMX baseline QSOs. Furthermore, these transfer maps deliver accurate initial guesses for optimal transfer trajectories in the vicinity of Phobos. Based on the primer vector analysis of the impulse transfer trajectories, it is found that departing and arriving at the same periphobian sides with an additional mid-course impulse results in the optimal impulse solution.

Later this thesis explores the application of invariant manifolds of unstable retrograde orbits to design out-of-plane transfer trajectories around Phobos to aid high-latitude coverage and scientific observation capabilities to a mission. Computed families of three-dimensional QSOs using out-of-plane bifurcations near planar orbits show that most of these orbits are weak to highly unstable. The invariant manifolds of an unstable 3D-QSO are computed by perturbing the states along the direction of 3D-QSO's local eigenvectors. The intersection of capture and escape trajectories propagated from different locations along candidate 3D-QSOs with an oblate cylinder passing through the two relative planar QSOs are evaluated to extract transfer trajectories connecting a planar and the spatial QSO. This out-of-plane transfer technique provides a baseline to estimate the costs and time-of-flight associated with ballistic dynamics between high-altitude and low-altitude QSOs. The feasibility of using unstable 3D-QSO family members as staging orbits between high-altitude and low-altitude QSOs of MMX mission is later assessed. The final candidates of intermediate 3D-QSOs are ranked based on MMX scientific requirements, transfer analyses, and station-keeping costs by nullifying the growth of orbit injection errors along the unstable eigenvectors of candidate 3D-QSOs.

This work's findings could serve as initial guesses for real-ephemeris implementations to be adopted for the actual MMX mission design. The transfer methodologies and analysis presented in this paper can be extended for future missions that seek lower ΔV transfer opportunities between stable retrograde orbits around Phobos or any small irregular planetary satellites in the solar system.

Contents

List of Figures

List of Tables

1 Introduction

1.1 Exploration of Martian Moons

Deep space missions towards remote planetary satellites such as the Martian moons Phobos and Deimos can provide scientists with invaluable clues on the birth and evolution of our solar system[1, 2]. The origin of the Martian moons is now one of the Solar System's mysteries, as there are inconsistent signs pointing to several interpretations[3, 4]. Exploring the Martian moons would shed light on the formation of these satellites, thereby answering whether Phobos and Deimos are captured type-D asteroids[5, 6] or fragments that interfused after a planetesimal collision with Mars[7, 8]. In terms of mission concepts, Phobos has also been considered as a natural space station that can be utilized by future crewed Martian missions to monitor and control robotic assets on the surface of Mars[9]. Scientific speculations regarding the origin and evolution of the Martian moons have made Phobos and Deimos attractive bodies for space exploration[10]. The curiosity to explore the Martian moons served as a catalyst for several spacecraft missions that would supposedly land on Phobos.

Unfortunately, all of these attempts failed while either en route or in the vicinity of the Martian moon, leaving the mystery of their origin unsolved. Initially, two

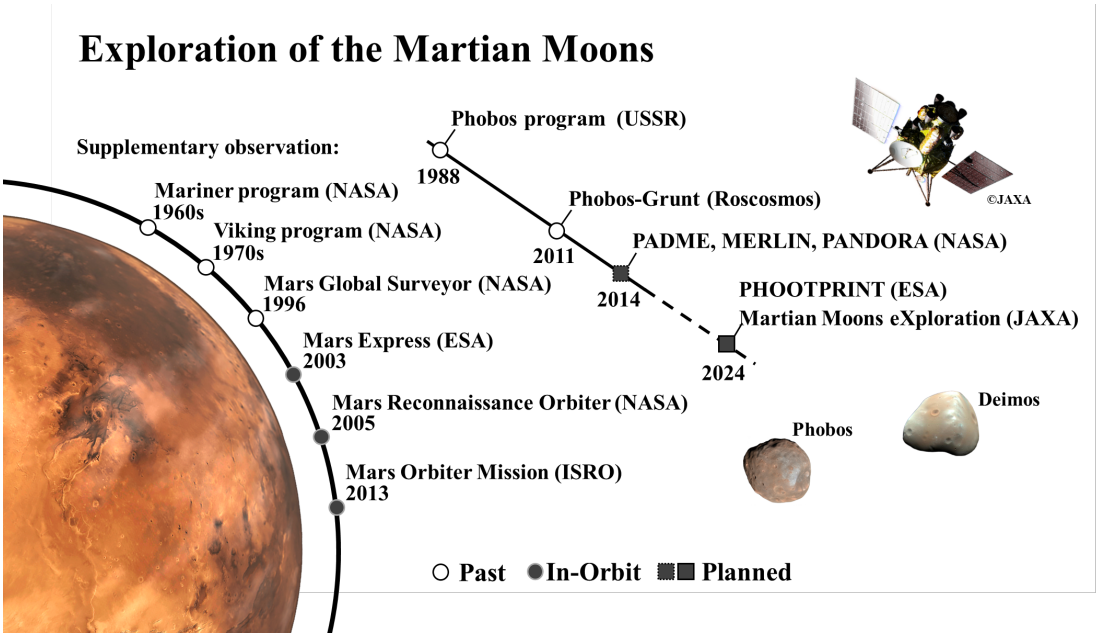

Figure 1.1: Missions to Martian Moons.

space missions from the Soviet Phobos programs (Phobos 1 and Phobos 2) were launched in 1988 to explore the Martian moon. Both missions, however, failed to achieve their objectives[1]. Due to a glitch in the attitude control system, Phobos 1 was lost along its interplanetary route, while Phobos 2 failed before deploying two rovers over the moon's surface. Despite this partial failure, Phobos 2 captured several pictures of the Martian moon before its fatal collapse[11]. Following the failure of the Phobos programs, the Russian spacecraft Phobos-Grunt was launched to return a sample from Phobos' surface[12, 13]. Despite the mission's failure due to a propulsion system problem along its interplanetary trajectory, the impact of Phobos-Grunt has inspired future missions (Fig. 1.1) to the Martian moons such as MMX (Martian Moons eXploration)[14]and other mission proposals like NASA's PADME (Phobos and Deimos and Mars Environment)[15], MERLIN (Mars-Moons Exploration, Reconnaissance, and Landed Investigation)[16], PANDORA (Phobos AND Deimos ORigin Assessment)[17] and the European Space Agency's DePhine (Deimos and Phobos Interior Explorer)[18],

[1] https://nssdc.gsfc.nasa.gov/planetary/phobos.html

PHOOTPRINT[2] (Phobos Sample Return Mission)[19].

The Martian Moons eXploration (MMX) mission is a robotic sample return spacecraft proposed by the Japan Aerospace eXploration Agency (JAXA)[20]. The goal of MMX is to characterize Phobos' dynamical and geophysical environments and return samples from its surface back to Earth by 2029, thereby providing insights into the origin of Martian moons and the evolution of Mars and other small bodies in the Solar system. The current mission plan of MMX involves an interplanetary phase followed by a Mars orbit insertion phase, a Phobos proximity phase, and surface operations to perform descent and landing operations[21, 22, 23]. The mission profile of the MMX mission is illustrated in Fig. 1.2, revealing how upon arrival, the spacecraft will be inserted into a series of retrograde relative orbits around the Martian moon and carry out its scientific observations for more than three years. The dynamical environment around Phobos is unique compared to other planetary systems[24]. MMX envisions utilizing quasi-satellite orbits (QSO) to characterize the dynamical environment of Phobos for adequate landing site selection and relatively safe spacecraft operations[20].

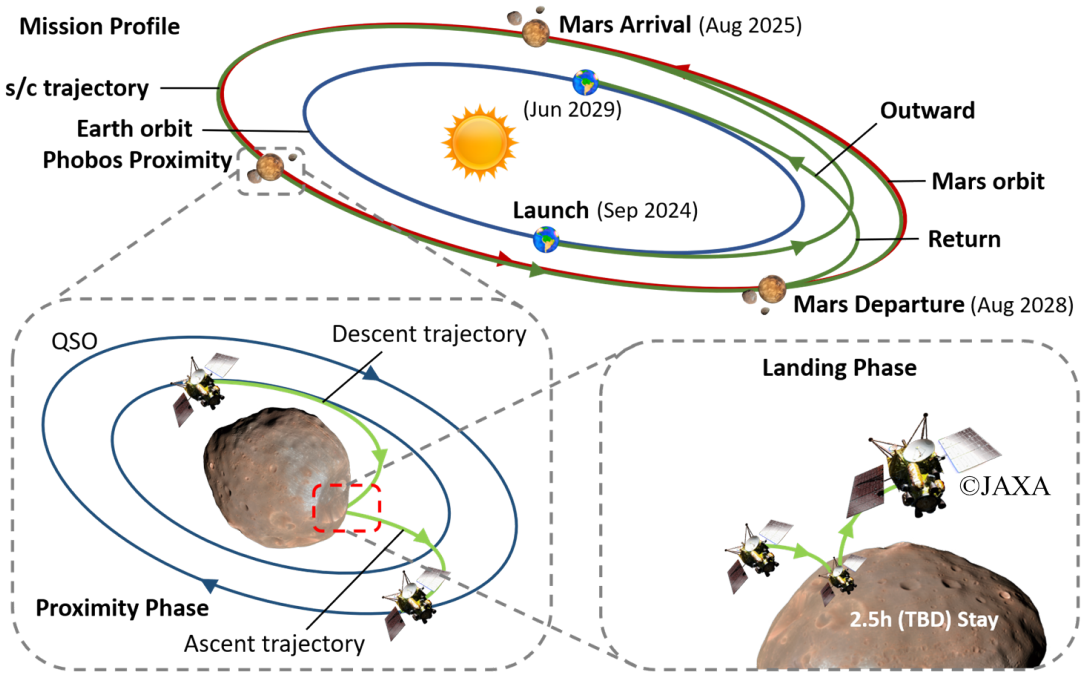

Figure 1.2: Martian Moons eXploration Mission Profile.

[2] https://sci.esa.int/s/AGdXJLw

1.2 Quasi-satellite Orbits

Quasi-satellite Orbits (QSOs) are a type of co-orbital 1:1 resonant motion where a spacecraft orbits the primary body (m_1) perturbed by the secondary body (m_2) such that it follows an almost elliptic retrograde trajectory centered to the secondary body in a synodic frame as illustrated in Fig. 1.3. In some literature, QSOs have been referred to as Distant Retrograde Orbits (DROs) in the Circular Restricted Three-Body Problem (CRTBP)[25, 26, 27, 28, 29], and also the family 'f' of periodic orbits by Hénon in his numerical analyses of the circular Hill problem[30, 31, 32]. They are stable three-body orbits that demand lower orbit maintenance costs over long mission periods[33, 34].

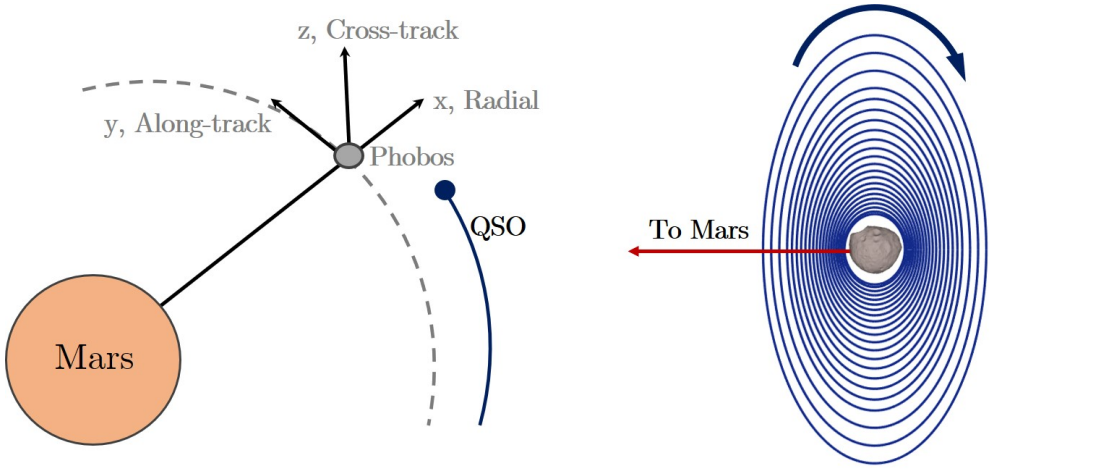

a) Mars-Phobos-QSO Illustration (Mars-centered frame)

b)Relative QSOs around Phobos (Phobos-centered frame)

Figure 1.3: Quasi-satellite orbits.

In the case of the Mars-Phobos system, Phobos has a sphere of influence embedded within its surface due to its smaller mass, density, and proximity to Mars. A simple two-body approximation with Mars is not appropriate to describe the dynamics in the vicinity of Phobos. Indeed, the size of the Martian moon is enough to perturb two-body motion during the proximity phase and make spacecraft operations quite challenging. Therefore to ensure the safe operation of the spacecraft in the proximity of Phobos for a more extended mission period, it is required to consider the three-body problem. Also, due to the proximity of the Mars-Phobos Lagrangian points L_1 and L_2 to the surface of Phobos, collinear point orbits such as Halo, Lyapunov, and Lissajous

orbits are unsafe and practically undesirable for prolonged proximity operations around Phobos[35]. In this case, Quasi-Satellite Orbits (QSOs) are unquestionably the best option to exploit the proximity of the Martian Moon. Alternate orbits to explore Phobos, including liberation point orbits, are systematically studied by Zamaro and Biggs[36].

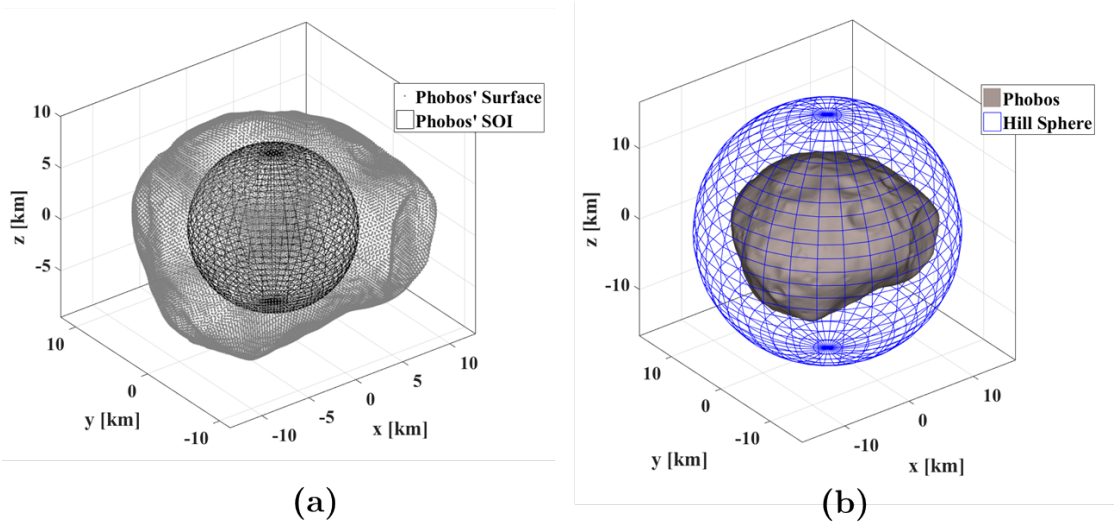

Figure 1.4: Dynamics around Phobos.

Following Hénon, a number of studies have investigated the properties of QSOs and leveraged their stable nature for several mission proposals. Previously, transfers to QSO from Low Earth Orbits using the manifolds of collinear equilibrium point orbits of the Sun-Earth CRTBP have been studied by Scott and Spencer[37, 38], and in the framework of Earth-Moon CRTBP by Capdevila et al.[39], Mingotti et al.[40], Demeyer and Gurfil[41], and Oshima and Yanao[42]. Low-energy transfers from Lyapunov orbits around cis-lunar Lagrangian points to QSO were studied by Ming and Shijie[43]. Parrish et al.[44] adopted low-thrust propulsion for transfers between a QSO and an L_2 halo orbit of the Earth-moon system. Lam and Whiffen[45] studied the stability of QSO, proposing different transfers between different altitude QSOs using either impulsive or low-thrust propulsion. They applied this strategy to both the Jupiter-Europa and Jupiter-Ganymede systems, thereby showing examples of low-thrust trajectories from retrograde relative orbits around the two Jovian moons[46]. Despite the number of studies that can be found in the literature, the problem of finding and implementing

appropriate transfer techniques between relative planar QSOs, planar to 3D-QSOs, and from Planet-centric orbits to QSOs are still open to debate.

To this end, Russell introduced primer vector theory and low-thrust trajectories to maneuver satellites between QSOs in the Jupiter-Europa and Earth-Moon systems[47]. Ichinomiya et al.[48] applied Lam and Whiffen's[45] approach to design transfers between planar QSOs in the Mars-Phobos CRTBP. Transfers between planar and spatial QSOs were only studied by Canalias et al.[49], whereby single impulsive maneuvers were implemented in order to insert from mid-altitude QSOs into their spatial and out-of-plane counterpart. The goal of this thesis is to address on the transfer design problem between the relative retrograde orbits. In particular, introducing transfer methodologies based on in-plane and out-of-plane bifurcations of relative retrograde orbits in the framework of Circular Hill Problem (HP) with an ellipsoidal secondary[50, 51].

1.3 Bifurcation theory approach

In-plane and out-of plane bifurcations of periodic orbits were first studied by Robin and Markellos[52]. Later, Lara et al.[53] used similar bifurcation methods to explore distant stability regions around Europa. Vaquero and Howell[54] designed 3D resonant orbits bifurcating from planar resonant periodic families in the Sun-Earth CRTBP. Oshima and Yanao[42] applied the same bifurcation theory to calculate spatial QSOs (3D-QSOs) and study their application in the bi-circular four-body problem of Sun-Earth-Moon system. As a different application, they also considered ballistic landings on Phobos. More recently, Chen et al.[55] studied the effective stability of bifurcated 3D-QSOs for Phobos exploration. Differently from previous research, we leverage the resonant type bifurcation approach to develop bifurcated families of QSOs and utilize them to design transfer trajectories connecting relative QSOs in the proximity of Phobos. This thesis introduces two transfer methodologies: 1) In-plane transfer method using Multi-Revolution Periodic QSOs (MP-QSOs) or Swing-QSOs. 2) Out-of-plane transfer method using the invariant manifolds of Spatial QSOs (3D-QSOs). These proposed transfer strategies provide us with a better understanding of retrograde transfer trajectories, i.e., minimum ΔV execution points, and time of flight around Phobos. Furthermore, it delivers proper initial guesses for real-ephemeris implementations that

could be adopted for the actual mission design.

1.4 Thesis outline

Chapter 2 begins with a brief overview of dynamical systems theory techniques used to compute periodic orbit families, including gravity and dynamical models, continuation methods, and terminologies used throughout the thesis. We also review the concepts of stability, bifurcations, and manifold theory to develop some of the quantitative and qualitative numerical procedures included in this research.

Chapter 3 of this thesis deals with the numerical procedures adopted to systematically compute families of bifurcated distant retrograde orbits (DROs) or QSOs. Firstly, the continuation methods introduced in the previous chapter are used to evaluate in-plane and out-of-plane bifurcations along the planar families of QSOs. Further stability analysis and the applicability of these bifurcated orbits for Phobos exploration are discussed later.

Chapters 4 and 5 introduce novel relative proximity transfer techniques utilizing these computed families of bifurcated retrograde orbits. Firstly, we utilize horizontal bifurcated Multi-revolution Periodic QSOs (MP-QSOs) to design planar transfer trajectories between relative QSOs. Secondly, we leverage invariant manifolds of vertical bifurcated Spatial QSOs (3D-QSOs) to connect relative QSOs. These transfer techniques are applied to the MMX mission candidate orbits by using the Mars-Phobos system as an example.

Finally, Chapter 6 summarizes the contributions and outcomes of the thesis, and discusses possible future directions.

1.5 Contributions and Publications

The key contributions of this research are itemized and summarized in this section.

- Systematic numerical computation of bifurcated families of retrograde orbits:
  - Computation of lower altitude QSOs using differential corrector techniques.
  - Bifurcation and stability analysis to produce in-plane and out-of-plane QSOs.

- In-plane transfer method:
  - > In-plane bifurcated QSO families (MP-QSOs) are explored for transfer design between QSOs around Phobos.
  - > 2D Transfer maps are introduced to visualize the design domain between QSOs.
  - > ΔV of the transfer is defined by geometrical parameters that minimize transfer costs.
  - > Transfer maps provide a basis for optimizing retrograde transfer trajectories of MMX mission.
  - > Transfer trajectories are optimized using impulsive primer vector theory.
- Out-of-plane transfer method:
  - > Transfer methodology using the invariant manifolds of unstable 3D-QSOs is proposed.
  - > Feasibility of spatial retrograde orbits for the Phobos exploration is studied.
  - > Transfer design via 3D-QSOs between MMX candidate QSOs enables high-latitude observations of Phobos' surface.

Published works from this thesis include:

Journals

1. N. Pushparaj, N. Baresi, and Y. Kawakatsu, "Transfers and orbital maintenance of spatial retrograde orbits for Phobos exploration," Acta Astronautica, 189, 452-464, 2021. DOI: 10.1016/j.actaastro.2021.09.008
2. N. Pushparaj, N. Baresi, K. Ichinomiya, and Y. Kawakatsu, "Transfers around Phobos via bifurcated retrograde orbits: Applications to Martian Moons eXploration mission," Acta Astronautica, 181, 70-80, 2021. DOI: 10.1016/j.actaastro.2021.01.016

Conferences

1. N. Pushparaj, N. Baresi, and Y. Kawakatsu, "Optimal Transfer Trajectory Analysis of Relative QSOs around Phobos," 33rd International Symposium on Space Technology and Science (ISTS), February-March 2022, Oita, Japan.

2. N. Pushparaj, and Y. Kawakatsu, "Bifurcated Quasi-Satellite Orbits for Martian Moons eXploration (MMX)," 33rd International Symposium on Space Technology and Science (ISTS), February-March 2022, Oita, Japan.

3. N. Pushparaj, N. Baresi, and Y. Kawakatsu, "Martian Moons eXploration transfer analysis between planar and spatial QSOs around Phobos," 72nd International Astronautical Congress, 25-29 October 2021, Dubai, UAE.

4. N. Pushparaj, N. Baresi, and Y. Kawakatsu, "Phobos proximity orbital transfer analysis with applications to MMX mission," 31st Workshop on JAXA Astrodynamics and Flight Mechanics, July 2021, ISAS/JAXA, Sagamihara, Japan.

5. N. Pushparaj, N. Baresi, and Y. Kawakatsu, "Transfers around Phobos using invariant manifolds of unstable Quasi-Satellite Orbits," 71st International Astronautical Congress, 12-14 October 2020, CyberSpace Edition.

6. N. Pushparaj and Y. Kawakatsu, "Exploration of Phobos Using Bifurcated Distant Retrograde Orbits: Application to MMX," ISAS Planetary Exploration Workshop, 9 September 2020, ISAS/JAXA, Sagamihara, Japan.

7. N. Pushparaj, N. Baresi, and Y. Kawakatsu, "Transfers via bifurcated Quasi-satellite Orbits around Phobos: Applications to MMX," 30th Workshop on JAXA Astrodynamics and Flight Mechanics, July 2020, ISAS/JAXA, Sagamihara, Japan.

8. N. Pushparaj, N. Baresi, and Y. Kawakatsu, "Design of Transfer Trajectories Between Planar and Spatial Quasi-Satellite Orbits," AIAA SciTech Forum 2020, 6-10 January 2020, Orlando, USA.

9. N. Pushparaj, N. Baresi, and Y. Kawakatsu, "Transfers around Phobos using Multi-Periodic Quasi-Satellite Orbits," 29th Workshop on JAXA Astrodynamics and Flight Mechanics, July 2019, ISAS/JAXA, Sagamihara, Japan.

10. N. Pushparaj, N. Baresi, K. Ichinomiya, and Y. Kawakatsu, "Multi-Revolutional Periodic Orbit Transfers in the Ellipsoidal Gravity Field of Phobos," 32nd International Symposium on Space Technology and Science (ISTS), June 2019, Fukui, Japan.

2

Background

2.1 Introduction

This chapter outlines the dynamical and gravity models, continuation methods, and terminologies used in each chapter and throughout the thesis. Specifically, the gravity field of a small body is modeled with the constant density ellipsoid. The dynamics around a small body are modeled with the Hill problem (HP), including the secondary's ellipsoidal gravity. Furthermore, it is helpful to review the concepts of stability, bifurcations, and manifold theory to develop some of the quantitative and qualitative procedures included in this research to understand better the methodologies used to design transfer trajectories in this thesis. The procedures presented here are focused on Martian moon Phobos, but they can be applied to any small irregular planetary satellites in the solar system by changing the physical parameters.

2.2 Dynamical Models

2.2.1 Hill problem

The motion of a particle in the vicinity of a planetary satellite can be defined using the equations of the classical circular restricted three-body problem (CRTBP)[56]. The general three-body problem considers the trajectories of three arbitrary massive bodies (Primary, Secondary, and particle) traveling under mutual gravitation. The motion of a particle (a Spacecraft) in the vicinity of a secondary body (e.g., planetary satellite) can also be described with the Hill Problem (HP) due to the smaller mass ratio of primary-secondary systems and the smaller spacecraft-secondary distance[57].

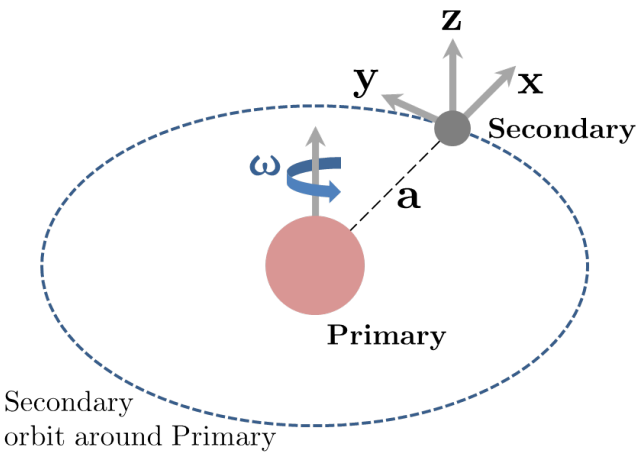

Figure 2.1: Hill Problem.

The Hill Problem's equations of motion are defined in a rotating reference frame centered at the secondary's barycenter as shown in Fig. 2.1, where, x-axis parallel to the line connecting the primary and secondary bodies, the z-axis parallel to the orbital angular momentum vector, and the y-axis in the direction of orbital velocity of the secondary. The equations of motion of Hill Problem in dimensional form[57]:

$$\begin{cases} \ddot{x} - 2\omega_s \dot{y} &= -(\mu_s/r^3)\, x + 3\omega_s^2\, x, \\ \ddot{y} + 2\omega_s \dot{x} &= -(\mu_s/r^3)\, y, \\ \ddot{z} &= -(\mu_s/r^3)\, z - \omega_s^2\, z, \end{cases} \tag{2.1}$$

where, $r = \sqrt{x^2 + y^2 + z^2}$ is the distance from the centre of coordinate frame, μ_s is the gravitational parameter of the secondary body, ω_s is the mean motion of the secondary body. Normalizing Eq. (2.1) to generalize the results, the length and time units are scaled such that both ω_s and $(\mu_s/\omega_s^2)^{(1/3)}$ are equal to 1. Normalized equations of motion of the third body (spacecraft) reduces to classical Hill's equations:

$$\begin{cases} \ddot{x} - 2\dot{y} &= -(x/r^3) + 3\,x, \\ \ddot{y} + 2\dot{x} &= -(y/r^3), \\ \ddot{z} &= -(z/r^3) - z, \end{cases} \tag{2.2}$$

2.2.2 Ellipsoidal gravity model

The general problem of a mass particle subject to the gravitational attraction of a host planet and a uniformly rotating tri-axial ellipsoid with constant density is hereby considered. The tri-axial ellipsoidal model of Phobos can be formulated by specifying the physical parameters of the Martian moon as follows. Three major axes are defined, including the larger semi-major axis along the x-axis of the Mars-Phobos synodic frame, the intermediate semi-major axis along the y-axis, and the smallest semi major axis along the z-axis of the rotating coordinate frame. The irregular gravity field of Phobos can be approximated using an ellipsoidal model with three major axes: α, β, and γ as shown in Fig. 2.2.

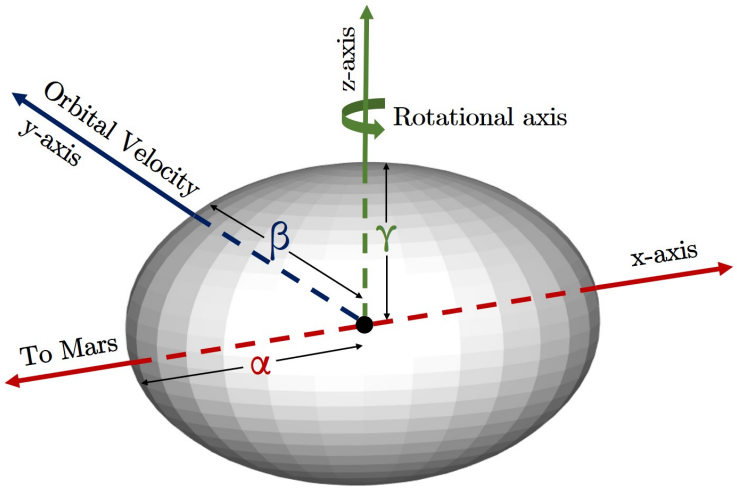

Figure 2.2: Tri-axial ellipsoid $\gamma \leq \beta \leq \alpha$

Assuming constant density σ_P, the gravitational parameter of Phobos is computed as in [58, 59]:

$$\mu_P = \frac{4\pi}{3} G\sigma_P \alpha\beta\gamma, \tag{2.3}$$

where G, is gravitational constant 6.674×10^{-8} $\mathrm{cm^3 g^{-1} s^{-2}}$ and $\frac{4\pi}{3}\alpha\beta\gamma$ is the volume of the ellipsoid. The gravitational potential of a constant density tri-axial ellipsoidal Phobos modelled at a point x, y, z is

$$\mathcal{U}(x, y, z) = -\mu_P \frac{3}{4} \int_0^\infty \phi(x, y, z, u) \frac{dl}{\Delta(l + \Lambda)}, \tag{2.4}$$

where

$$\phi(x, y, z, l + \Lambda) = \frac{x^2}{\alpha^2 + l + \Lambda} + \frac{y^2}{\beta^2 + l + \Lambda} + \frac{z^2}{\gamma^2 + l + \Lambda} - 1, \tag{2.5}$$

$$\Delta(l + \Lambda) = \sqrt{(\alpha^2 + l + \Lambda)(\beta^2 + l + \Lambda)(\gamma^2 + l + \Lambda)}. \tag{2.6}$$

Notice that μ_P is gravitational parameter of Phobos, whereas Λ is either zero or the real positive root of $\phi(x, y, z, l + \Lambda) = 0$ depending on whether the gravitational attraction is computed internally or outside the body, and l is the integration variable. Physical properties of Phobos are provided in Table 2.1[60].

Table 2.1: Phobos physical properties

Properties	Values
α, Largest semi-major axis	13.03 km
β, Intermediate semi-major axis	11.4 km
γ, Smallest semi-major axis	9.14 km
σ_P, Density	1.860 g/cm^3
μ_P, Gravitational Parameter	0.000706 km^3/s^2
M_P, Mass	1.058×10^{16} kg
a_P, Phobos semi-major axis	9377 km
P_P, Rotational period	7.66 hrs

2.2.3 Hill Problem with ellipsoidal gravity

In addition to the simplified Mars-Phobos HP point mass model, this thesis considers the HP ellipsoidal gravity model. Noting that the gravitational parameter of Phobos

(Table 2.1) is significantly smaller than the gravitational parameter of Mars, if we assume that the relative distance between the spacecraft and Phobos is significantly smaller than the distance between Mars and its moon, the differential equations governing the motion of mass particles around Phobos can be well approximated with the equations of the circular Hill problem [57] from Eq. (2.2):

$$\begin{cases} \ddot{x} - 2\dot{y} &= g_x + 3\,x, \\ \ddot{y} + 2\dot{x} &= g_y, \\ \ddot{z} &= g_z - z, \end{cases} \tag{2.7}$$

where μ_s/r^3 term from Eq. (2.1) is simply replaced with three components of gravitational accelerations g_x, g_y, and g_z due to an attracting ellipsoidal mass [57]:

$$g_x = -\frac{3}{2}\mu_P x \int_0^\infty \left(\frac{1}{\alpha^2 + l + \Lambda}\right)\frac{dl}{\Delta(l+\Lambda)}, \tag{2.8a}$$

$$g_y = -\frac{3}{2}\mu_P y \int_0^\infty \left(\frac{1}{\beta^2 + l + \Lambda}\right)\frac{dl}{\Delta(l+\Lambda)}, \tag{2.8b}$$

$$g_z = -\frac{3}{2}\mu_P z \int_0^\infty \left(\frac{1}{\gamma^2 + l + \Lambda}\right)\frac{dl}{\Delta(l+\Lambda)}. \tag{2.8c}$$

where $\mathbf{X} = [x, y, z, \dot{x}, \dot{y}, \dot{z}]^T$ represents the state of third body in normalized units, i.e., 1 $LU = \epsilon\, a_P = 23.86$ km, 1 $TU = 1/n_P = 4387.63$ s, where $\epsilon = (\mu_P/\mu_M)^{1/3}$, a_P is the semi-major axis of Phobos, and n_P is the mean motion of the Martian moon, respectively. Notice that Eq. (2.4) and (2.8) depends on elliptic integrals that can be calculated through standard numerical procedures as in Ref. [61].

Finally, observe that the equations of motion (2.7) admits an energy-like integral of motion known as the *Jacobi integral*:

$$C = \mathcal{W}(\boldsymbol{r}) - \frac{1}{2}\,(\dot{x}^2 + \dot{y}^2 + \dot{z}^2), \tag{2.9}$$

where $\mathcal{W}(\boldsymbol{r}) = \frac{1}{2}\,(3\,x^2 - z^2) + \mathcal{U}(\boldsymbol{r})$ is the effective potential of the system. Since $\mathcal{T} = \frac{1}{2}\,(\dot{x}^2 + \dot{y}^2 + \dot{z}^2) = \mathcal{W} - C \geq 0$, the Jacobi integral divides the vicinity of Phobos in areas of forbidden and admissible motion. That is, for each value of C, $\mathcal{W} - C = 0$ defines a zero-velocity curve that cannot be crossed by any spacecraft with the same Jacobi

integral value. Figure 2.3 shows the zero-velocity curves for the circular HPe, as well as the L_1 and L_2 Lagrangian points found along the Mars-Phobos line (at $x_{L_1} = -17.34$ km and $x_{L_2} = 17.34$ km, respectively, $C_{L_1} = C_{L_2} = 66.04\ m^2/s^2 = 2.23\ LU^2/TU^2$). As it can be seen, the Lagrangian points are just a few kilometers above the surface of Phobos and are known to be unstable [24].

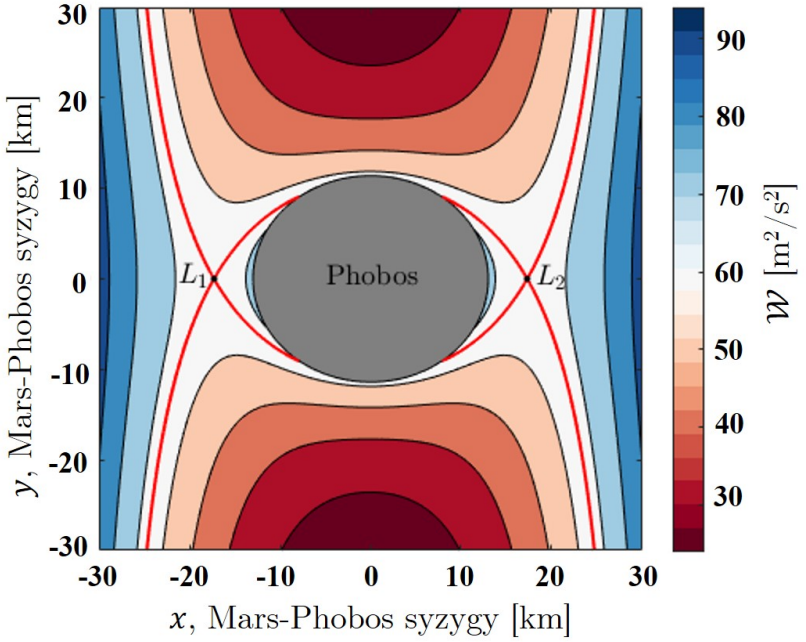

Figure 2.3: Zero-velocity curves calculated in the circular Hill problem around Phobos.

Symmetries in Hill Problem

The circular Hill problem exhibits two types of symmetries, with respect to the xy-plane and x-axis, respectively [56]. The symmetric properties of the circular Hill problem are depicted in Fig. 2.4.

(a) If a trajectory flows away from the plane y = 0, a mirror image of that trajectory continues to flow backward in time on the other side of the plane (i.e., if an initial trajectory flows away from the plane y = 0, the mirror trajectory flows towards it).The two symmetric trajectories in Fig. 2.4(a) are two parts of the same trajectory.

(b) A mirror symmetry exists across the z = 0 plane in addition to the time-reversal symmetry across the y = 0 plane as illustrated in Fig. 2.4(b).

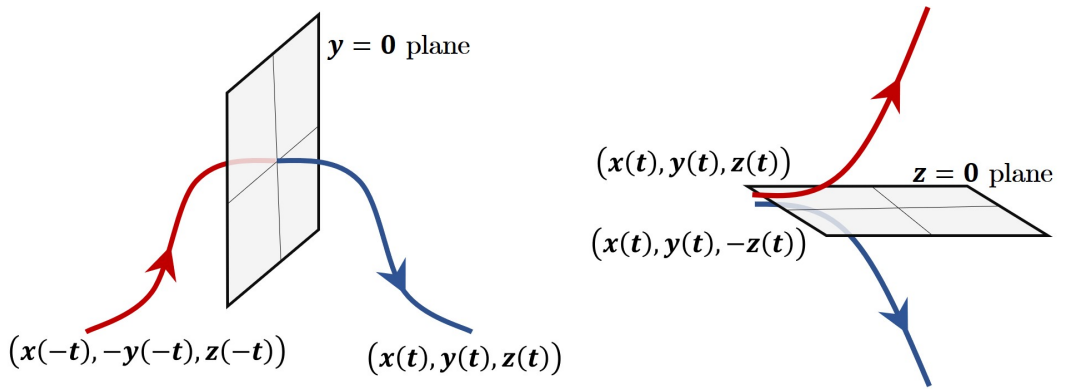

a) Symmetry across the y = 0 plane. b) Symmetry across the z = 0 plane.

Figure 2.4: Symmetries in the circular Hill problem.

These two symmetries can be coupled to form another symmetry with both symmetric properties. It is also worth noting that Eq. (2.7) is invariant under the following transformations:

- $[x, y, z, \dot{x}, \dot{y}, \dot{z}, t] \rightarrow [x, -y, z, -\dot{x}, \dot{y}, -\dot{z}, -t]$, when $y = -y, t = -t$
- $[x, y, z, \dot{x}, \dot{y}, \dot{z}, t] \rightarrow [x, -y, -z, -\dot{x}, \dot{y}, \dot{z}, -t]$, when $y = -y, z = -z, t = -t$.

Periodic orbits can be found using the time-reversal symmetry across the y = 0 plane. Assume that a trajectory crosses the y = 0 plane twice in a perpendicular direction. The trajectory will mirror before the last crossing, returning to the state at the first crossing, eventually resulting in a closed trajectories (plane-symmetric periodic orbit). The following section discusses numerical procedures for computing periodic orbits and their associated families.

2.3 Periodic Orbits

In dynamical systems theory, periodic orbits are defined as trajectories that repeat over a certain period of time. Let $\boldsymbol{x_0} = [x_0, y_0, z_0, \dot{x}_0, \dot{y}_0, \dot{z}_0]^T$ and T be the initial state vector and time of flight of a spacecraft. The fundamental problem of computing a

periodic orbit is finding a set of variables $\boldsymbol{X} \equiv [\boldsymbol{x_0}, T]^T \in \mathbb{R}^{7\times1}$that satisfies periodicity and phase conditions[62, 63]. Fig. 2.6 illustrates the periodic and phase constraints to compute a periodic orbit. Periodicity condition ensures that the propagated orbit is periodic, such that the initial state vector propagated over a time T coincides with the final state at a specific time. Periodicity condition can be conventionally expressed as

$$\boldsymbol{\varphi}(\boldsymbol{x_0}, 0, T) - \boldsymbol{x_0} = \boldsymbol{0} \in \mathbb{R}^{6\times1}, \tag{2.10}$$

where $\boldsymbol{\varphi}(\boldsymbol{x_0}, 0, T)$ is a terminal state vector propagated from $\boldsymbol{x_0}$ between initial and final times $t = 0$ and $t = T$.

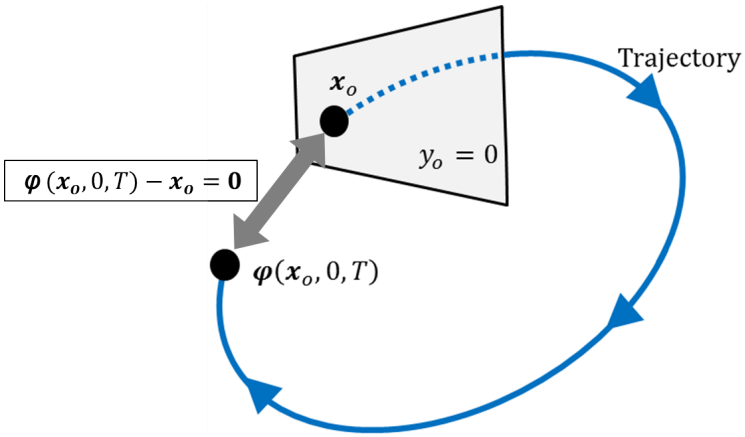

Figure 2.5: Schematic of periodicity and phase constraints.

It's worth noting that number of variables is one more than the constraints defined by the Eq. (2.10). As a result, we add a constraint that fixes the phase of $\boldsymbol{x_0}$, allowing $\boldsymbol{x_0}$ to be found only once on the periodic orbit. Phase constraint of a periodic orbit is defined by

$$p(\boldsymbol{x_0}) = \boldsymbol{0} \in \mathbb{R}^{1\times1}, \tag{2.11}$$

Combining Eq. (2.10) and Eq. (2.11), equation to find periodic solution is derived as

$$F(\boldsymbol{X}) \equiv \begin{bmatrix} \boldsymbol{\varphi}(\boldsymbol{x_0}, 0, T) - \boldsymbol{x_0} \\ p(\boldsymbol{x_0}) \end{bmatrix} = \boldsymbol{0} \in \mathbb{R}^{7\times1}, \tag{2.12}$$

Suitable predictor-corrector schemes can be used to trace continuous periodic family solutions that account for changes in $\boldsymbol{x_0}$ and T along the curve representing the

periodic orbit family in the $(\boldsymbol{x_0}, T)$ plane. The predictor-corrector method proposed by Seydel[64] is considered in this work and outlined in the following subsections to provide a unique solution for Eq. (2.12).

2.3.1 Predictor: Pseudo-arclength continuation

In this thesis, we use the pseudo-arclength continuation method predictor step as described in Ref.[65] to develop families of periodic orbits.

Let $\tilde{\boldsymbol{X}}$ be a solution of $F(\boldsymbol{X}) = 0$, $\tilde{X}'$ be the unit tangential vector to the curve at $\tilde{\boldsymbol{X}}$, and δs defines prediction step size as shown in Fig. 2.6. Then, a first guess for the next correction step $\boldsymbol{X_{fg}}$ can be obtained along $\tilde{X}'$ as:

$$\boldsymbol{X_{fg}} = \tilde{\boldsymbol{X}} \pm \delta s \tilde{X}', \tag{2.13}$$

Pseudo-arclength continuation scheme constraints to the solution guess $\boldsymbol{X_g}$ can be defined by

$$(\boldsymbol{X_g} - \tilde{\boldsymbol{X}})^T \tilde{X}' - \delta s = 0, \tag{2.14}$$

Schematic of pseudo-arclength continuation process is depicted in Fig. 2.6, whereby the predictor creates a first guess at the next correction step $\boldsymbol{X_{fg}}$ along $\tilde{X}'$ with a specific step size δs. The guess $\boldsymbol{X_g}$ is then iteratively corrected with a constraint Eq. (2.14) on the orthogonal hyperplane to $\tilde{X}'$ indicated as a green line in Fig. 2.6.

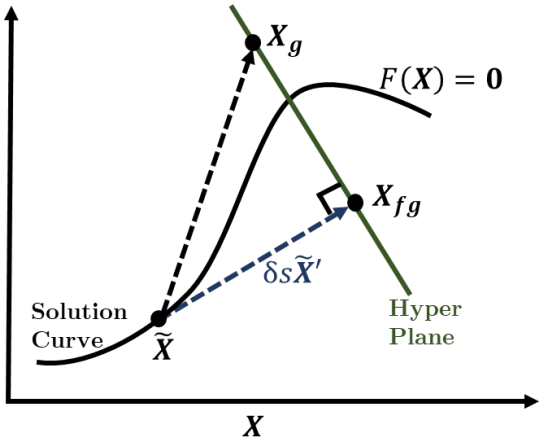

Figure 2.6: Schematic of pseudo-arclength continuation.

The variable δs is a small parameter (e.g., $\delta s = 10^{-4}$), whose magnitude can be adjusted throughout the continuation process to control the number of family members being computed.

2.3.2 Corrector: Shooting method

The equation to be solved to correct the periodic orbits is derived by incorporating the pseudo-arclength continuation[65] constraint Eq. (2.14) with periodic and phase conditions Eq. (2.13).

$$F(\boldsymbol{X}) \equiv \begin{bmatrix} \boldsymbol{\varphi}(\boldsymbol{x_0}, 0, T) - \boldsymbol{x_0} \\ p(\boldsymbol{x_0}) \\ (\boldsymbol{X_g} - \tilde{\boldsymbol{X}})^T \tilde{X}' - \delta s \end{bmatrix} = \boldsymbol{0}. \tag{2.15}$$

Even though $(\boldsymbol{x_0}, T)$ from the predictor step is only a projected values, it is indeed unlikely that each of Eq. (2.15)'s constraints are satisfied. The predicted solution is, however, close to the true solution; Newton's method can be used to numerically iterate the predicted solution until the Eq. (2.15) converges to zero or close to a tolerance margin. Now, defining $\Delta \boldsymbol{X}$ as the correction vector of $\boldsymbol{X_g}$, the objective function at the next guess can be given by first order Taylor's expansion:

$$F(\boldsymbol{X_g} + \Delta \boldsymbol{X}) = F(\boldsymbol{X_g}) + \frac{\partial F(\boldsymbol{X_g})}{\partial X_g} \Delta \boldsymbol{X} + H.O.T. \tag{2.16}$$

where $\frac{\partial F}{\partial X_g}$ is the Jacobian and expressed as:

$$\frac{\partial F(\boldsymbol{X_g})}{\partial X_g} = \begin{bmatrix} \frac{\partial \varphi}{\partial \boldsymbol{x_0}} & \dot{\boldsymbol{\varphi}}(\boldsymbol{x_0}, 0, T) \\ \frac{\partial p(\boldsymbol{x_o})}{\partial \boldsymbol{x_0}} & 0 \\ \tilde{X}'^T_{\boldsymbol{x_0}} & \tilde{X}'^T_{\boldsymbol{T}} \end{bmatrix} \tag{2.17}$$

where $\frac{\partial \varphi}{\partial \boldsymbol{x_0}}$ corresponds to the state transition matrix (STM) from $\boldsymbol{x_0}$ to $\boldsymbol{\varphi}(\boldsymbol{x_0}, 0, T)$. STM after one orbital period is also known as Monodromy matrix, M, which helps analyze the stability of the computed periodic orbits in the next section. $\tilde{X}'^T_{\boldsymbol{x_0}}$ and $\tilde{X}'^T_{\boldsymbol{T}}$ are components of $\tilde{X}'$ updating $\boldsymbol{x_0}$ and T, respectively.

On eliminating the higher order terms from Eq. (2.18), periodic solution $F(\boldsymbol{X})$ is converged by iteratively updating the $\Delta \boldsymbol{X}$ vector.

$$\Delta X = -\left(\frac{\partial F(X_g)}{\partial X_g}\right)^{-1} F(X_g) \tag{2.18}$$

Upon convergence, the algorithm solves the boundary value problem, which allows the predictor-corrector scheme to be reinitialized and continue along the branch of the periodic orbit family.

2.3.3 Periodic orbits in the vicinity of Phobos

A central manifold characterized by families of periodic orbits and quasi-periodic orbits exists around each of the collinear liberation points L_1 and L_2 in the Hill Problem framework. Periodic families around liberation points L_1 and L_2 are planar Lyapunov, vertical Lyapunov, northern and southern halo orbit families. Fig. 2.7 to Fig. 2.9 illustrate the families of liberation point orbits computed using pseudo-arclength continuation and shooting methods described in the previous subsections.

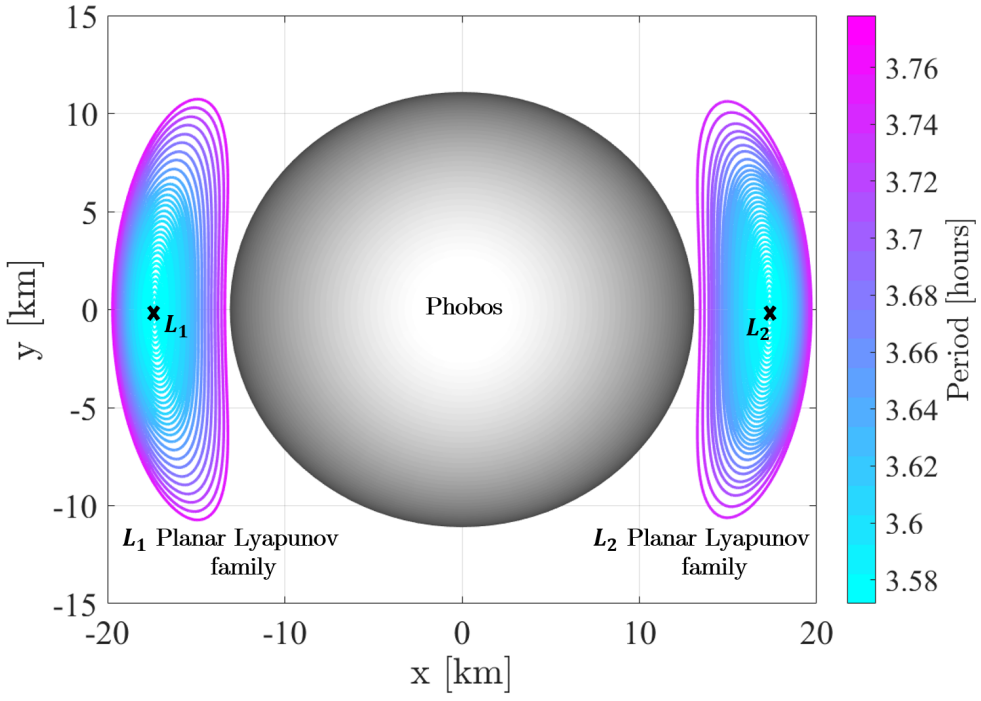

Figure 2.7: Dynamics around Mars-Phobos Lagrangian points: Planar Lyapunov Orbit families around L_1 and L_2.

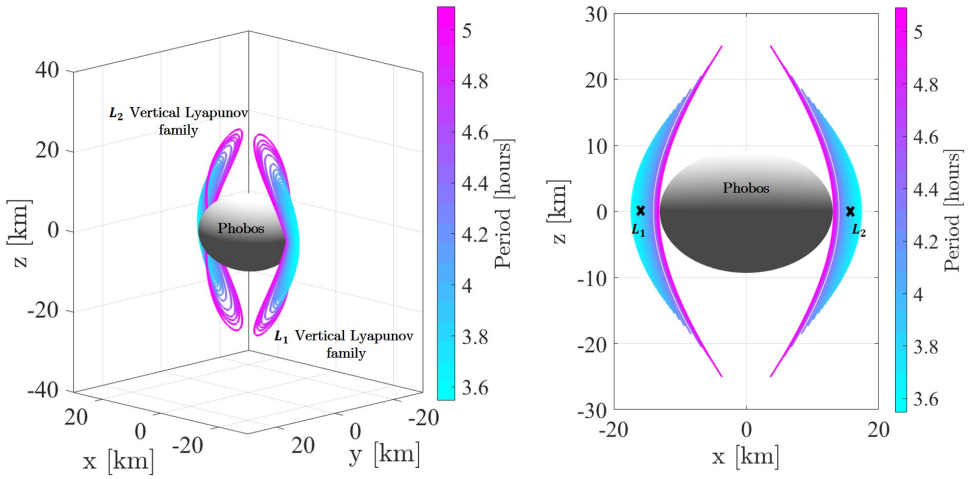

Figure 2.8: Dynamics around Mars-Phobos Lagrangian points: Vertical Lyapunov Orbit families around L_1 and L_2.

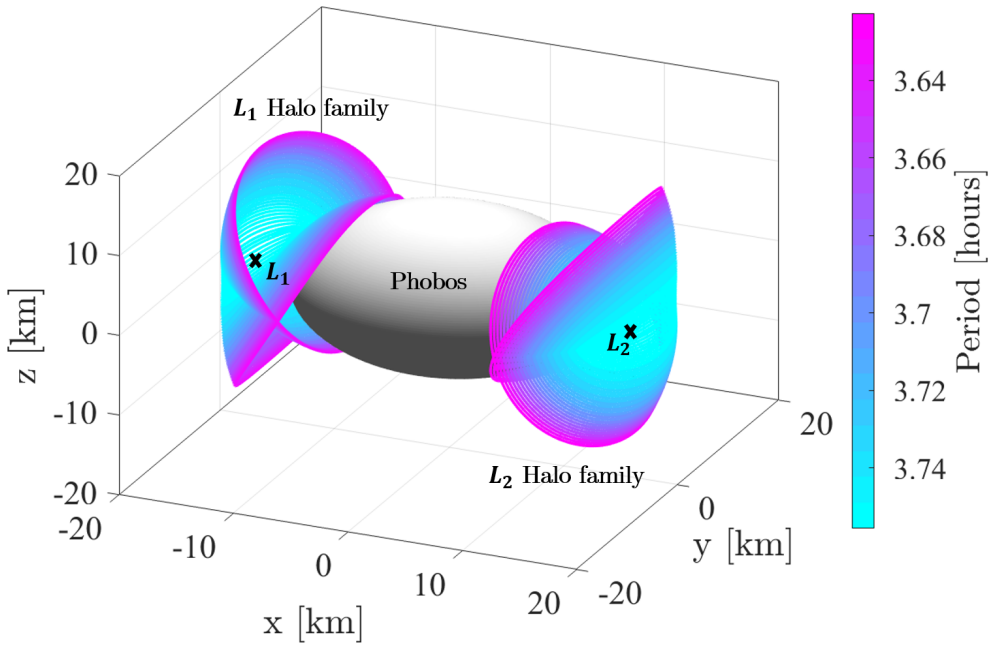

Figure 2.9: Dynamics around Mars-Phobos Lagrangian points: Northern and Southern Halo orbit families around L_1 and L_2.

Other periodic orbits around Phobos are family f and g type orbits known as retrograde and prograde families of orbits existing around the smaller primary in the CRTBP framework. The family 'g' exhibits a complex behavior that evolved from stable circular prograde oscillations around the smaller primary. In the Mars-Phobos system, prograde families lie within and closer to the surface of Phobos. These families of orbits are used to study point-to-point jumping arcs on the Phobos' surface that exhibit lower take-off and landing velocities[66]. Examples of prograde orbit family continuation using the pseudo-arclength continuation method are shown in Fig. 2.10 (b), along with the retrograde families in Fig. 2.10 (a). These retrograde orbit families or family 'f' orbits are most widely known as distant retrograde orbits (DROs) or Quasi-satellite Orbits (QSOs) in the literature. Chapter 3 elaborates on the computation of these families of orbits and review key dynamical properties of retrograde relative orbits and their application to space mission design.

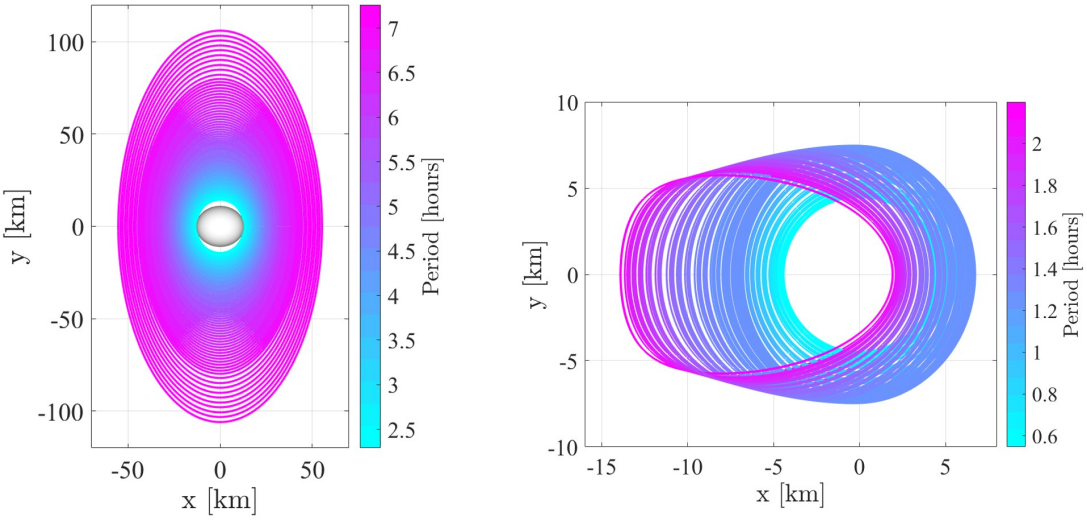

a) Retrograde Family b) Prograde Family

Figure 2.10: Dynamics around Phobos: a) Retrograde Orbits; b) Prograde Orbits.

2.4 Stability of Periodic Orbits

The monodromy matrix, M, defined as the state transition matrix propagated for exactly one period of the orbit, is commonly used to determine orbital stability. Let $\delta \boldsymbol{x_0}$ be a small perturbation about the initial state of the computed periodic orbit. State transition matrix maps this initial deviation forward in time after 'n' orbital periods.

$$\delta \boldsymbol{x_n} = \Phi(T_n, t_0)\delta \boldsymbol{x_0} = \Phi(T_n, T_{n-1})...\Phi(T, t_0)\delta \boldsymbol{x_0} = M_n \delta \boldsymbol{x_0} \tag{2.19}$$

Following the nature of Hamiltonian dynamical systems, for each eigenvalue $\lambda \in \mathbb{R}$ of M, $1/\lambda$ is also an eigenvalue, and occur in reciprocal pairs[57, 67]. Also, if $\lambda \in \mathbb{C}$, then $\bar{\lambda}$ and $1/\bar{\lambda}$ are eigenvalues of M. Periodic orbits are stable only when all of the eigenvalues ($\lambda_i, \forall i = 1, 2, .., n$) of M have a magnitude less than unity, i.e., $|\lambda_i| \leq 1, \forall i = 1, 2, .., n$.

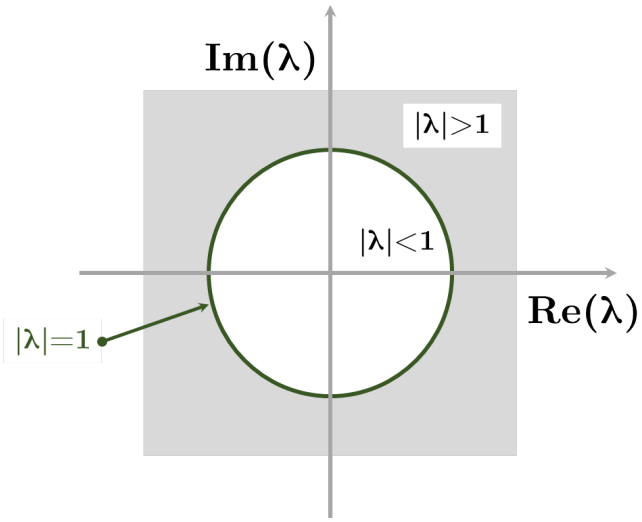

Figure 2.11: Stability bound for the eigenvalues of the monodromy matrix.

Fig. 2.11 illustrates the stability bounds for eigenvalues of the monodromy matrix in the complex plane to the unit circle. Non-trivial and complex eigenvalues placed on the unit circle ($|\lambda| = 1$) indicate the existence of oscillatory modes. Pair of reciprocal eigenvalues that are placed off the unit circle, on the other hand, indicates the presence of unstable ($|\lambda| > 1$) and stable ($|\lambda| < 1$) modes governing the motion in the vicinity of the periodic orbit. When a pair of non-trivial eigenvalues reach any critical value, bifurcation occurs, which will be discussed in the following subsection.

Let $\boldsymbol{\varphi}_T(\boldsymbol{x_0}) = \boldsymbol{x_0}$ be the periodic solution of Equations of motion, then

$$\boldsymbol{\varphi}_T(\boldsymbol{x_0} + \delta\boldsymbol{x_0}) \simeq \boldsymbol{\varphi}_T(\boldsymbol{x_0}) + M\delta\boldsymbol{x_0} + H.O.T = \boldsymbol{x_0} + \delta\boldsymbol{x_0}. \tag{2.20}$$

On neglecting H.O.T yields $(M - I_n)\delta\boldsymbol{x_0} = 0$, where I_n is an identity matrix, resulting with an eigenvalue $\lambda = 1$. If this is true, a second eigenvalue must be equal to unity as well. Furthermore, the characteristic polynomial of a 6-by-6 monodromy matrix can be further simplified as

$$\begin{aligned} det(M - \lambda I_n) &= (\lambda - 1)^2(\lambda - \lambda_1)(\lambda - 1/\lambda_1)(\lambda - \lambda_2)(\lambda - 1/\lambda_2), \\ &= (\lambda - 1)^2(\lambda^2 + b_1\lambda + 1)(\lambda^2 + b_2\lambda + 1), \end{aligned} \tag{2.21}$$

where λ_1, $1/\lambda_1$, λ_2, $1/\lambda_2$ are other non-trivial eigenvalues of M, and $b_1 = -(\lambda_1 + 1/\lambda_1)$ and $b_2 = -(\lambda_2 + 1/\lambda_2)$ must be real with $max(|Re(b_1)|, |Re(b_2)|) < 2$ for a periodic orbit to be stable.

Values b_1 and b_2 are referred to as stability indices and will be evaluated throughout this thesis to assess the stability of the periodic orbits[68, 69]. Following Bray and Goudas[70], b_1 and b_2 are calculated as

$$b_1, b_2 = \frac{\alpha \pm \sqrt{\alpha^2 - 4\beta + 8}}{2}, \tag{2.22}$$

where $\alpha = 2 - trace(M)$ and $\beta = \frac{\alpha^2 - trace(M^2)}{2} + 1$,

$$1/\lambda_j, \lambda_j = \frac{-b_j \pm \sqrt{b_j^2 - 4}}{2}, \forall j = 1, 2, \tag{2.23}$$

Eq. (2.23) provides an efficient relation for computing the eigenvalues of the monodromy matrix of any periodic orbit of a six-dimensional autonomous Hamiltonian system.

Naturally, once the eigenvalues of M are known, the resulting eigenvectors can be used to compute the invariant manifolds associated with the periodic orbit. The invariant manifolds of a periodic orbit are computed by perturbing the states along the direction of periodic orbit's local eigenvectors.

Stable and Unstable invariant manifolds originating from various regions along the unstable periodic orbits are usually characterized using numerical computation on

multiple nodes of the periodic orbit.

Let $\mathbf{Y}^s(\mathbf{X}_0)$ and $\mathbf{Y}^u(\mathbf{X}_0)$ be the normalized stable and unstable eigenvectors associated with the real pair of eigenvalues of the monodromy matrix M evaluated in an arbitrary point $\mathbf{X}_0$.

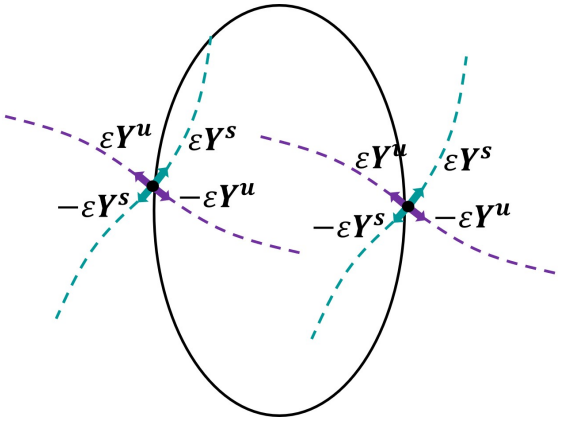

Figure 2.12: Direction of perturbed eigenvectors from a periodic orbit.

Fig. 2.12 shows the direction of the perturbed normalized stable and unstable eigenvectors from a periodic orbit(PO). Here, we defined arbitrary points along PO equally spaced in time and approximated the computation of stable and unstable manifolds locally. The computation of stable and unstable manifolds associated with an unstable PO can be accomplished using suitable numerical integration procedures [71]. Initial guesses for stable and unstable manifolds are given by

$$\mathbf{X}^s(\mathbf{X}_0) = \mathbf{X}_0 \pm \varepsilon \mathbf{Y}^s(\mathbf{X}_0) \tag{2.24}$$

$$\mathbf{X}^u(\mathbf{X}_0) = \mathbf{X}_0 \pm \varepsilon \mathbf{Y}^u(\mathbf{X}_0) \tag{2.25}$$

Where, ε is small displacement from $\mathbf{X}_0$. In this work we have displaced the initial state by $\varepsilon = 1 \times 10^{-4}$. This perturbation should be set numerically as low as possible while designing maneuver-free transfers.

Propagating Eq.(2.24) backwards in time, we generate stable manifold trajectories. Similarly, propagating Eq.(2.25) forward in time, we generate unstable manifold trajectories. These are further explored for spatial transfer design discussed in the Chapter 5.

2.5 Bifurcation of Periodic Orbits

In dynamical systems, a bifurcation may lead to a change in stability along a periodic orbit family, resulting in new families of periodic orbits or termination of existing families of periodic orbits. Based on the stability of the periodic orbit, local bifurcations are detected and characterised by monitoring the non-trivial eigenvalues of the monodromy matrix corresponding to each of the periodic orbits in a family[72]. Any changes in the eigenvalues can result in varying degrees of linear instability along the solution curve.

Fig. 2.13 depicts the non-trivial eigenvalues on either side of the bifurcation in a complex plane for various types of bifurcation. Following are types of bifurcations found in dynamical systems theory: Tangent Bifurcations, Period-doubling Bifurcations, and Period-multiplying Bifurcations. Each type of bifurcation is associated with a specific change in characteristics of the dynamics in the vicinity of the periodic orbits in a family.

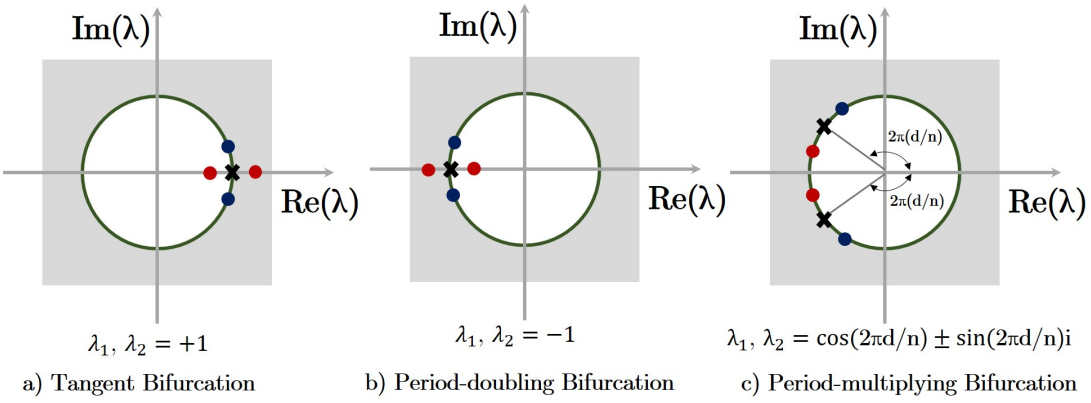

Figure 2.13: Non-trivial eigenvalues in the complex plane, illustrating the stability of periodic orbits on either side of bifurcation points. (Unit circle is represented by *green*, the eigenvalues are represented by *red* and *blue*, and the critical value or bifurcation is represented by black 'x'.)

2.5.1 Tangent Bifurcations

A tangent bifurcation occurs when the orbital stability of a family of periodic orbits changes as a parameter variation, such as the Jacobi constant. The nontrivial eigenvalues

($\lambda_1 = \lambda_2 = 1$) of the monodromy matrix reaches the critical values (i.e., $b_j = 2$) during this type of local bifurcation. Tangent bifurcations are classified into three types[64]: Cyclic fold, Pitchfork, and Transcritical. When the stability of orbits along a single-family is varied without creating or intersecting any other families of orbits, cyclic fold bifurcation occurs. Pitchfork bifurcation occurs when a change in the instability of a periodic orbit family causes the orbits to split into two new families with comparable stability. Finally, transcritical bifurcation is defined as the point of intersection between stable and unstable families of periodic orbits that share stability properties. An example of tangent bifurcations is presented in Fig. 2.14 (subplot 1), where the bifurcations lead to the L_1 halo orbit family from the L_1 planar Lyapunov orbit family in the vicinity of Phobos.

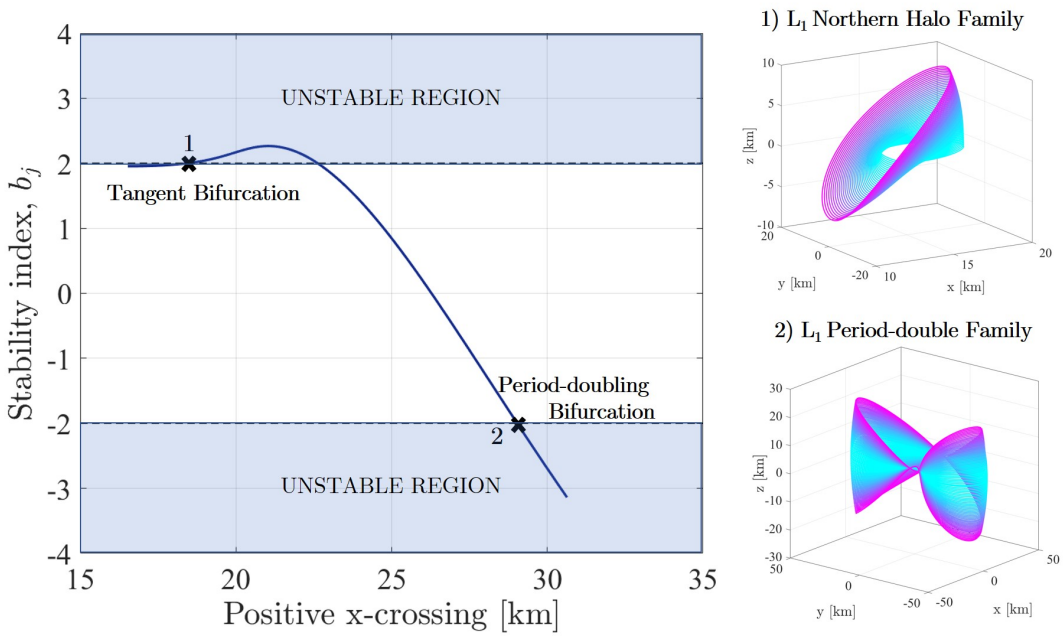

Figure 2.14: Stability indices of L_1 planar Lyapunov periodic orbit family and bifurcated families of periodic orbits.

2.5.2 Period-doubling Bifurcations

Period-doubling bifurcation takes place when the nontrivial eigenvalues ($\lambda_1 = \lambda_2 = -1$) of the monodromy matrix reach corresponding critical stability indices (i.e., $b_j = -2$). The change in qualitative stability characteristics of the periodic orbit family also

indicate the intersection of the n-periodic family with the $2n$-periodic family. Fig. 2.14 (subplot 2) illustrates the family of period-double bifurcations of the L_1 planar Lyapunov periodic orbit family.

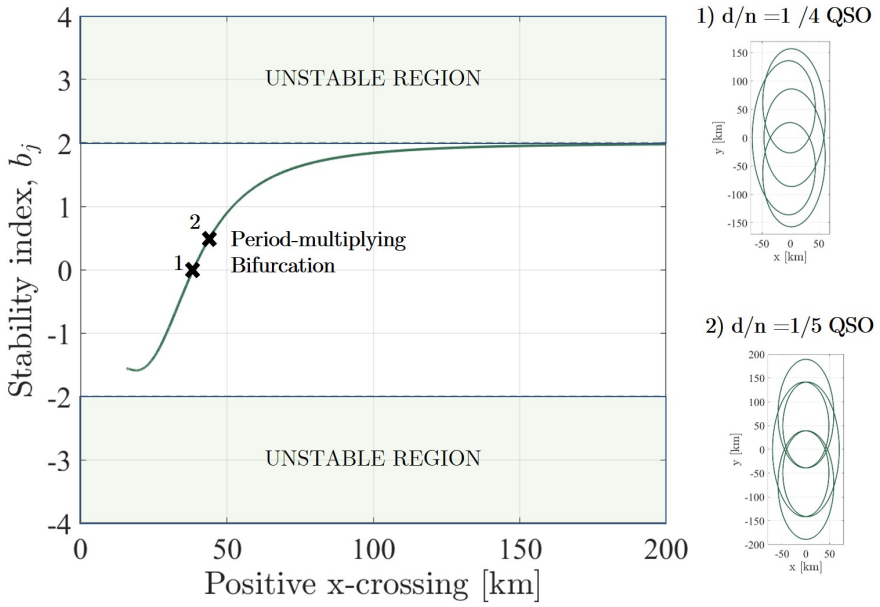

Figure 2.15: Stability indices of planar Quasi-satellite Orbit family around Phobos and period-multiplying bifurcated families at d/n=1/4 and 1/5.

2.5.3 Period-multiplying Bifurcations

Besides the critical cases of stability indices (i.e., $b_j = \pm 2$) that lead to tangent ($\lambda_1 = \lambda_2 = 1$) and period-doubling ($\lambda_1 = \lambda_2 = -1$) bifurcations, several other families of periodic orbits bifurcate with multiple periods from the initial family of periodic orbits[73, 74]. In particular, for the ranges of stability indices $-2 < b_j < 2$, period-multiplying or resonant bifurcation occurs when two non-trivial eigenvalues of M correspond to the n^{th} roots of unity, i.e., $\lambda_1 = \lambda_2 = \sqrt[n]{1} = cos(2\pi d/n) \pm sin(2\pi d/n)i$, such that when the stability of the periodic orbit family reaches critical stability indices values defined by a resonant ratio (d/n) in Eq.(2.26)[52, 53, 72].

$$b_{Res} = 2\cos 2\pi\frac{d}{n}, \quad d, n \in N \tag{2.26}$$

where d and n are integer numbers. Note that the integer 'd' indicates a near-commensurability of period between the orbit at the point of bifurcation and the rotation of the coordinate system, whereas 'n' denotes the periodic multiplicity.

Thus corresponding stability index of the n-fold periodic orbit after a period $\tau = nT$ is $|b_j| = 2$, and these critical orbits are "$d:n$ bifurcated orbits" and the family of periodic orbits that emerge from d:n bifurcated point is "$d:n$ bifurcated families." Such period-multiplying bifurcated families are used in this research to systematically design and develop transfer procedures that establish transfer design space between relative quasi-satellite orbits. As an example illustrated in Fig. 2.15, bifurcations at points 1 and 2 result in period-quadruple (1/4) and period-quintuple (1/5) bifurcated periodic quasi-satellite orbits bifurcating from the planar QSO family. The following chapter explains how to systematically compute the families of bifurcated QSOs that are used in the transfer design methods described in Chapters 4 and 5.

3 Bifurcated Quasi-satellite Orbits

3.1 Introduction

The dynamic environment around Phobos is complex. The low mass-distance relationship between Mars and Phobos makes it impossible to consider classical Keplerian or two-body motion about Phobos for mission design. Consequently, mission designers have looked at different orbit candidates that would allow close inspections of the Martian moon from higher and safer distances[75, 76]. Due to the proximity of the Lagrangian points to the surface of Phobos, mission design using liberation point orbits is impractical. On the other hand, Quasi-satellite Orbits (QSOs) or Distant retrograde orbits (DROs) are the class of periodic orbits that lie outside the SOI of the smaller primary (i.e., Phobos). The peculiar case of smaller planetary satellites such as Phobos is very suitable for exploiting these orbits for closer observation of the Phobos surface. QSOs are generally considered one of the three kinds of co-orbital configurations in CRTBP with 1:1 resonance. Other co-orbital configurations include Tadpole and Horseshoe Orbits[34, 77].

3.2 Quasi-satellite Orbits around Phobos

In this research, Phobos is assumed to move around Mars in a circular orbit with semi-major axis $a_P = 9377$ km. If we momentarily neglect its gravitational attraction, a spacecraft on an eccentric orbit with the same semi-major axis would remain in the vicinity of the Martian moon and describe purely periodic orbits with respect to the co-rotating frame of the planetary satellite. More specifically, a spacecraft would describe 2:1 ellipses centered on Phobos and with period equal to its orbital period around Mars (7.66 hrs) as prescribed by the analytical solution of the Hill-Clohessy-Wiltshire (HCW) equations [78]. HCW equations are not applicable in the vicinity of the Phobos surface.

If we now consider the gravitational attraction of Phobos, the closer spacecraft to the surface of the Martian moon, the higher the gravitational influence of the planetary satellite on the relative trajectory of the spacecraft. Because of this perturbation, lower altitude QSOs are usually computed via differential correctors techniques that search for purely periodic orbits while migrating inwards from high-altitude 2:1 ellipses that are less affected by the gravity of the planetary satellite. In this research, we have utilized pseudo-arclength continuation [65] and shooting methods for calculating families of QSO as shown in the left subplot of Fig 3.1. Other alternative analytical approaches to compute QSOs include works of Kogan [79], Lidov [80, 81], and Lara [82].

The current mission design of MMX envisages the utilization of different altitude planar QSOs in order to characterize the gravitational field before landing on Phobos[20, 83]. Key features of these baseline trajectories are tabulated in Table 3.1, whereas the right subplot of Fig. 3.1 depicts the candidate relative orbits as seen from the Mars-Phobos synodic frame.

Table 3.1: MMX Candidate QSO.

Name	$x \times y$ (km)	$\dot{x} \times \dot{y}$ (m/s)	T (hrs)	C (−)
QSO-H [High]	100×198.47	45.74×22.95	7.59	−8.78
QSO-M [Mid]	50×94.41	23.41×12.04	7.13	−2.20
QSO-La [Low(a)]	30×48.83	15.31×8.68	5.76	−0.78
QSO-Lb [Low(b)]	22×30.81	12.79×8.25	4.40	−0.37
QSO-Lc [Low(c)]	20×26.69	12.31×8.31	3.97	−0.27

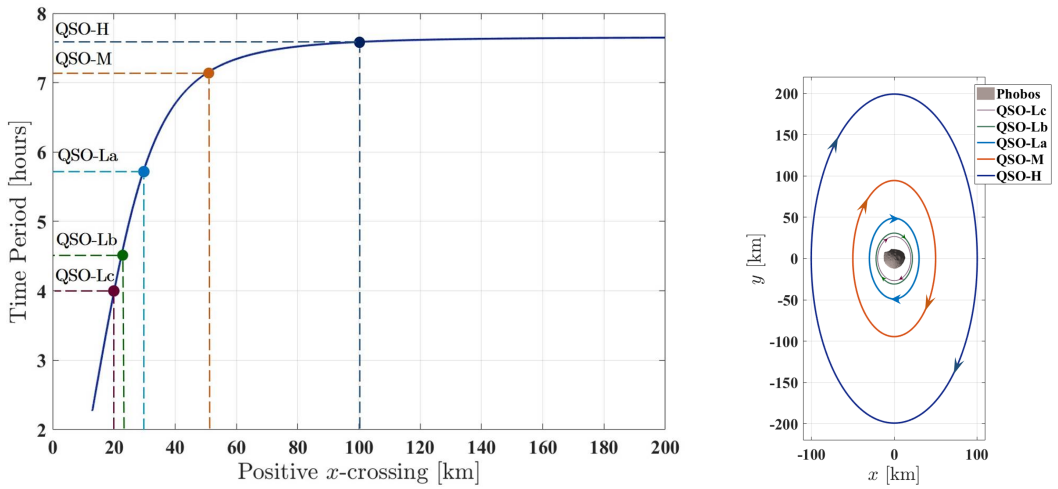

(a) (b)

Figure 3.1: a) Time Period vs positive x-axis crossing of the QSO family branch. b) MMX baseline quasi-satellite orbits.

3.3 Multi-Revolution Periodic Quasi-satellite Orbits

Multi-Revolution Periodic QSO (MP-QSO) are retrograde relative trajectories that repeat after several revolutions around Phobos. As MP-QSO bifurcate from single-revolution QSO, this type of periodic orbits can be found in the vicinity of the Martian moon when either of the stability indices b_j crosses the resonant value as indicated in the Eq. (2.26)

$$b_{Res} = 2\cos 2\pi\frac{d}{n}, \quad d, n \in N,$$

where d and n are integer numbers defined in [53]. Note that the integer 'd' indicates a near-commensurability of period between the orbit at the point of bifurcation and the rotation of the coordinate system [52], whereas 'n' denotes the multiplicity of a periodic orbit, i.e., the number of revolutions around Phobos. The value of b_{Res} corresponding to the ratios of $d : n$ are shown in the Fig. 3.2. These periodic orbits are referred as $d : n$ MP-QSO and examples of them are shown in Fig. 3.3.

Let $\boldsymbol{x}_0^*$ and T^* be the initial state and orbital period of the bifurcation point. Bifurcation points are detected using a bisection method on the curves of Fig. 3.2. Once a positive x-axis crossing has been obtained, its corresponding QSO orbit is calculated leading to an accurate estimate of $\boldsymbol{x}_0^*$ and T^*. In addition, the monodromy matrix of

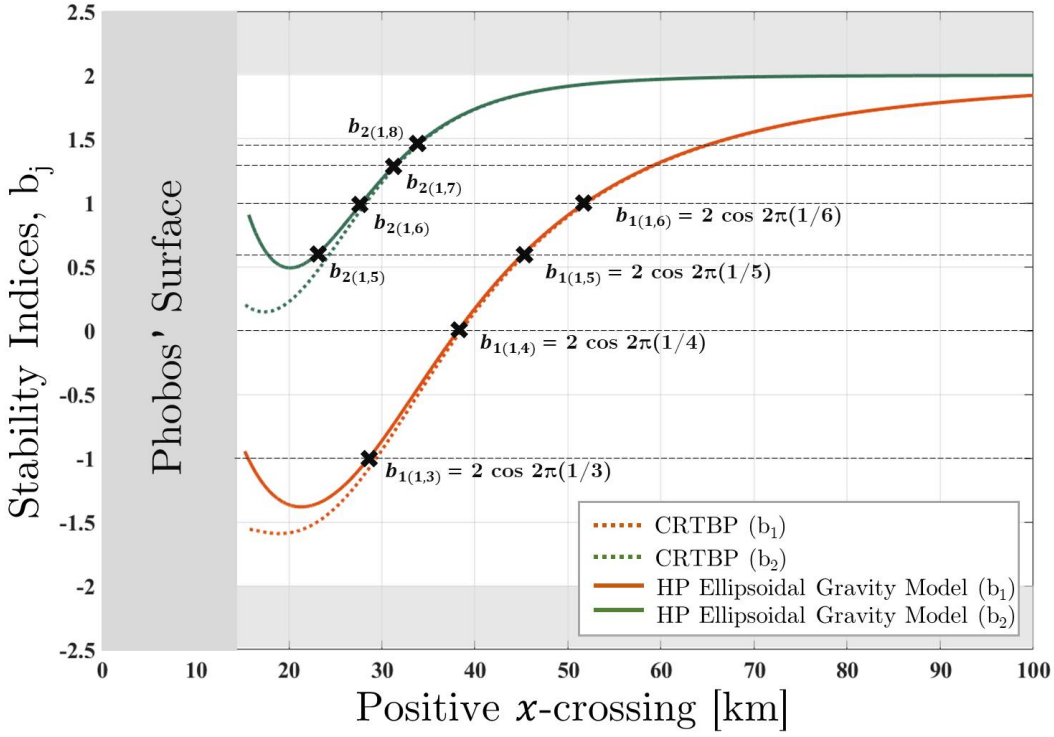

Figure 3.2: Stability Indices of QSO and bifurcation points.

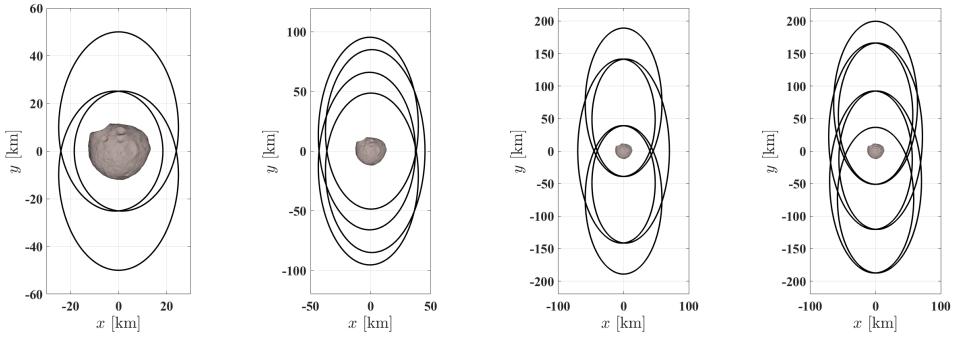

(a) 1:3 MP-QSO (b) 1:4 MP-QSO (c) 1:5 MP-QSO (d) 1:6 MP-QSO

Figure 3.3: Bifurcated d:n MP-QSOs from b_1.

the newly found QSO is multiplied for n times and diagonalized to approximate the direction of the researched $d:n$ MP-QSO family tangent. We consider $\tilde{Z}_0^* = \left[\tilde{x}_0', \tilde{T}'\right]^T$

be the family tangent of the MP-QSO family, where $\left[\tilde{x}_0', \tilde{T}'\right]^T$ are unit tangential state vector and propagation time to the solution curve at $Z_0^* = \left[x_0^*, T^*\right]^T$ as shown in Fig. 3.4. This bifurcation analysis reveals that there are two families of MP-QSOs emanating

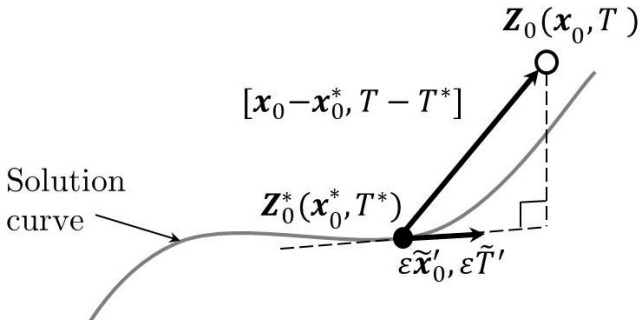

Figure 3.4: Pseudo-arclength continuation on bifurcation points.

from each bifurcation point (*pitchfork* bifurcation). These two branches will be referred to as “symmetric" and “asymmetric" MP-QSO depending on whether the radial velocity ($\dot{x}_0$) of the predicted initial point, namely $x_0 = x_0^* \pm \varepsilon\, \tilde{x}_0'$, is equal or not to zero. To enforce the “symmetric" condition, we add an additional constraint on the initial radial velocity of the MP-QSO and run a pseudo-arclength continuation procedure that generates MP-QSO family branches from the initial conditions from Eq. (3.1) and family tangent $\tilde{Z}_0^*$.

$$\begin{cases} x_0 &= x_0^* \pm \varepsilon\, \tilde{x}_0', \\ T &= n\, T^* \pm \varepsilon\, \tilde{T}', \end{cases} \tag{3.1}$$

The variable ε is a small parameter, this work used $\varepsilon = 10^{-4}$, whose magnitude can be adjusted throughout the continuation process to control the number of family members being computed. Also notice that the resulting symmetric MP-QSOs can be classified as Type-I and Type-II $d : n$ MP-QSO based on the direction of the initial perturbation of the initial state as shown in Fig. 3.5.

Figure 3.6 depicts the in-plane bifurcated branches of quasi-satellite orbits. For clarity, we have highlighted family branches with a multiplicity factor ‘n’ of 15 in this figure (i.e., number of revolutions around Phobos). The black curve identifies the planar QSO family, while the bifurcated MP-QSO branches evolving from the primary solution curve are highlighted by the blue curves.

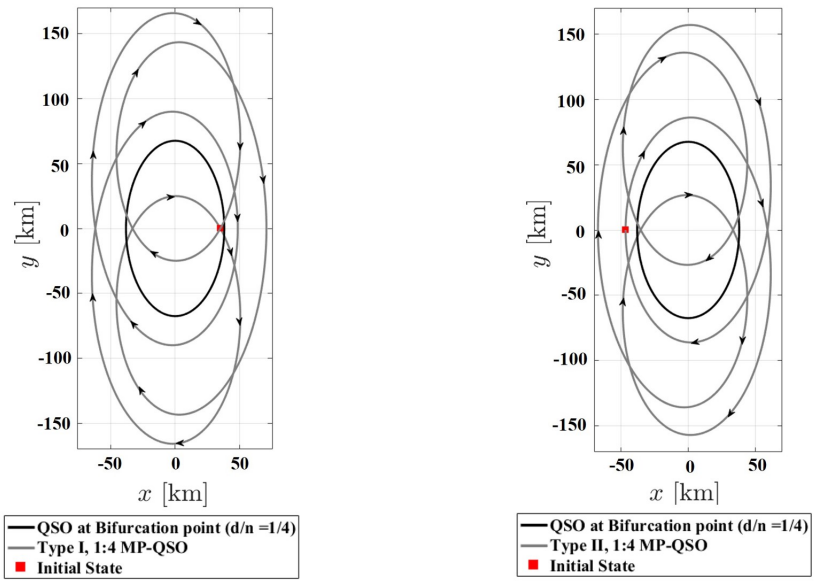

(a) Type-I (anti-Mars direction). (b) Type-II (Mars direction).

Figure 3.5: Types of MP-QSO branch based on direction of initial perturbation.

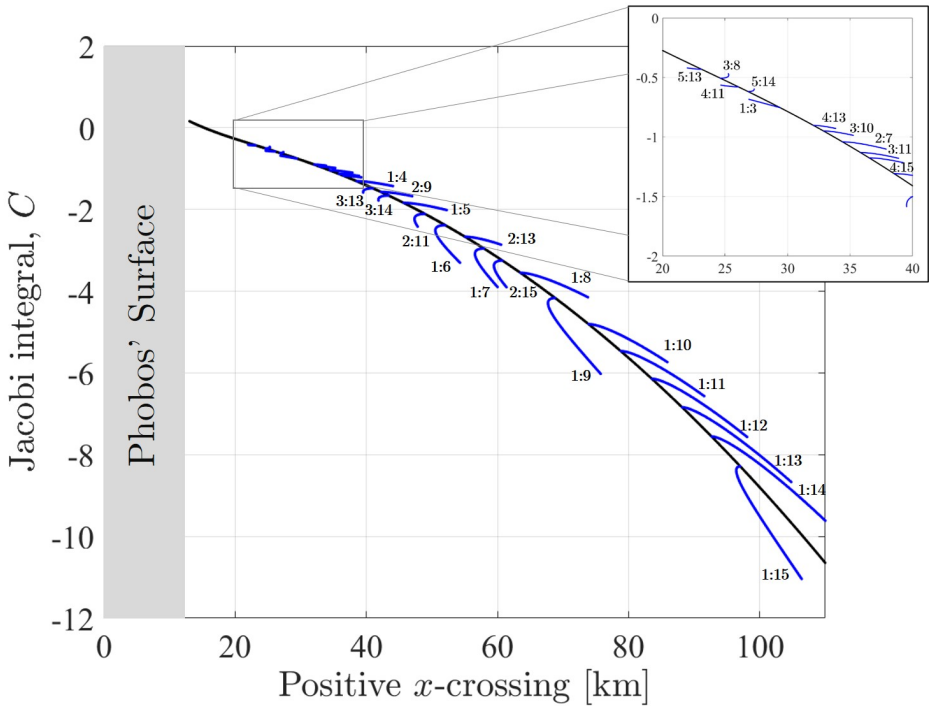

Figure 3.6: In-plane QSO families (MP-QSOs) bifurcating from Planar QSO family.

The enlarged view of branches evolving between 20 and 40 kilometers is shown in the subplot of Fig. 3.6. These bifurcated family branches closer to Phobos' surface and their proximity to the surface makes scientific observations impractical. The branches beyond 40 kilometers, on the other hand, can be used to observe Phobos. Fig. 3.8 shows examples of MP-QSOs bifurcated from the branches of Fig. 3.6. Fig. 3.7 illustrates the summary of systematic computation of bifurcated QSO families. For a robust and safe transfer, leveraging the geometry of MP-QSOs, we propose a transfer technique in Chapter 4 to transfer spacecraft between relative QSOs in the proximity of Phobos. The out-of-plane bifurcations from the stability curves b_2 are known as 3D-QSOs or spatial QSOs, numerical procedures for generation of spatial QSOs, and applicability for Phobos high latitude region observations are discussed in the following section.

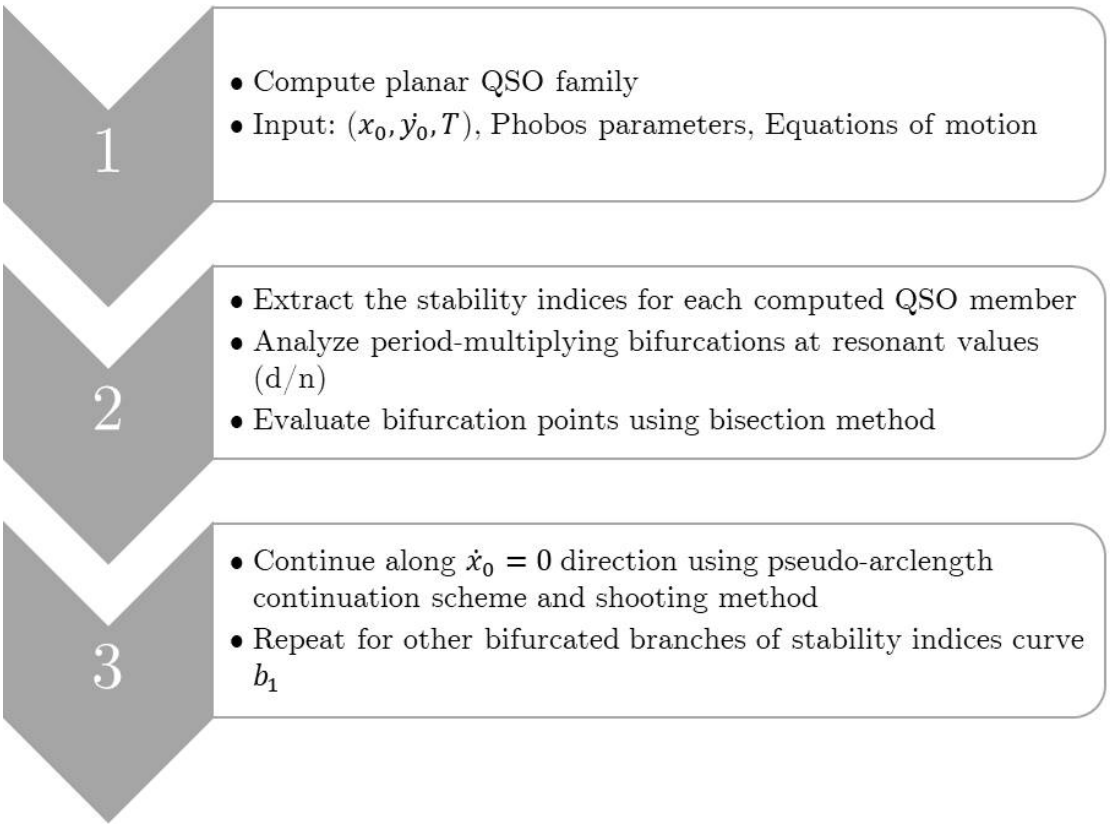

Figure 3.7: Systematic computation of bifurcated QSO families.

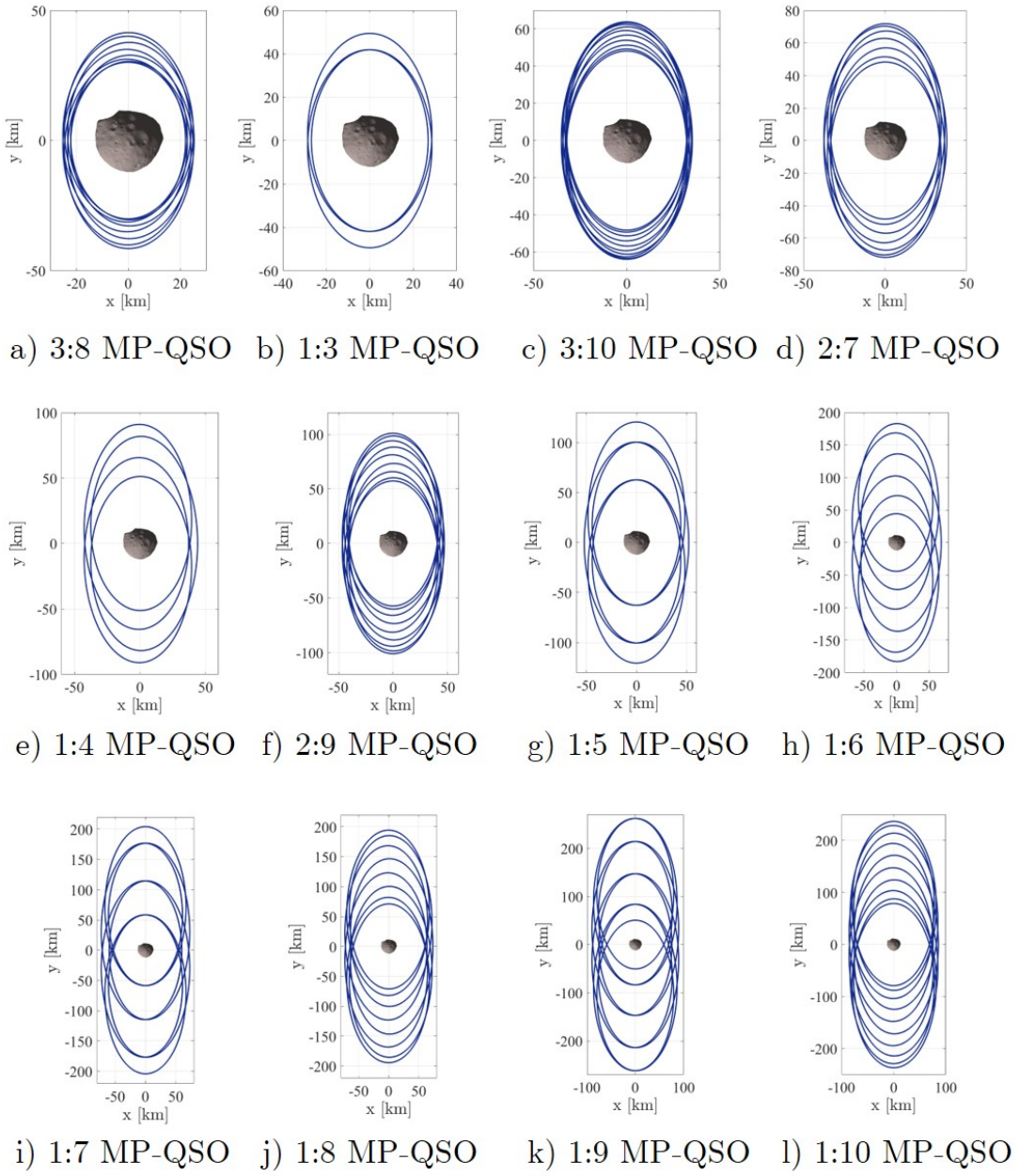

Figure 3.8: Examples of MP-QSO families.

3.4 Spatial Quasi-satellite Orbits

Spatial Quasi-satellite Orbtis or 3D-QSOs are out-of-plane bifurcated families of the planar QSO family. These 3D-QSOs are computed from the out-of-plane bifurcations of the planar QSO family branch b_2. Stability indices curves illustrated in the Fig. 3.2 indicates the period-multiplying bifurcation points at in-plane and out-of-plane stability indices curves(i.e., b_1 and b_2). The families of periodic orbits evolving from the b_2 are linearly unstable and have high-latitude coverage advantages for any scientific missions to distant smaller planetary satellites. Computing quasi-periodic invariant tori around a planar stable periodic QSO[84, 42], semi-analytical methods[85, 86] and grid search methods[87, 88] are often used to study QSOs in higher-dimensional systems, such as spatial or non-autonomous models.

In this section, we hereby calculate families of 3D-QSOs via bifurcations of resonant values $(d : n)$ [52]. These bifurcating orbits can be identified using the eigenvalues of the monodromy matrix corresponding to each orbit in the family. Remember that the presence of a bifurcating orbit is indicated by a change in stability, as indicated by the eigenvalues of the monodromy matrix.

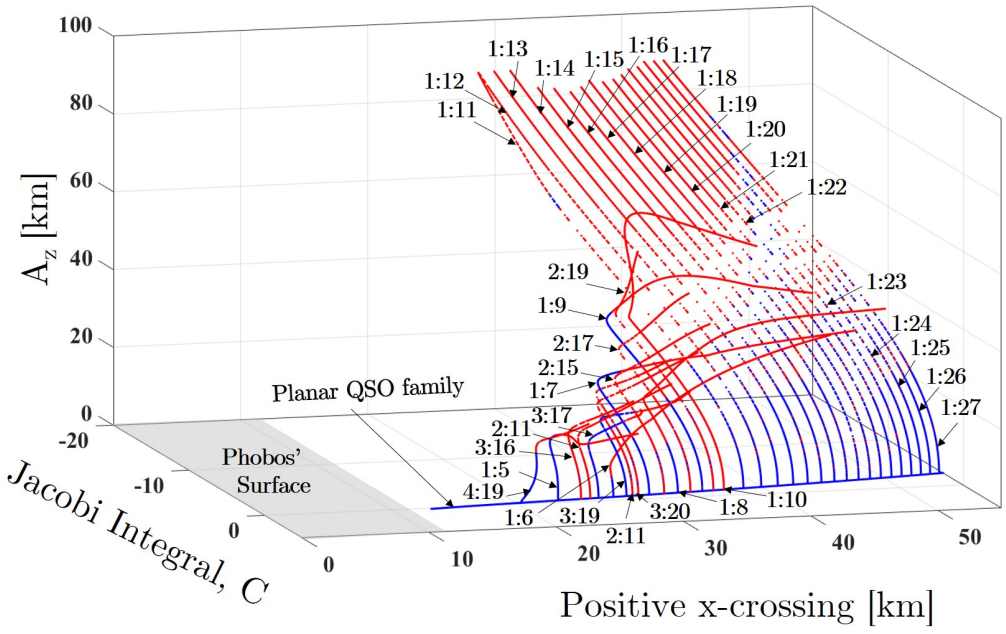

Figure 3.9: Out-of-plane QSO families (3D-QSOs) bifurcating from Planar QSO family.

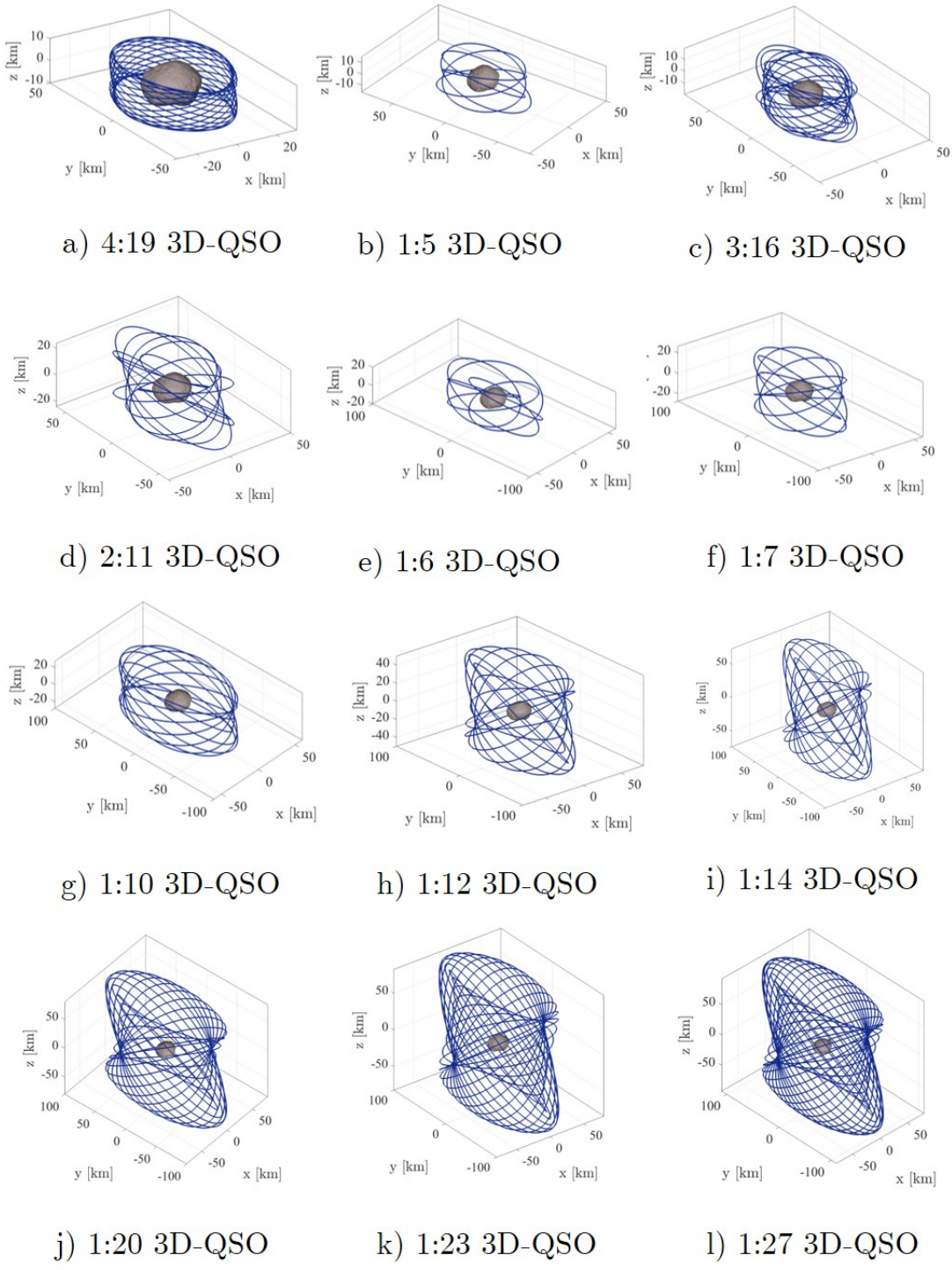

Figure 3.10: Examples of 3D-QSO families.

After identifying the bifurcating orbit, an algorithm similar to the one used to compute MP-QSOs from the planar QSO family branch can target these out-of-plane 3D-QSO families. Hereafter, vertical bifurcations will be referred to as $d:n$ 3D-QSOs. The bifurcated branches from planar QSOs are shown in Fig. 3.9, whereby the family of plane-symmetric periodic orbits is computed with $z \neq 0$ and $\dot{z} = 0$. The blue dots indicate stable periodic orbits, whereas the red dots indicate unstable periodic orbits. Examples of $d:n$ 3D-QSOs of different $d:n$ from the Fig. 3.9 are shown in Fig. 3.10. Note that not every resonance ratio is labeled for the sake of brevity. Furthermore, the intersection of solutions mapped on the figure does not imply the same orbit as they have different initial values of $\dot{y}_0$. We observe that most of the 3D-QSO families with A_z >40 km are weakly to highly unstable as there is a switch in the stability of the computed families bifurcated 3D-QSOs. However, these out-of-plane bifurcated retrograde orbit families are ideal for high latitude observations. In the MMX mission, scientific observations for high latitude coverage, and global mapping of Phobos surface terrain, MMX envisions utilizing 3D-QSOs at low-mid altitude regions of current baseline altitudes of operation[20].

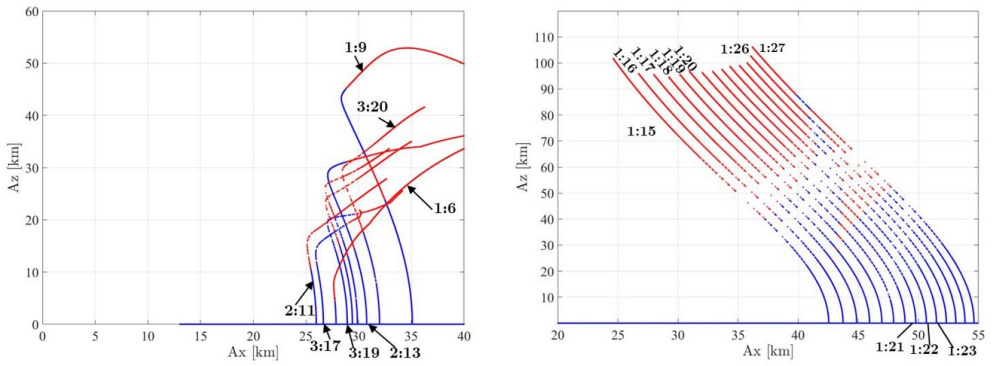

a) Low-altitude b) Mid-altitude

Figure 3.11: A_x vs A_z of Low-Mid altitude 3D-QSO families.

Table 3.2: Potential candidate 3D-QSO

MMX Baseline Altitudes	3D-QSO Families
30 km (Low)	2:11, 3:17, 3:19, 1:9, 2:13, 1:6, 3:20
50 km (Mid)	1:17, 1:18, 1:19, 1:20, 1:21, 1:22, 1,23

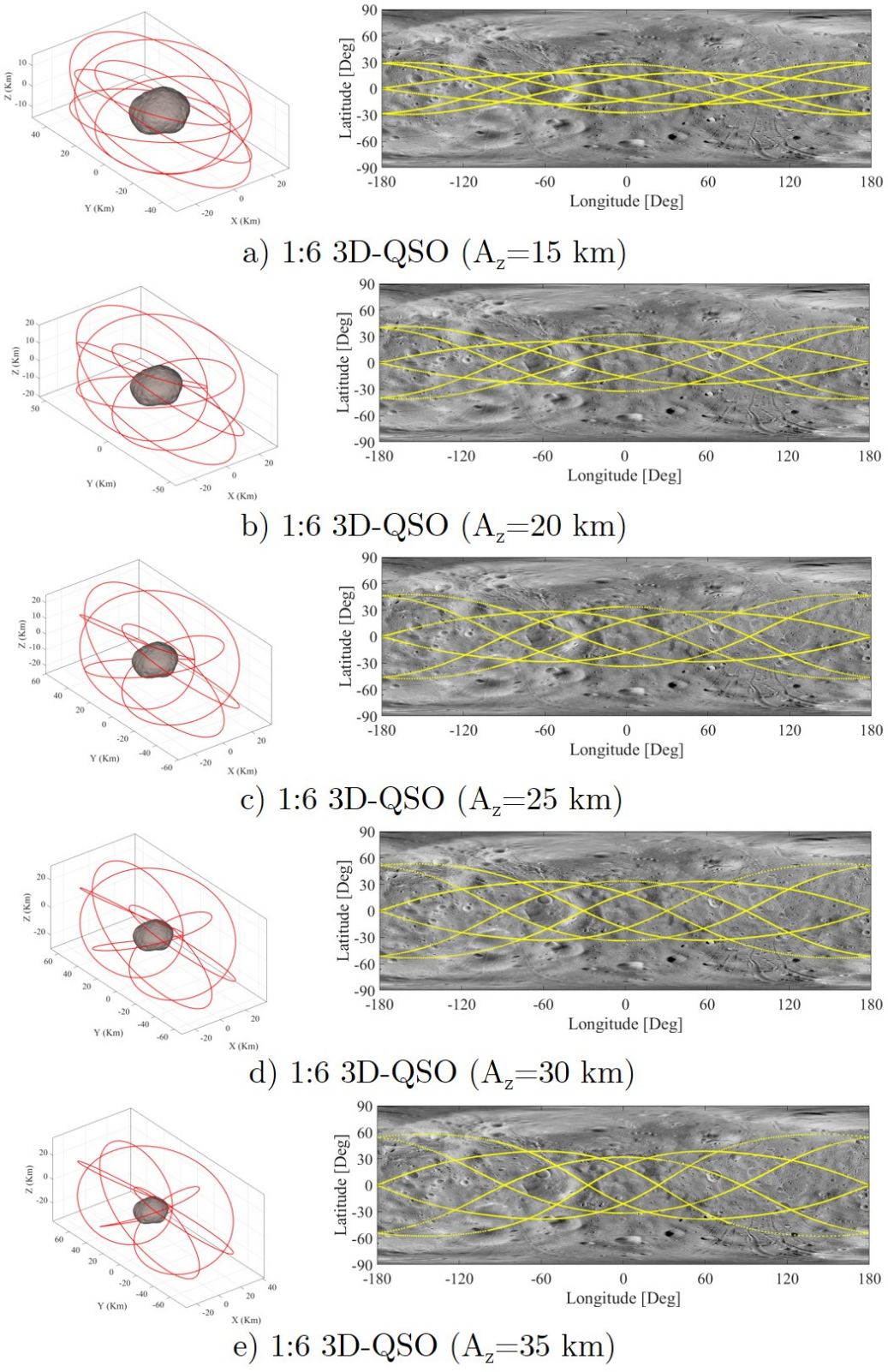

Figure 3.12: Ground tracks of Low-altitude 1:6 3D-QSO families at different A_z.

To support scientific operations[21, 22, 89] and to observe the high-latitude regions of Phobos' surface, we highlight some of the suitable candidate 3D-QSOs within the MMX baseline target altitudes as listed in Table. 3.2. Amplitude variations of these candidate 3D-QSO families at low-mid altitude are shown in Fig. 3.11.

Ground tracks of 3D-QSOs

Examples of low-mid altitude 3D-QSO's ground tracks around x-amplitude (A_x) 30 and 50 km for different z-amplitudes (A_z) are illustrated in the Fig. 3.12 and Fig. 3.13, respectively. 3D-QSO of 1:6 family illustrated in the Fig. 3.12 presents orbits at $A_z \in [15, 35]$. It can be observed that, all the members of 1:6 3D-QSo families in the low-altitude region are highly unstable. From the high-latitude region coverage point of view, $A_z = 15\ km$ covers latitudes between $32.16°N$ and $-32.43°S$. On the other hand, $A_z = 35\ km$ covers latitudes between $60.83°N$ and $-61.14°S$. Due to the proximity to the surface of Phobos, these low-altitude 3D-QSOs require more sophisticated orbital maintenance techniques. Chen et al.[55] analysed stability of these low-altitude 3D-QSOs and revealed practical stability regions. In particular, some of these orbits can be maintained with Δv cost of 1 m/s for 9 days.

Even though preliminary analysis on maintaining low-altitude 3D-QSOs suggests the practical possibility, considering the complex dynamical environment and orbital determinations errors, mid-altitude 3D-QSOs are envisaged for the MMX mission for safer out-of-plane operations. Fig. 3.13 illustrates the ground track of 1:23 3D-QSO family members of different z- amplitude. It can be noted that an orbit of $A_z = 60\ km$ (stable) covers latitudes between $56.78°N$ and $-57.14°S$. In order to cover higher latitude regions, we need unstable 3D-QSOs of $A_z > 60\ km$. In particular, $A_z = 80\ km$ (unstable) covers latitude between $64.20°N$ and $-64.59°S$, whereas $A_z = 100\ km$ (unstable) covers latitudes between $70.83°N$ and $-71.21°S$, and $A_z = 120\ km$ (unstable) covers latitude between $75.30°N$ and $-75.68°S$, respectively. Note that all of the mid-altitude 3D-QSOs become weakly to highly unstable around $A_z = 60\ km$. These results seem to be consistent with Chen et al.[55] findings on the effective stability of 3D-QSOs in the CRTBP framework. Taking advantage of this, we propose a novel transfer methodology that exploits mid-altitude 3D-QSO as an intermediate orbit connecting high-altitude and low-altitude planar QSOs discussed in Chapter 5.

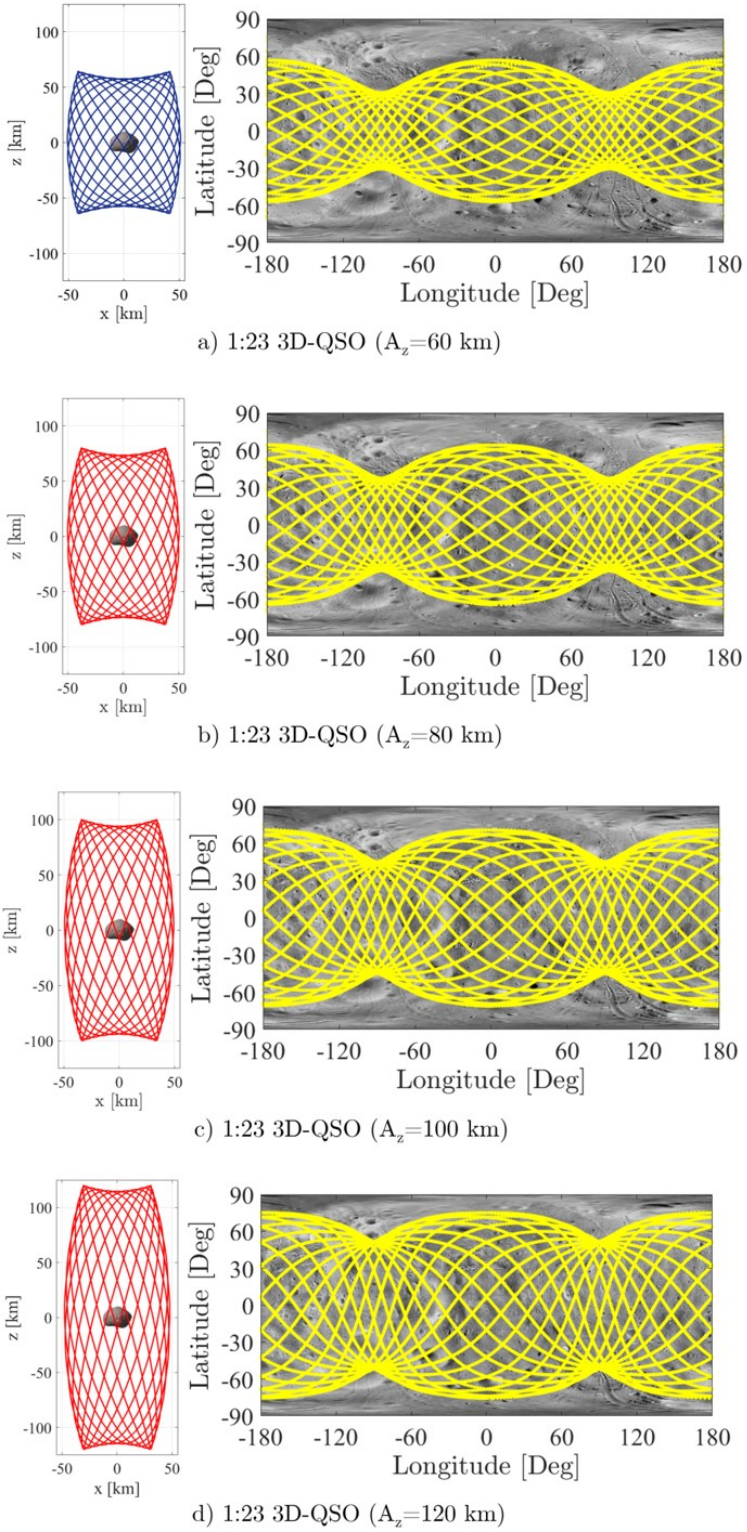

Figure 3.13: Ground tracks of Mid-altitude 1:23 3D-QSO families at different A_z.

4

In-plane Transfer Design

4.1 Introduction

Transfer maps using MP-QSOs provide a basis for robust and safe retrograde transfer trajectories around Phobos. That is, even if the spacecraft skips the ΔV maneuver at the designated point, the spacecraft remain in the MP-QSO and later crossings can be used to perform the orbit injection maneuver into the target orbit. This method involves two impulse transfers, one to escape the initial QSO and another one to insert into the desired lower altitude orbit. The necessary condition for utilizing MP-QSO for transfer applications is that the candidate $d : n$ MP-QSO must intersect both the departure and arrival orbits at least once, and without any intermediate maneuvers. Differently from Ichinomiya et al.[48], who have used fixed positive y-axis departure and free arrival transfer, we hereby allow the departure and arrival point to vary across all possible longitudes $\theta = \arctan(-y/x)$ around Phobos as illustrated in Fig. 4.1(a). Subsequently, the whole transfer design space via MP-QSO is explored and used to develop overall transfer maps between pair of QSO orbits accounting multiple departure and arrival

points. By inspection of computed transfer maps, combinations of departing and arrival longitudes that yield lower ΔV costs for the transfers are revealed.

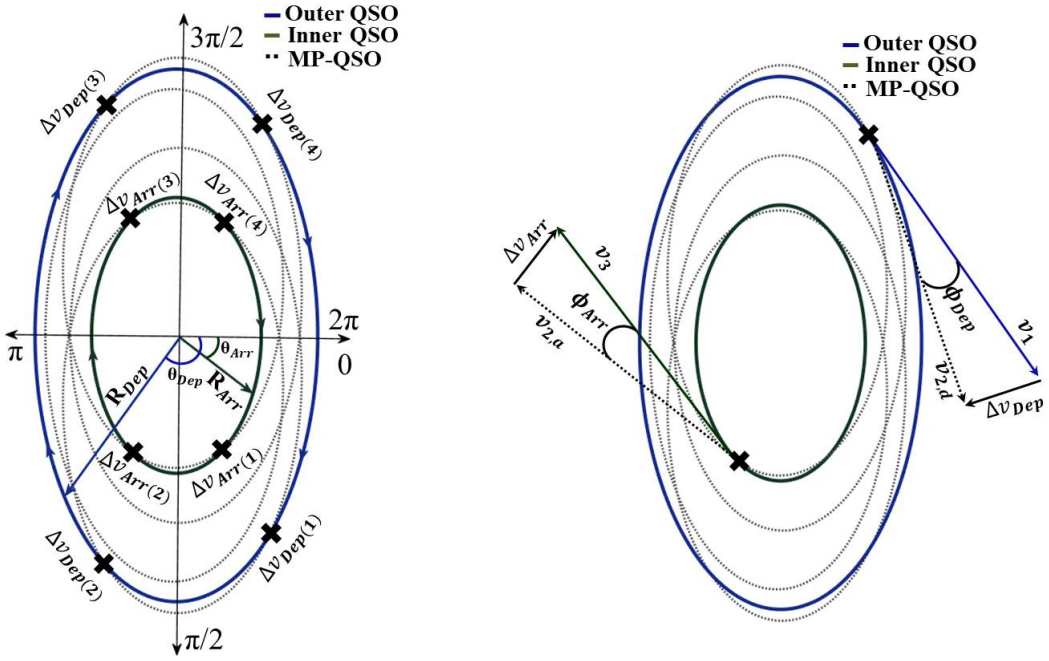

(a) (b)

Figure 4.1: Illustration of the proposed transfer methodology for 1:4 MP-QSO crossings of suitable *departing* and *arrival* QSO orbits.

4.2 Transfer Methodology

To illustrate this transfer approach, let $\boldsymbol{v}_{2,d}$ and $\boldsymbol{v}_{2,a}$ be the velocity vectors of a candidate MP-QSO at arbitrary departure and arrival points as illustrated in Fig. 4.1(b). The ΔV_{Dep} and ΔV_{arr} for the transfer can be represented as

$$\Delta V_{Dep} = \sqrt{v_{2,d}^2 + v_1^2 - 2v_1 v_{2,d} cos\phi_{Dep},}, \tag{4.1a}$$

$$\Delta V_{Arr} = \sqrt{v_{2,a}^2 + v_3^2 - 2v_1 v_{2,a} cos\phi_{Arr},}, \tag{4.1b}$$

where, $\boldsymbol{v}_1$ and $\boldsymbol{v}_3$ are the velocities of a spacecraft in the departing and arrival QSOs when maneuvers are executed. ϕ_{Dep} and ϕ_{Arr} represent the differences in the flight-path

angles before and after the departing and arrival maneuvers.

Let us now denote C_1, C_3, and C_2 the Jacobi integrals of the departing QSOs, the arrival QSOs, and the transfer MP-QSO, respectively. Following Eq. (2.9), we have,

$$v_1^2 = 2(\mathcal{W}(\boldsymbol{r_1}) - C_1), \tag{4.2a}$$
$$v_{2,d}^2 = 2(\mathcal{W}(\boldsymbol{r_1}) - C_2), \tag{4.2b}$$
$$v_{2,a}^2 = 2(\mathcal{W}(\boldsymbol{r_3}) - C_2), \tag{4.2c}$$
$$v_3^2 = 2(\mathcal{W}(\boldsymbol{r_3}) - C_3), \tag{4.2d}$$

implying

$$\Delta V_{Dep} = \sqrt{2(\mathcal{W}(\boldsymbol{r_1}) - C_1) + 2(\mathcal{W}(\boldsymbol{r_1}) - C_2) - 2v_1 v_{2,d} cos\phi_{Dep}}, \tag{4.3a}$$
$$\Delta V_{Arr} = \sqrt{2(\mathcal{W}(\boldsymbol{r_3}) - C_3) + 2(\mathcal{W}(\boldsymbol{r_3}) - C_2) - 2v_1 v_{2,a} cos\phi_{Arr}}. \tag{4.3b}$$

Note that $(\mathcal{W}(\boldsymbol{r}_1) - C_2)$ and $(\mathcal{W}(\boldsymbol{r}_3) - C_2)$ must be greater than zero otherwise the spacecraft cannot reach the corresponding quasi-satellite orbit.

As a result, the ΔV_{total} of the transfer may be written as

$$\Delta V_{total} = \sqrt{4\mathcal{W}(\boldsymbol{r_1}) - 2(C_1 + C_2) - 2v_1 v_{2,d} cos\phi_{Dep}} + \sqrt{4\mathcal{W}(\boldsymbol{r_3}) - 2(C_3 + C_2) - 2v_1 v_{2,a} cos\phi_{Arr}}. \tag{4.4}$$

Equation (4.4) illustrates how the minimum of ΔV_{total} may be affected by various parameters such as

- the effective potentials $\mathcal{W}(\boldsymbol{r}_1)$ and $\mathcal{W}(\boldsymbol{r}_3)$ of the departing and arrival QSOs
- the possible values of C_2 (Jacobi of the transfer orbit. i.e., MP-QSO)
- the differences in the departing and arrival flight-path angles (ϕ_{Dep}, and ϕ_{Arr}, respectively)

In the remainder of this chapter, we apply this transfer methodology to the actual mission design problem, particularly to JAXA's Martian Moons eXploration mission.

4.3 Phobos Proximity QSO transfers: Application to Martian Moons eXploration mission

In this section, we identify the MP-QSO families that satisfy the necessary condition to implement the proposed transfer methodology. We will also develop transfer maps between baseline QSO orbits while recording MP-QSO family members that intersect both of the departing and arrival orbits. The results of numerical analysis presented in the next section show that minimum ΔV_{total} values of transfer occur for the maximum value of C_2 whilst 1) the departing and arrival points are almost equal to the maximum values of $\mathcal{W}(\boldsymbol{r}_1)$ and $\mathcal{W}(\boldsymbol{r}_3)$ (i.e., near the positive and negative $y-$axis), and 2) ϕ_{Dep} and ϕ_{Arr} are as close as possible to zero or tangential.

4.3.1 Identification of MP-QSOs connecting planar QSOs

Given the infinite number of $d:n$ bifurcations that exist across the nominal QSO family, we constrain $d:n$ bifurcations up to a multiplicity of 10 to limit the number of revolution of candidate MP-QSOs around Phobos. The $d:n$ ratios of MP-QSOs as a function of their respective Jacobi integral are illustrated in Fig. 4.2, whereas the period-multiplying bifurcated branches of MP-QSOs from the nominal QSO family solution space are shown in Fig. 4.3.

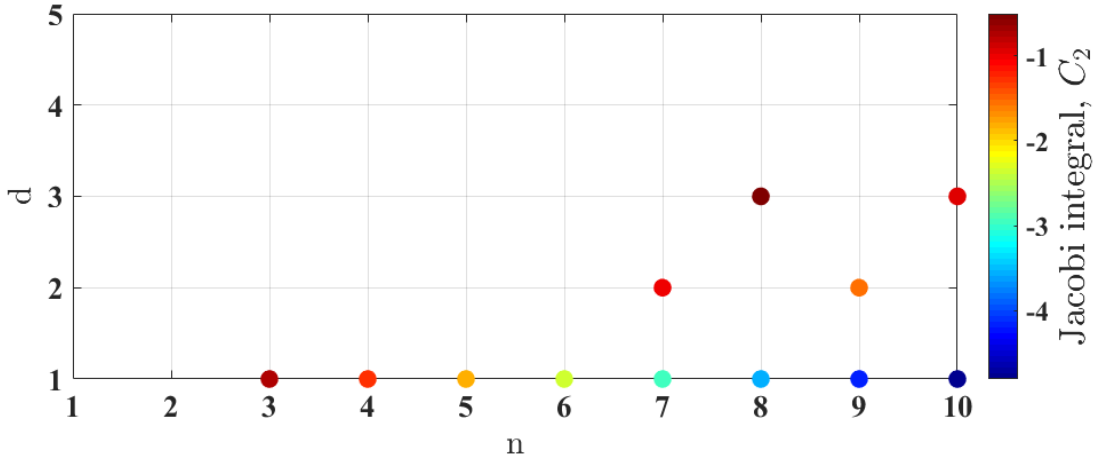

Figure 4.2: $d:n$ ratios as a function of their Jacobi integral value at the time of bifurcation

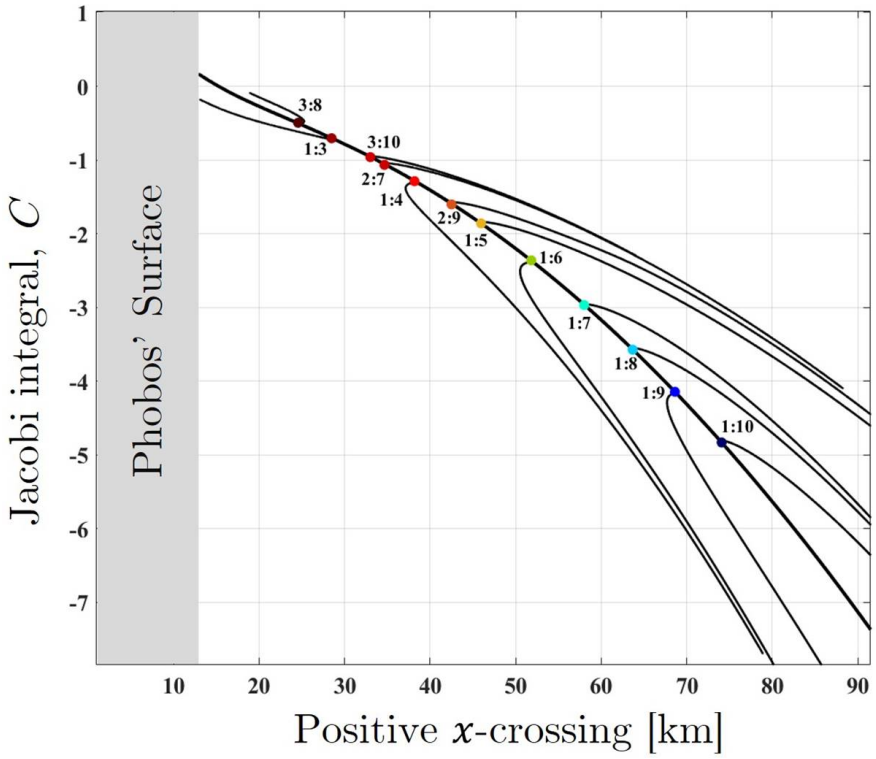

Figure 4.3: Bifurcated family branches from planar QSO family.

During the baseline operations of MMX, the altitude of the spacecraft will be varied to perform various scientific operations and gradually characterize the gravity field of Phobos. In particular, MMX will be transferred from high to low-altitude QSOs (i.e., A_x = 100 km to 20 km) using the following sequences: QSO-H → QSO-M; QSO-M → QSO-La; QSO-La → QSO-Lb; QSO-Lb → QSO-Lc (refer Table 3.1 for the QSO specifications). In this section, we use candidate $d : n$ MP-QSO family members to develop transfer maps and design transfer trajectories between MMX baseline QSOs (see [?] and references therein). We concentrate on those MP-QSO family members that intersect both of the departing and arrival orbits. Fig. 4.5 shows the positive y-axis crossings of the candidate $d : n$ MP-QSO family branches, revealing which of the considered MP-QSO families can be considered for further analysis. We notice that a variety of $d : n$ MP-QSOs intersect the MMX baseline orbits, including 3:8, 1:3, 3:10, 2:7, 1:4, 2:9, 1:5, 1:6, 1:7, 1:8, 1:9, and 1:10 MP-QSOs . Some of these bifurcated trajectories also cross multiple baseline orbits, enabling their utilization for different transfer opportunities and phases. For example, Fig.4.4(a) is the $+y$ amplitude variation map

of 1:4 MP-QSO families (i.e., positive y crossings of each computed members of the MP-QSO) computed from the bifurcation point (b_{Res} at d:n =1:4). We observe that 1:4 MP-QSOs intersect both QSO-Lb and QSO-Lc with a C_2 value between -7.697 and -2.585. The same bifurcated family is also intersecting both QSO-H and QSO-M with $C_2 \in [-7.697, -3.759]$ indicating utilization of same orbit to inject spacecrafts at different altitude QSOs (see Fig.4.4(b)). $+y$ amplitude variation maps of some of the other MP-QSO families are depicted in Fig. 4.5. 3:8 MP-QSOs are the families closest to the surface of Phobos and found to connect only QSO-Lb and QSO-Lc (Fig.4.5(a)) between $C_2 \in [-0.421, -0.092]$. Likewise, 1:3 MP-QSO families intersect QSO-La, QSO-Lb and QSO-Lc as shown in Fig.4.5(b), 3:10 MP-QSO families intersect QSO-M with other lower altitude QSOs (Fig.4.5(c)), and 2:7 MP-QSO can connect all of the baseline QSOs similar to that of 1:4 MP-QSO family (Fig.4.5(d)). Looking at Fig. 4.5, we find that the $+y$ amplitude variations of MP-QSO families increases as the values of C_2 corresponding to the MP-QSO family decreases.

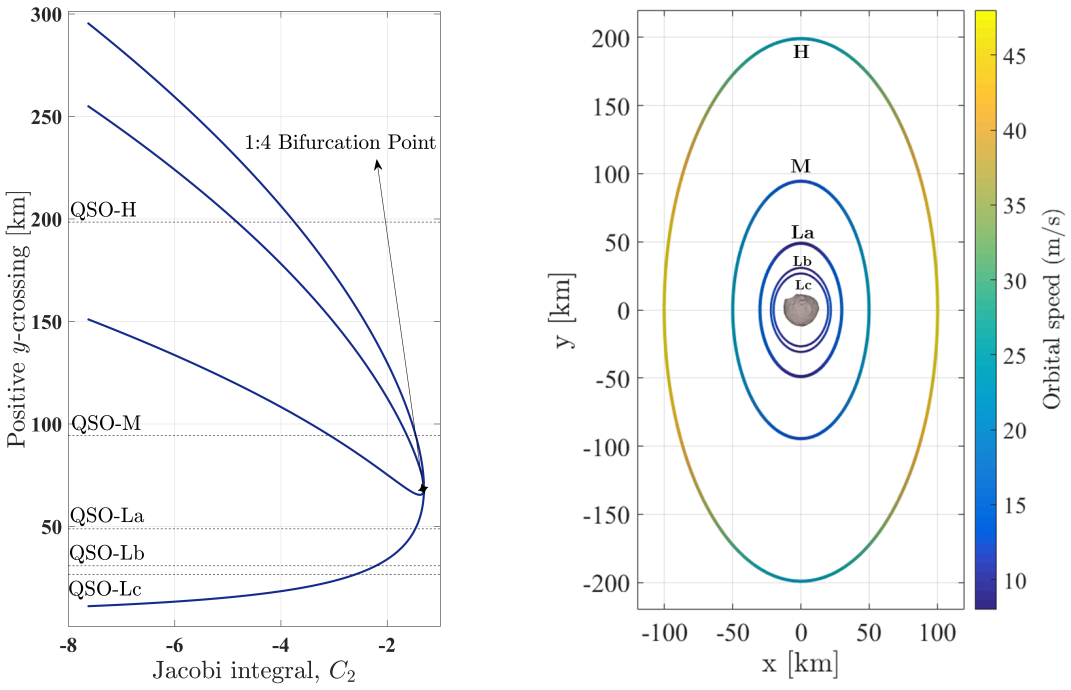

Figure 4.4: a)$+y$ amplitude variation map of 1:4 MP-QSO family; b) Baseline MMX orbits along with orbital velocity.

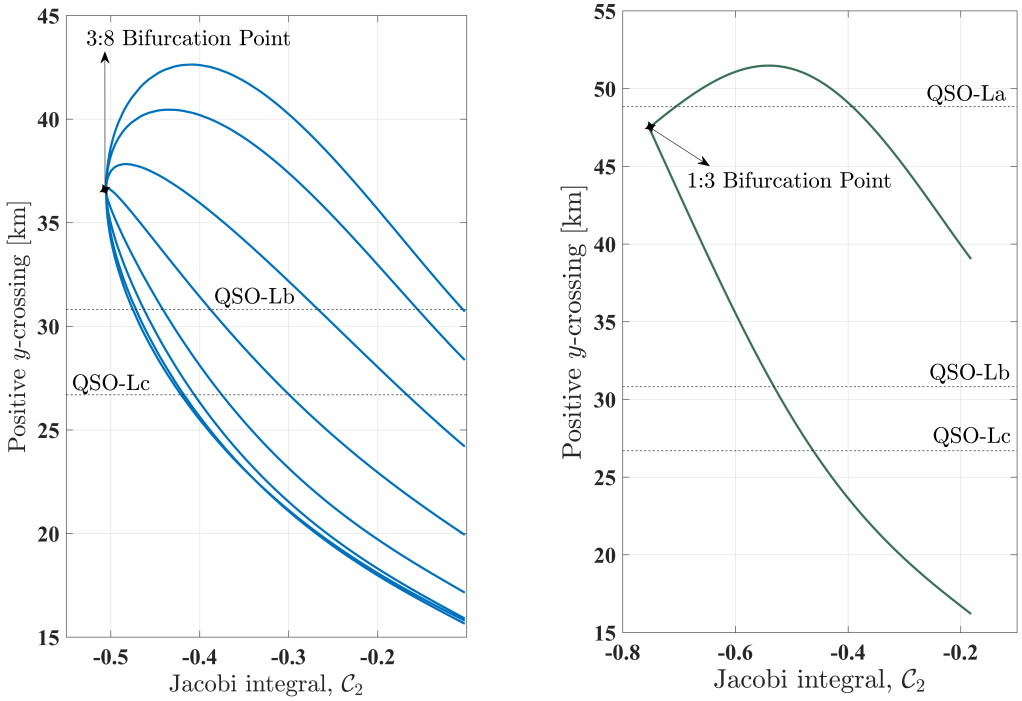

(a) 3:8 MP-QSO family

(b) 1:3 MP-QSO family

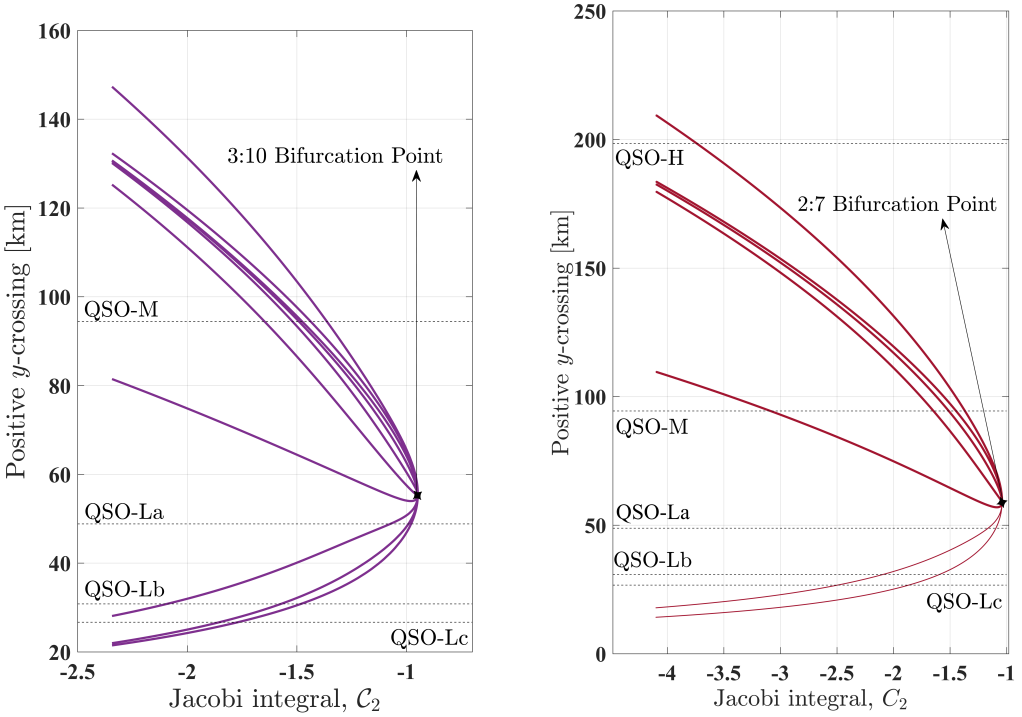

(c) 3:10 MP-QSO family

(d) 2:7 MP-QSO family

Figure 4.5: $+y$ amplitude variation maps of some candidate MP-QSO families.

The ranges of C_2 [$C_{2,i}$ to $C_{2,f}$] of other families of MP-QSOs intersecting MMX orbits at different transfer stages are tabulated in Tables 4.1 to 4.4. Once the ranges of the Jacobi integrals C_2 are established, we can compute and create transfer maps to connect higher altitude QSOs with lower altitude QSOs. The minimum ΔV_{total} enlisted in Tables 4.1 to 4.4 are extracted from the computed transfer maps for each candidate MP-QSO families.

4.3.2 Transfers between QSO-H to QSO-M

The transfer analysis between the highest altitude QSOs is carried out in the following manner. Firstly, we initialize the departing and arrival QSOs as QSO-H (C_1 = -8.78) and QSO-M (C_3 = -2.20), respectively. Secondly, we utilize candidate $d : n$ MP-QSOs to compute the whole set of MP-QSO trajectories that intersect with the departing and arrival orbits. Finally, we calculate ΔV_{total} and TOF values of the retrograde transfer trajectories and generate transfer maps as in Fig. 4.6 and Fig. 4.7. Transfer maps computed via MP-QSOs reveal the suitable longitudes at the departing (x-axis) and arrival (y-axis) QSOs around Phobos with ΔV_{total} of the transfers. Note that the transfer map patterns produced by the combination of departing and arrival QSOs are unique with respect to the MP-QSO used for the transfer. The minimum ΔV_{total} of each transfer candidate $d : n$ MP-QSO families is extracted from the transfer maps and listed in Table **??** along with the corresponding TOF, ϕ_{Dep}, ϕ_{Arr}, effective potentials $\mathcal{W}(\boldsymbol{r}_1)$ and $\mathcal{W}(\boldsymbol{r}_3)$ values. Note that C_2^* denotes the Jacobi integral value of the min ΔV_{total} transfer $d : n$ MP-QSO. It is observed that ΔV_{total} is minimized by MP-QSOs with the maximum value of the Jacobi integral as long as 1) $\mathcal{W}(\boldsymbol{r}_1)$ and $\mathcal{W}(\boldsymbol{r}_3)$ are almost equal to their maximum values at QSO-H and QSO-M, 2) ϕ_{Dep} and ϕ_{Arr} are both almost tangential. We find that the MP-QSO families 1:10 and 1:7 have the minimum ΔV_{total} transfer costs of 11.63 m/s and 11.72 m/s among the selected candidate MP-QSO families with a TOF of 4.17 hrs and 4.37 hrs, respectively. The total flight-path angle differences ($\phi_{Dep} + \phi_{Arr}$) were found to be equal to 14.17 deg and 15.37 deg. The minimum ΔV_{total} trajectories from the transfer maps Fig. 4.7(a) and (b) are shown in Fig. 4.12(a) and (b), respectively. Direct two-impulse transfers between QSOs of x-amplitudes 100 km and 50 km require a $\Delta V_{total} \approx$ 15 m/s [76] in the framework of Mars-Phobos CRTBP. On the other hand, present transfers via MP-QSOs require a $\Delta V_{total} \approx$ 11-16 m/s.

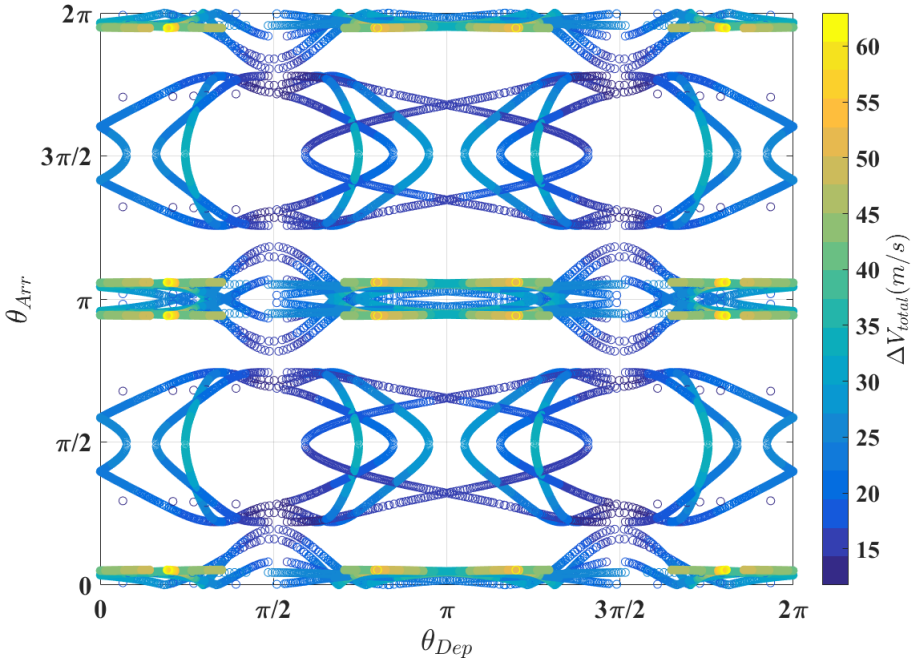

(a) 1:8 MP-QSO

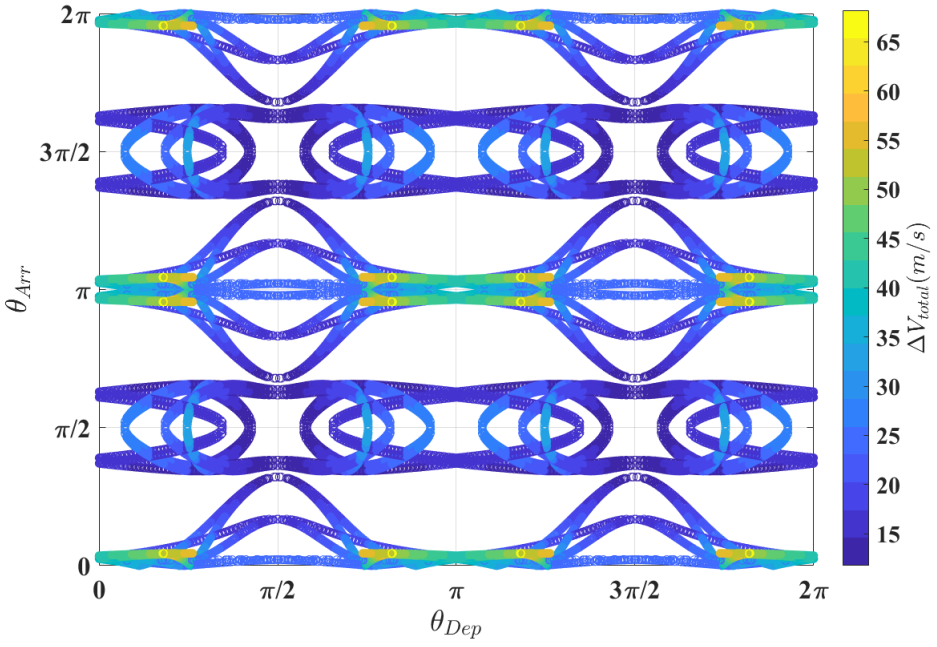

(b) 1:9 MP-QSO

Figure 4.6: Transfer maps between QSO-H and QSO-M via MP-QSOs (1:8 and 1:9)

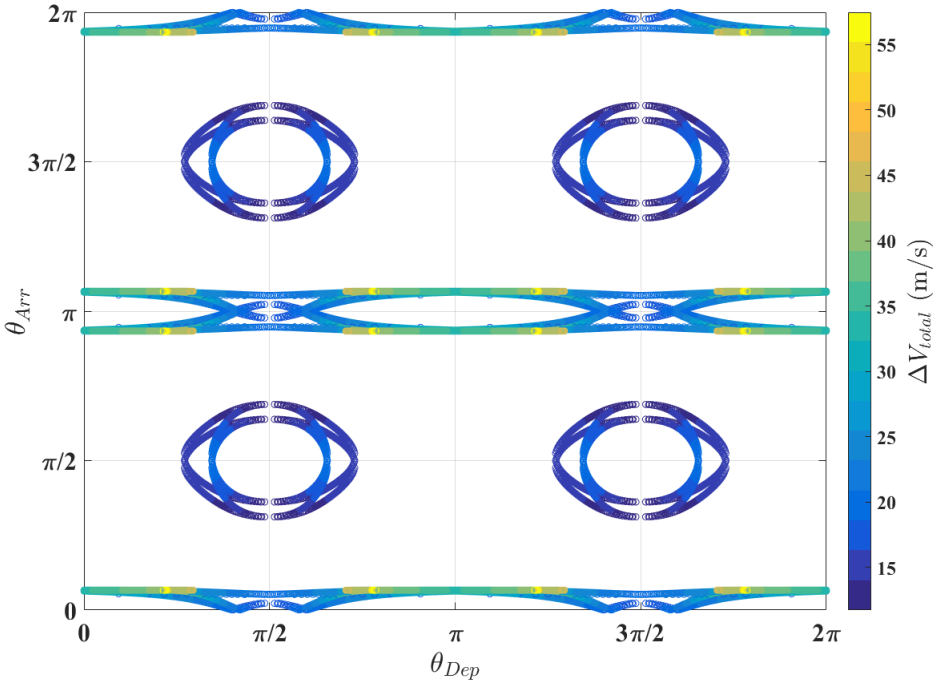

(a) 1:7 MP-QSO

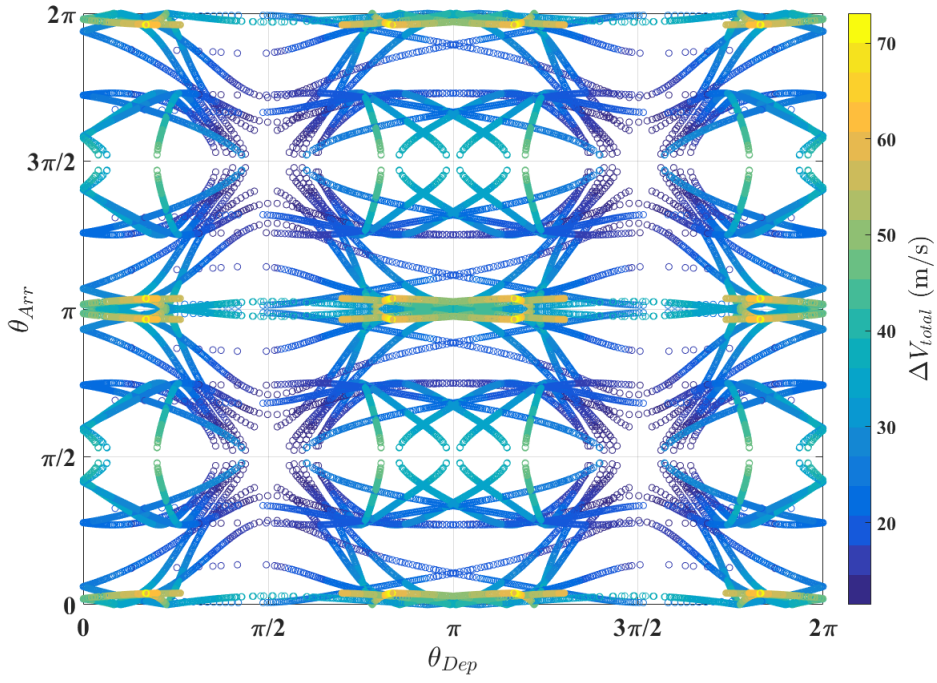

(b) 1:10 MP-QSO

Figure 4.7: Transfer maps between QSO-H and QSO-M via MP-QSOs (1:7 and 1:10)

Table 4.1: Transfer between QSO-H and QSO-M via candidate MP-QSOs.

MP-QSO $d:n$	Range of Jacobi, C_2 $[C_{2,i}$ to $C_{2,f}]$	C_2^*	$\mathcal{W}(\boldsymbol{r}_1)$	$\mathcal{W}(\boldsymbol{r}_3)$	ϕ_{Dep} (deg)	ϕ_{Arr} (deg)	Min ΔV_{total} (m/s)	TOF (hrs)	$\phi_{Dep}+\phi_{Arr}$ (deg)
2:7	[-3.571 to -5.042]	-5.041	18.488	6.308	2.03	31.35	16.68	14.23	33.38
1:4	[-3.759 to -7.697]	-5.270	26.631	6.349	0.27	32.16	16.32	4.34	32.43
2:9	[-3.691 to -5.394]	-5.275	26.741	6.355	0.17	32.13	16.30	4.38	32.30
1:5	[-3.162 to −9.705]	-5.423	26.683	6.652	0.21	29.96	15.60	4.37	30.18
1:6	[-3.679 to -13.402]	-4.194	3.298	5.803	8.65	12.01	12.22	12.38	20.66
1:7	[-4.012 to -16.548]	-4.012	0.682	4.385	5.59	9.78	11.72	4.37	15.37
1:8	[-4.230 to -19.153]	-7.070	26.522	4.748	0.15	21.44	11.75	21.11	21.59
1:9	[-4.702 to -22.317]	-5.493	1.940	3.177	4.35	15.07	11.76	3.46	19.43
1:10	[-5.295 to -25.064]	-5.495	4.874	0.552	7.27	6.90	11.63	4.17	14.17

Table 4.2: Transfer between QSO-M and QSO-La via candidate MP-QSOs.

MP-QSO $d:n$	Range of Jacobi, C_2 $[C_{2,i}$ to $C_{2,f}]$	C_2^*	$\mathcal{W}(\boldsymbol{r}_1)$	$\mathcal{W}(\boldsymbol{r}_3)$	ϕ_{Dep} (deg)	ϕ_{Arr} (deg)	Min ΔV_{total} (m/s)	TOF (hrs)	$\phi_{Dep}+\phi_{Arr}$ (deg)
3:10	[-1.363 to -2.297]	-1.528	7.011	2.782	0.17	12.70	4.53	23.87	12.87
2:7	[-1.368 to -5.042]	-1.547	7.083	2.785	0.02	12.99	4.59	14.13	13.01
1:4	[-1.468 to -7.697]	-1.468	0.892	0.497	4.03	1.01	3.99	3.81	5.04
2:9	[-1.812 to -5.394]	-1.901	5.564	0.556	2.34	3.26	4.15	11.69	5.60
1:5	[-2.415 to −9.705]	-2.415	5.879	0.595	11.69	4.96	8.87	9.03	16.65
1:6	[-3.099 to -13.402]	-3.099	7.014	0.486	9.19	3.42	9.86	8.60	12.62
1:7	[-4.012 to -16.548]	-4.012	4.388	0.516	9.78	5.91	12.04	8.15	15.69
1:8	[-5.112 to -19.153]	-5.112	5.915	0.518	18.13	7.34	17.82	8.23	25.48
1:9	[-6.137 to -22.317]	-6.137	3.653	0.480	17.44	2.65	19.51	8.06	20.10
1:10	[-7.488 to -25.064]	-7.488	5.459	0.506	24.98	7.00	25.32	8.13	31.99

Table 4.3: Transfer between QSO-La and QSO-Lb via candidate MP-QSOs.

MP-QSO $d:n$	Range of Jacobi, C_2 $[C_{2,i}$ to $C_{2,f}]$	C_2^*	$\mathcal{W}(\boldsymbol{r}_1)$	$\mathcal{W}(\boldsymbol{r}_3)$	ϕ_{Dep} (deg)	ϕ_{Arr} (deg)	Min ΔV_{total} (m/s)	TOF (hrs)	$\phi_{Dep}+\phi_{Arr}$ (deg)
1:3	[-0.181 to -0.544]	-0.544	1.731	2.330	5.89	0.08	1.74	4.53	5.98
3:10	[-1.479 to -2.297]	-1.479	2.739	0.740	11.76	0.39	6.67	18.96	12.15
2:7	[-1.592 to -5.042]	-1.592	2.842	0.740	13.85	0.66	9.62	9.19	14.51
1:4	[-2.210 to -7.697]	-2.210	3.047	0.745	22.56	0.78	11.90	0.67	23.35
2:9	[-2.504 to -5.394]	-2.504	2.601	0.754	22.36	1.96	12.54	17.26	24.32
1:5	[-3.799 to −9.705]	-3.799	2.876	0.741	28.93	1.44	18.13	7.96	30.38
1:6	[-4.384 to -13.402]	-4.384	2.731	0.750	32.67	3.29	20.64	17.84	35.96
1:7	[-5.631 to -16.548]	-5.631	2.612	0.747	36.43	3.55	24.80	25.65	39.99
1:8	[-6.933 to -19.153]	-6.933	2.566	0.750	38.56	4.09	28.51	25.81	42.66
1:9	[-8.315 to -22.317]	-8.315	2.494	0.744	40.95	3.25	32.27	33.56	44.21
1:10	[-9.884 to -25.064]	-9.884	2.436	0.743	43.03	3.29	36.06	34.28	46.33

Table 4.4: Transfer between QSO-Lb and QSO-Lc via candidate MP-QSOs.

MP-QSO $d:n$	Range of Jacobi, C_2 [$C_{2,i}$ to $C_{2,f}$]	C_2^*	$\mathcal{W}(r_1)$	$\mathcal{W}(r_3)$	ϕ_{Dep} (deg)	ϕ_{Arr} (deg)	Min ΔV_{total} (m/s)	TOF (hrs)	$\phi_{Dep}+\phi_{Arr}$ (deg)
3:8	[-0.092 to -0.421]	-0.394	0.850	1.059	3.11	2.02	0.97	6.29	5.13
1:3	[-0.181 to -0.544]	-0.482	1.705	2.234	8.63	0.11	2.20	1.47	8.74
3:10	[-1.767 to -2.297]	-1.767	1.421	0.848	16.96	0.68	9.13	9.71	17.64
2:7	[-1.863 to -5.042]	-1.863	1.574	0.848	19.33	0.88	9.89	9.75	20.21
1:4	[-2.585 to -7.697]	-2.585	1.521	0.848	21.66	0.53	12.96	0.29	22.19
2:9	[-2.802 to -5.394]	-2.802	1.512	0.857	22.22	1.68	13.83	10.09	23.90
1:5	[-4.456 to −9.705]	-4.456	1.461	0.849	25.05	1.46	19.70	7.72	26.51
1:6	[-4.998 to -13.402]	-4.998	1.363	0.848	26.98	2.05	21.67	26.17	29.03
1:7	[-6.389 to -16.548]	-6.389	1.308	0.848	28.75	1.24	25.89	26.31	29.99
1:8	[-7.772 to -19.153]	-7.772	1.306	0.854	29.77	4.39	29.65	33.99	34.17
1:9	[-9.289 to -22.317]	-9.289	1.271	0.849	30.69	1.77	33.46	33.79	32.46
1:10	[-10.930 to -25.064]	-10.930	1.270	0.855	31.40	4.00	37.26	34.12	35.40

4.3.3 Transfers between QSO-M to QSO-La

In this subsection, transfer maps between QSO-M (C_1 = -2.20) and QSO-La (C_3 = -0.78) are calculated using intersecting $d:n$ MP-QSO families. Figs. 4.4(a) and 4.5 suggest that 3:10, 2:7, and 1:4 MP-QSOs families may contain more efficient transfer orbits from QSO-M to QSO-La. In addition to these candidate transfer orbits, other MP-QSO families are summarized in Table 4.2 following the same rationale of the previous subsection. Unlike QSO-H → QSO-M, only four MP-QSO families have the range of Jacobi integrals C_2 overlapping with $[C_1, C_3]$: 3:10, 2:7, 1:4 and 2:9. We find that transfer orbits outside of this Jacobi integral regime would require a higher propellant expenditure. Transfer maps via 1:4 and 2:9 MP-QSOs are illustrated in Fig. **??** as the most favorable candidates. It is confirmed that the minimum ΔV_{total} values of 3.99 m/s and 4.14 m/s are offered by the 1:4 MP-QSO and 2:9 MP-QSO families, respectively. Their TOF was found to be 3.81 hr and 11.69 hr, with a total flight-path-angle of 5.04 deg and 5.60 deg. It can also be noted that, despite having a similar total flight-path-angles at the departure and arrival points, the minimum transfer cost obtained with the 3:10 and 1:6 MP-QSO families are significantly different. This suggest that, if possible, transfer between candidate QSOs should occur at the highest possible value of C_2. The minimum ΔV_{total} retrograde transfer trajectories associated with this second transfer stage are shown in Fig. 4.12(c) and (d). We also find that, direct two-impulse transfers between QSO-M → QSO-La costs a $\Delta V_{total} \approx 6$ m/s [76], which is moderately larger than current transfer method using MP-QSOs.

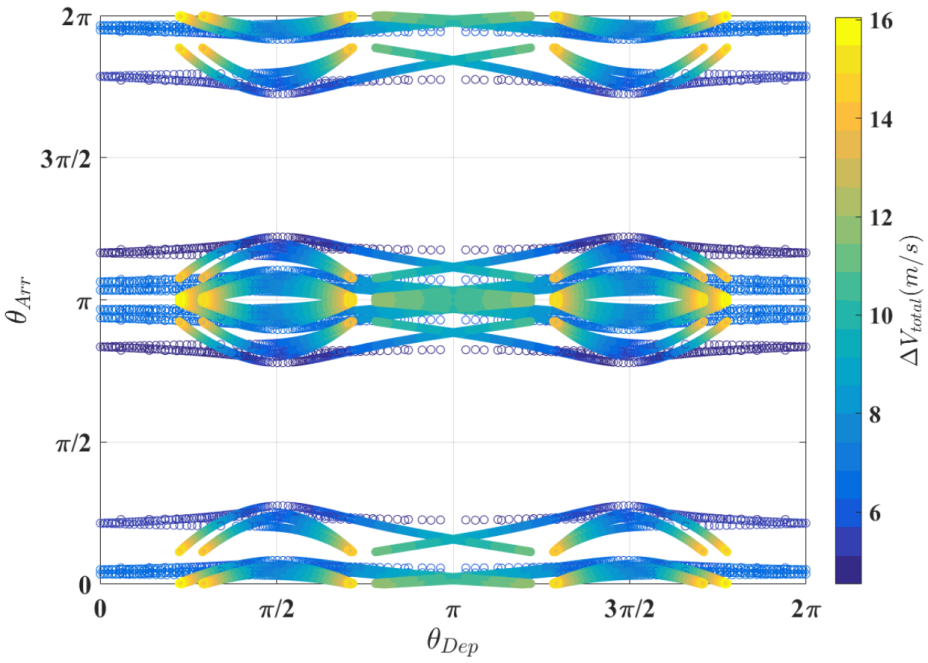

(a) 3:10 MP-QSO

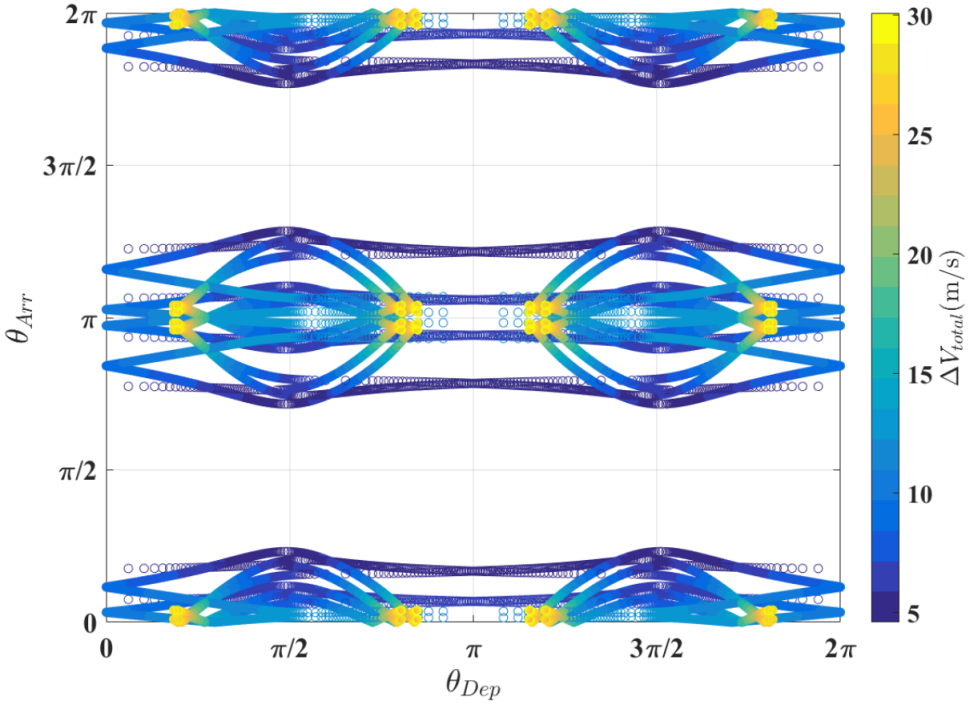

(b) 2:7 MP-QSO

Figure 4.8: Transfer maps between QSO-M and QSO-La via MP-QSOs (3:10 and 2:7)

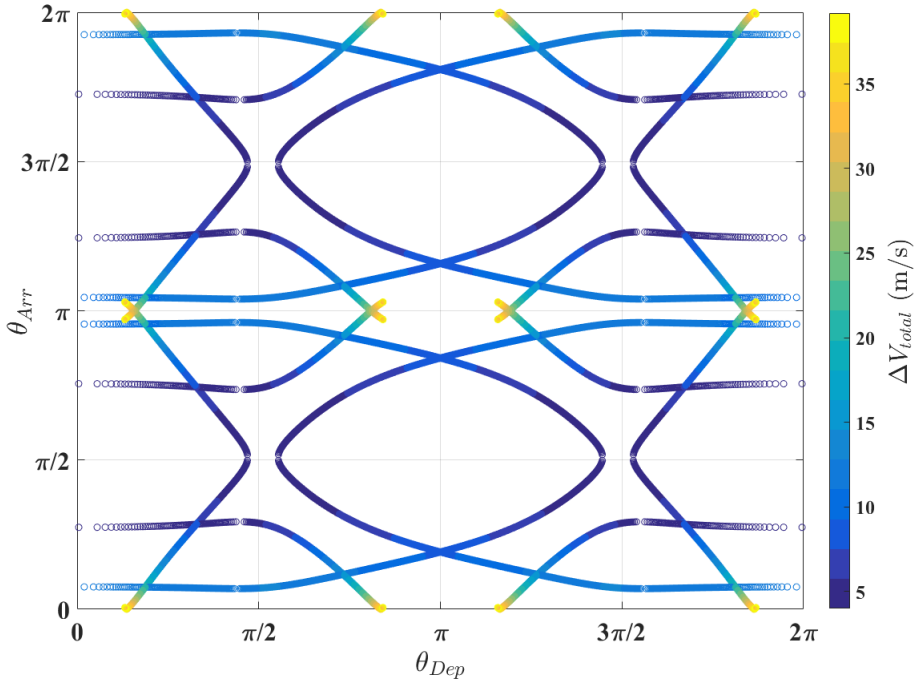

(a) 1:4 MP-QSO

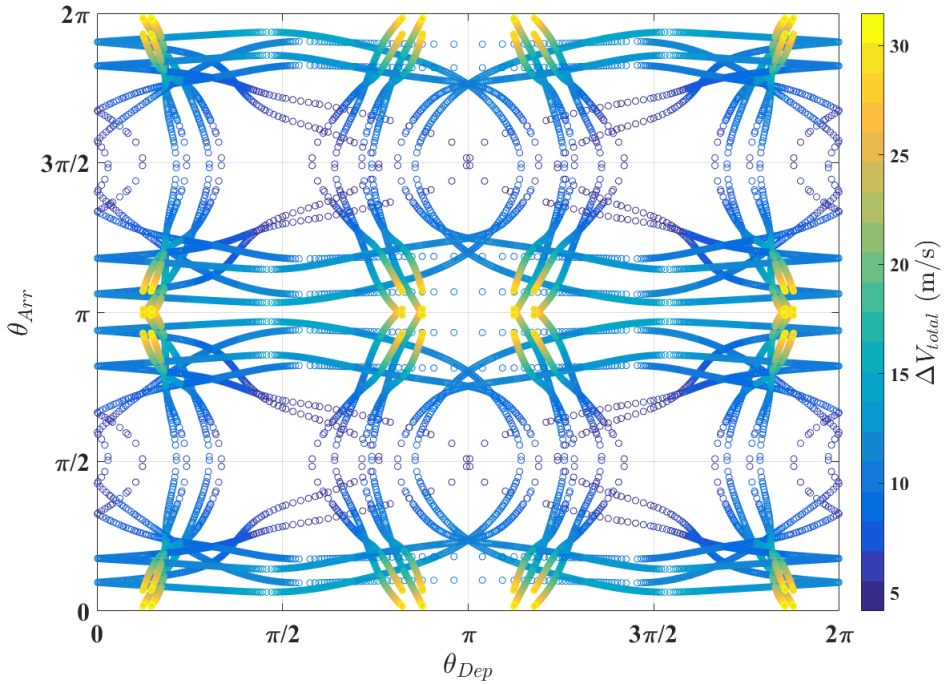

(b) 2:9 MP-QSO

Figure 4.9: Transfer maps between QSO-M and QSO-La via MP-QSOs (1:4 and 2:9)

4.3.4 Transfers between QSO-La to QSO-Lb

Potential transfer orbits between QSO-La (C_1 = -0.78) and QSO-Lb (C_3 = -0.37) are found using amplitude variation maps similar to the ones of Fig. 4.5. Differently from QSO-H → QSO-M and QSO-M → QSO-La, we find that 1:3 MP-QSOs may also be considered for transfer analyses. The range of Jacobi integrals of transfer orbits intersecting the departing and arrival orbits are tabulated in Table 4.3, whereas transfer maps showing retrograde transfer trajectories connecting QSO-La and QSO-Lb via 1:3 and 3:10 MP-QSOs are shown in Fig. 4.10. As it can be seen from both Table 4.3 and Fig. 4.10, 1:3 MP-QSOs yield the minimum values of ΔV_{total}. It is found that 1:3 MP-QSO is the only family with transfer opportunities $\in [C_1, C_3]$ with C_2 ranging from -0.181 to -0.544. Table 4.3 also shows that there has been a gradual increase in both minimum ΔV_{total}, and total flight-path-angles associated with the other families of MP-QSOs. Examples of retrograde transfer orbits with minimum ΔV_{total} values are illustrated in the Fig. 4.12(e) and (f). We note that, transfers using 1:3 MP-QSO between QSO-La → QSO-Lb costs lower than that of the direct two-impulse transfer cost of $\Delta V_{total} \approx 3$ m/s [76].

4.3.5 Transfer between QSO-Lb to QSO-Lc

The final stage in the Phobos proximity phase of MMX is to place the spacecraft on a very-low altitude (x-amplitude $\leq$ 20 km) QSO before surface operations. The Jacobi integrals of low-altitude QSOs (x-amplitude $\leq$ 30 km) are larger when compared to the other MMX baseline QSOs and this affects the optimal selection of the MP-QSO transfer. In particular, we find that a new family, 3:8, may be considered for minimum-propellant QSO transfers. Similar to previous transfer stages, we design and develop transfer maps via MP-QSOs to connect QSO-Lb (C_1 = -0.37) and QSO-Lc (C_3 = -0.27). Table 4.4 provides the results starting with a preliminary evaluation of the available C_2 ranges. We find that 3:8 and 1:3 MP-QSOs are the most promising candidates for low-ΔV transfers. The transfer maps associated with QSO-Lb → QSO-Lc via 1:3 and 3:8 families are illustrated in Fig. 4.11. Transfers using 3:8 candidates seems more favorable as they produce almost tangential transfers connecting QSO-Lb and QSO-Lc. Results of transfer trajectories via MP-QSO families suggest that the minimum ΔV_{total} along with the total flight-path-angle of transfers steadily increases from 3:8 to 1:10 MP-QSO.

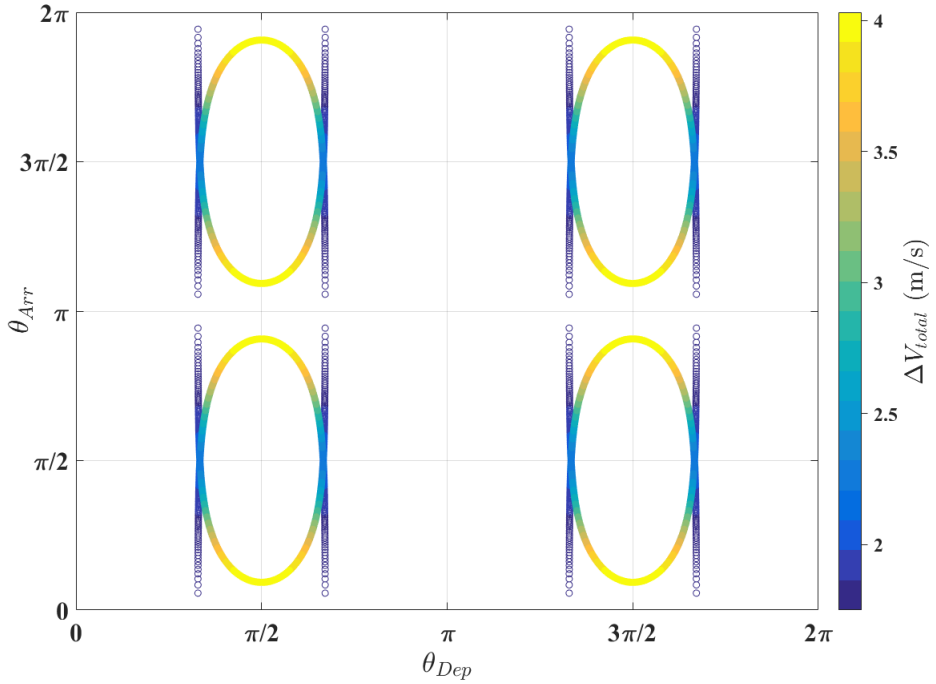

(a) 1:3 MP-QSO

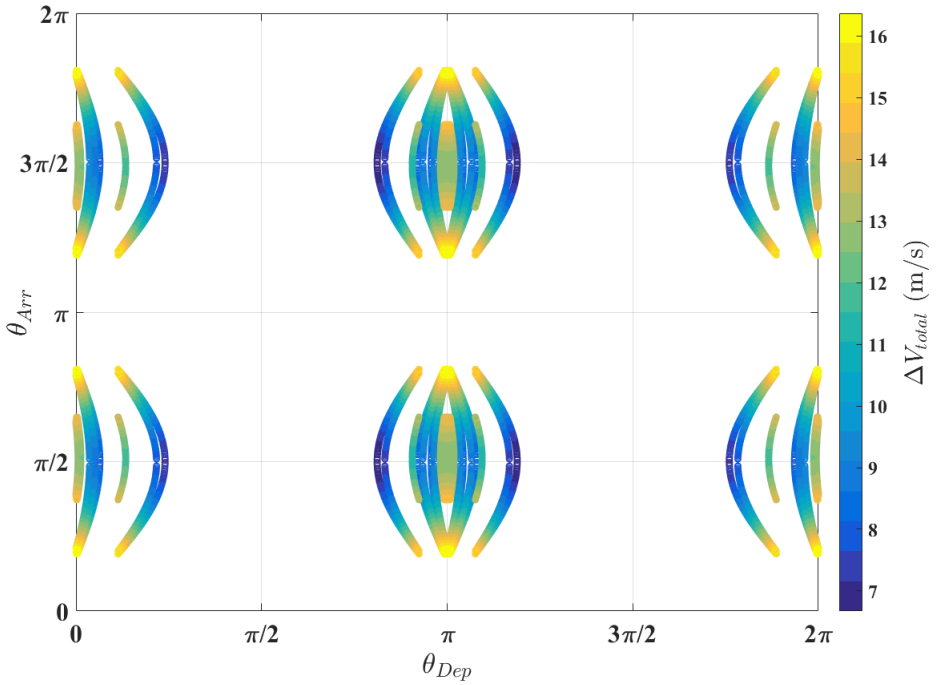

(b) 3:10 MP-QSO

Figure 4.10: Transfer maps between QSO-La and QSO-Lb via MP-QSOs(1:3 and 3:10)

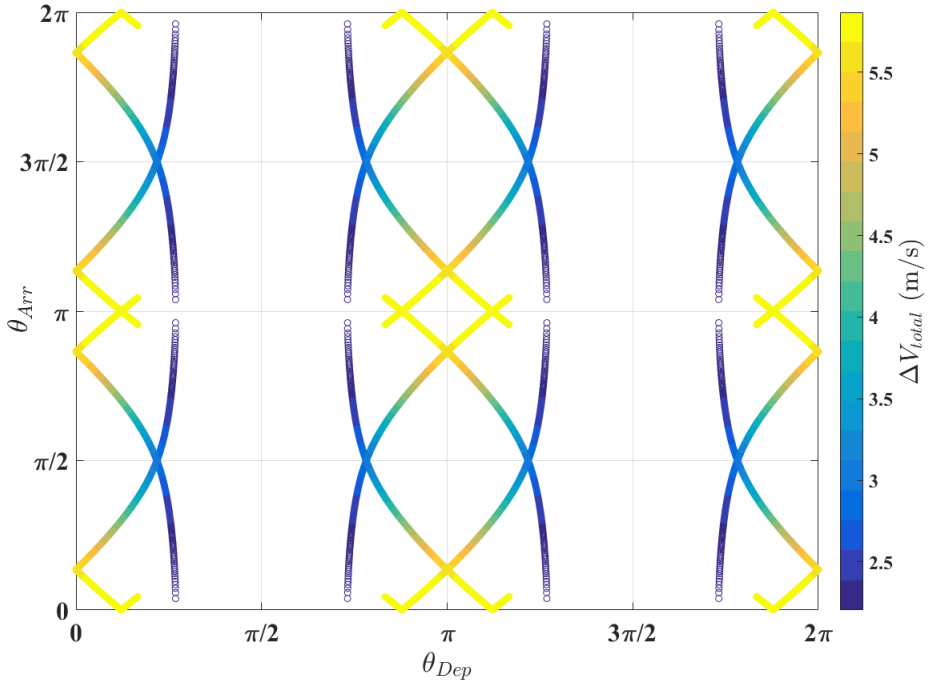

(a) 1:3 MP-QSO

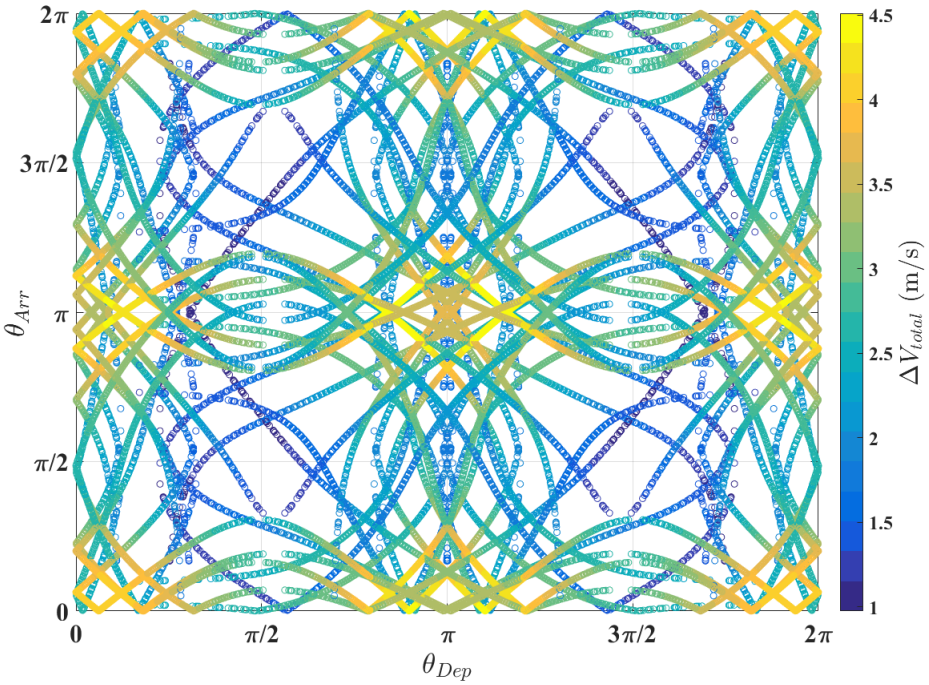

(b) 3:8 MP-QSO

Figure 4.11: Transfer maps between QSO-Lb and QSO-Lc via MP-QSOs(1:3 and 3:8)

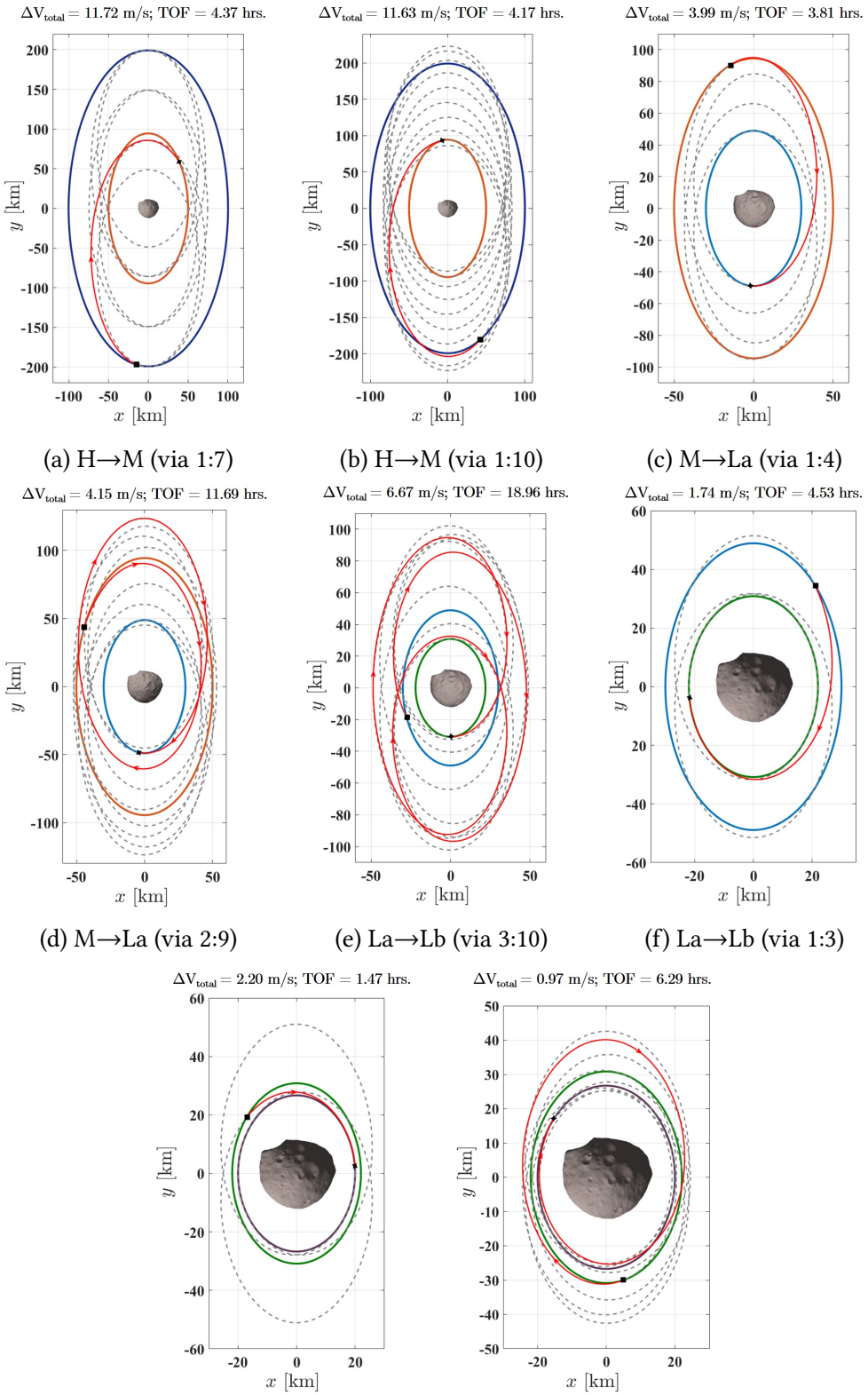

(a) H→M (via 1:7) (b) H→M (via 1:10) (c) M→La (via 1:4)

(d) M→La (via 2:9) (e) La→Lb (via 3:10) (f) La→Lb (via 1:3)

(g) Lb→Lc (via 1:3) (h) Lb→Lc (via 3:8)

Figure 4.12: Transfer trajectories using MP-QSOs between candidate MMX QSOs.

The minimum retrograde transfer ΔV_{total} cases between QSO-Lb and QSO-Lc are illustrated in the Fig. 4.12(g) to (h). We find that 3:8 MP-QSO has the minimum ΔV_{total} of 0.97 m/s in 6.29 hr (Fig. 4.12(h)) and 1:3 MP-QSO with a minimum ΔV_{total} of 2.20 m/s in 1.47 hr (Fig. 4.12(g)) with total flight-path-angle of 5.13 deg and 8.74 deg, respectively. We also note that total flight-path-angles of families 3:8 and 1:3 are much lower than that of other MP-QSO families and 3:8 provide almost similar ΔV_{total} cost approximately 1 m/s of the direct two-impulse transfer between QSOs of similar altitudes [76].

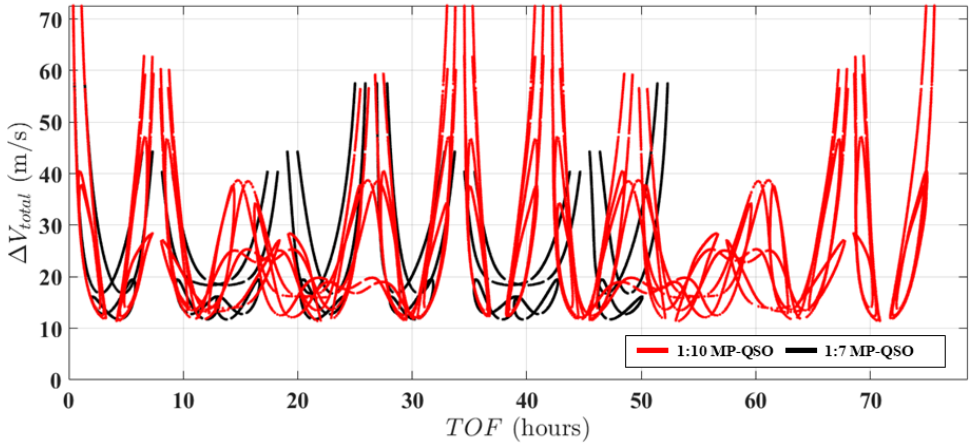

Figure 4.13: TOF vs ΔV_{total} for QSO-H to QSO-M transfer (1:7 and 1:10 MP-QSOs)

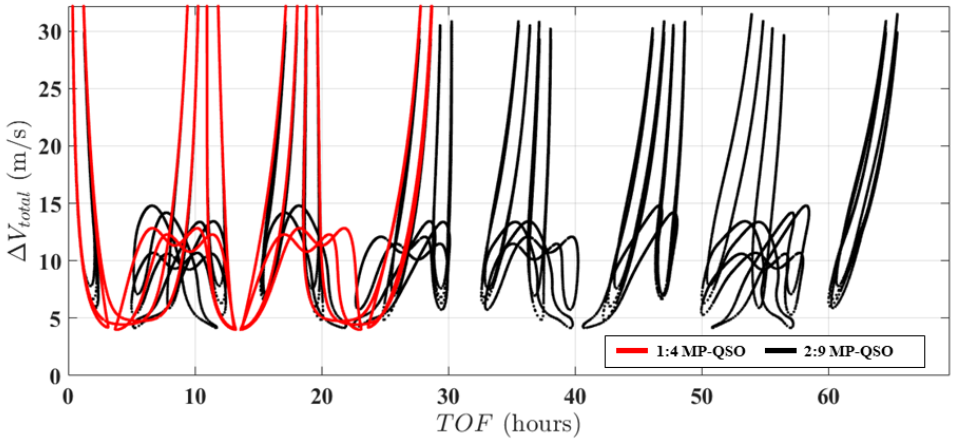

Figure 4.14: TOF vs ΔV_{total} for QSO-M to QSO-La transfer (1:4 and 2:9 MP-QSOs)

4.3.6 Summary of the in-plane transfers

The numerical analysis of the previous subsections are hereby summarized to present the Pareto front of different QSO transfers in the ΔV_{total} vs TOF parameter space. As seen in the QSO-M $\rightarrow$ QSO-La case, the Jacobi integral of the orbit transfer does play a role in minimizing ΔV_{total} values while reducing the flight-path-angles to almost tangential trajectories. Numerical analyses are also suggests that the minimum ΔV_{total} cost across candidate 3:8 MP-QSO to 1:10 MP-QSO families does increase as we gradually reduce the altitude of MMX around Phobos. This is evident from the plots of Fig. 4.13 to 4.16, showing the overall ΔV_{total} vs. TOF transfer solution space between the MMX baseline QSOs. In these plots, only the two most appropriate MP-QSO candidates producing low-ΔV transfers have been retained for the sake of illustration. The interested reader may refer to the values of Tables 4.1 to 4.4 for a more in-depth comparison. We note that C_2^* values presented in Tables 4.1 to 4.4 does not always fall within the limits C_1 and C_3 of departing and arrival QSOs due to the nature of MP-QSOs. For instance, in case of QSO-H $\rightarrow$ QSO-M, the values of C_2^* of all the candidate MP-QSOs fall in between C_1 and C_3. Whereas, in case of QSO-Lb $\rightarrow$ QSO-Lc, the C_2^* values of none of the candidate MP-QSOs fall in between C_1 and C_3. This clearly indicate that the value of C_2 alone does not determine the minimum ΔV_{total} of the transfer, but also the minimum total flight-path-angles of the transfer trajectories.

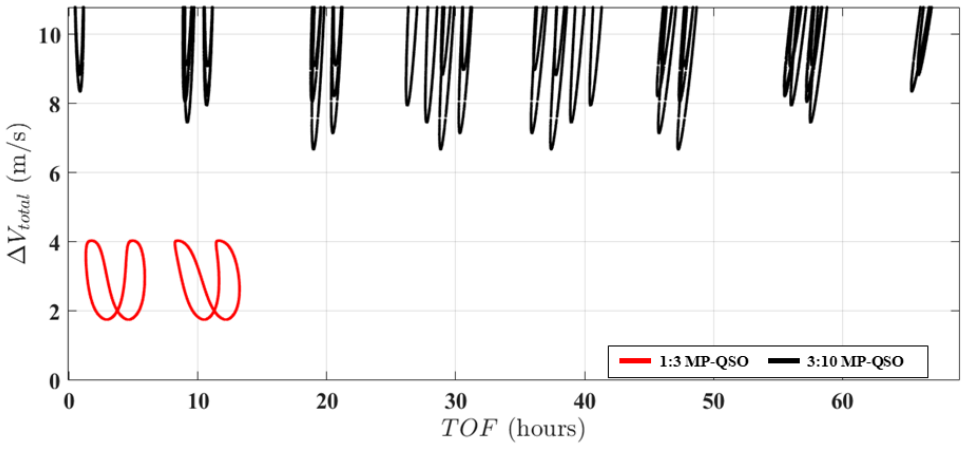

Figure 4.15: TOF vs ΔV_{total} for QSO-La to QSO-Lb transfer (1:3 and 3:10 MP-QSOs)

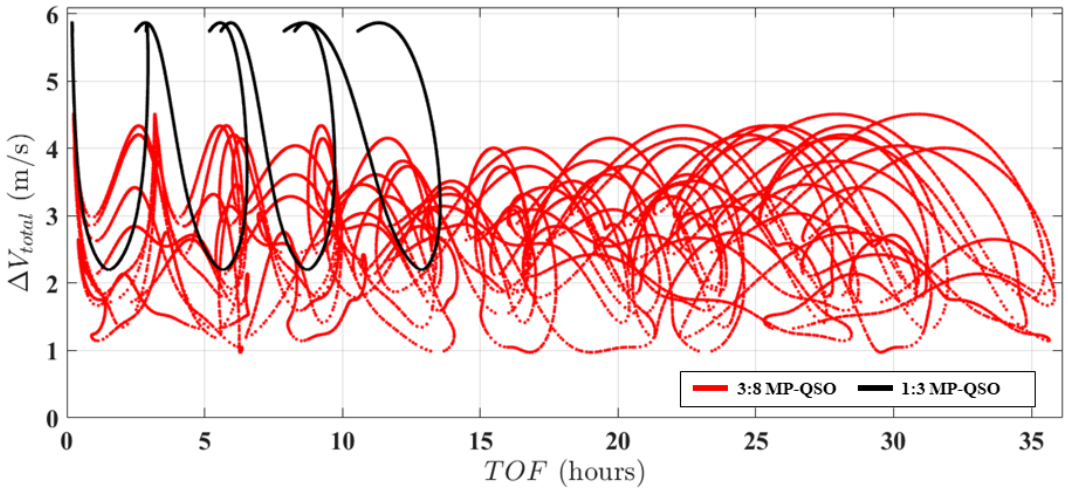

Figure 4.16: TOF vs ΔV_{total} for QSO-Lb to QSO-Lc transfer (3:8 and 1:3 MP-QSOs)

Table 4.5 provides a comparison of transfer costs computed through the presented transfer method via MP-QSOs (Hill Problem Ellipsoidal gravity framework) and a direct two-impulse transfers (CRTBP framework) between MMX baseline QSOs. It can be noted that transfer costs via MP-QSOs are cheaper than the direct 2-impulse transfers between the MMX candidate QSOs.

Table 4.5: Min ΔV_{total} transfer cost comparison

Transfer stage	Direct 2-impulse transfer (Ikeda et al.(2017))	Transfers via MP-QSOs (Current work)
QSO-H → QSO-M	15 m/s	11.63 m/s
QSO-M → QSO-La	6 m/s	3.99 m/s
QSO-La → QSO-Lb	3 m/s	1.74 m/s
QSO-Lb → QSO-Lc	1 m/s	0.97 m/s

4.4 Optimal Transfer Trajectories

In this section, to improve upon the identified transfer trajectories via MP-QSOs between MMX baseline orbits, this thesis use impulsive primer vector theory[90, 91, 92] to optimize these trajectories further. Primer vector theory uses the primer vector, a costate velocity vector, to evaluate if a trajectory satisfies the necessary analytical

conditions for optimality. If the necessary conditions are not satisfied, the theory indicates how the candidate trajectory should be modified to reduce its transfer cost which are discussed in the following subsections.

4.4.1 Impulsive Primer Vector Theory

Primer vector theory (PVT) is an indirect method of optimizing transfer trajectories with necessary conditions and sufficient conditions (if available)[93] derived from the indirect optimization of the fuel-minimum problem[91]. When impulsive transfer trajectories are used, the primer vector determines the timing and location of thrust impulses in order to minimize propellant cost.

PVT for impulsive transfer trajectories indicates whether adding an initial or final coast, a midcourse impulse, or changing the timing, magnitude, and direction of an already existing midcourse impulse can reduce the cost[94, 95].

For impulsive transfer, cost function representing minimum total ΔV can be defined as

$$J = \sum_{n=0}^{N} \Delta V_n \tag{4.5}$$

Initial deviations to the reference trajectory ($\delta\dot{\boldsymbol{x}}$) can be linearly mapped to specific time using the state transition matrix (STM) $\Phi(t, t_0)$[96, 97] as

$$\delta\dot{\boldsymbol{x}} = \begin{bmatrix} \delta\dot{\boldsymbol{r}} \\ \delta\dot{\boldsymbol{v}} \end{bmatrix} = \begin{bmatrix} O_3 & I_3 \\ G & O_3 \end{bmatrix} \begin{bmatrix} \delta\boldsymbol{r} \\ \delta\boldsymbol{v} \end{bmatrix} \tag{4.6}$$

where O_3 is 3×3 zero matrix, I_3 is 3×3 identity matrix, and G is 3×3 gravity gradient matrix. The elements of G are given by

$$g_{ij} = \partial^2\Phi / \partial x_i \partial x_j \tag{4.7}$$

Eq.(4.6) can be written in second-order form as

$$\delta\ddot{\boldsymbol{r}} = G\delta\boldsymbol{r} \tag{4.8}$$

STM of this system can be partitioned in to four 3×3 matrices as follows:

$$\Phi(t, t_0) \equiv \begin{bmatrix} \Phi_A(t, t_0) & \Phi_B(t, t_0) \\ \Phi_C(t, t_0) & \Phi_D(t, t_0) \end{bmatrix} \tag{4.9}$$

In order to minimize the cost function, we form Hamiltonian of the system, H using,

$$H = J + \boldsymbol{\lambda}_r^T \dot{\boldsymbol{r}} + \boldsymbol{\lambda}_v^T \dot{\boldsymbol{v}} \tag{4.10}$$

where $\dot{\boldsymbol{r}}$ and $\dot{\boldsymbol{v}}$ are velocity and acceleration of the spacecraft, and $\boldsymbol{\lambda}_r^T$ and $\boldsymbol{\lambda}_v^T$ are 3×1 vector Lagrange multipliers that includes the equations of motion as non-linear constraints for the optimization problem[98].

The adjoint system to Eq.(4.6) is

$$\begin{bmatrix} \dot{\boldsymbol{\lambda}}_r \\ \dot{\boldsymbol{\lambda}}_v \end{bmatrix} = \begin{bmatrix} O_3 & -G \\ -I_3 & O_3 \end{bmatrix} \begin{bmatrix} \boldsymbol{\lambda}_r \\ \boldsymbol{\lambda}_v \end{bmatrix} \tag{4.11}$$

Rewriting Eq.(4.11) in second-order form as

$$\ddot{\boldsymbol{\lambda}}_v = G\boldsymbol{\lambda}_v \tag{4.12}$$

is identical to Eq.(4.8), therefore STM for $(\boldsymbol{\lambda}_v, \dot{\boldsymbol{\lambda}}_v)$ will be identical to Eq.(4.9)

$$\begin{bmatrix} \boldsymbol{\lambda}_v(t) \\ \dot{\boldsymbol{\lambda}}_v(t) \end{bmatrix} = \Phi(t, t_0) \begin{bmatrix} \boldsymbol{\lambda}_v(t_0) \\ \dot{\boldsymbol{\lambda}}_v(t_0) \end{bmatrix} \tag{4.13}$$

Lawden[90] termed $\boldsymbol{\lambda}_v$ as the “primer vector " (i.e.,$\boldsymbol{\lambda}_v = \mathbf{p}$) and derived following necessary conditions for an optimal impulsive transfer trajectory.

- Primer vector and its derivative are continuous along the transfer trajectory.
- Primer vector magnitude satisfies $p(t) \leq 1$ with the ΔV impulses taking place at instants at which $p(t) = 1$.
- At impulse times, the primer vector is a unit vector in the optimal thrust direction.
- As a consequence of above conditions, $dp/dt = \dot{p} = \dot{\boldsymbol{p}}^T \boldsymbol{p} = 0$ at an intermediate impulse.

In linear systems, these necessary conditions are also the sufficient conditions for an optimal trajectory.

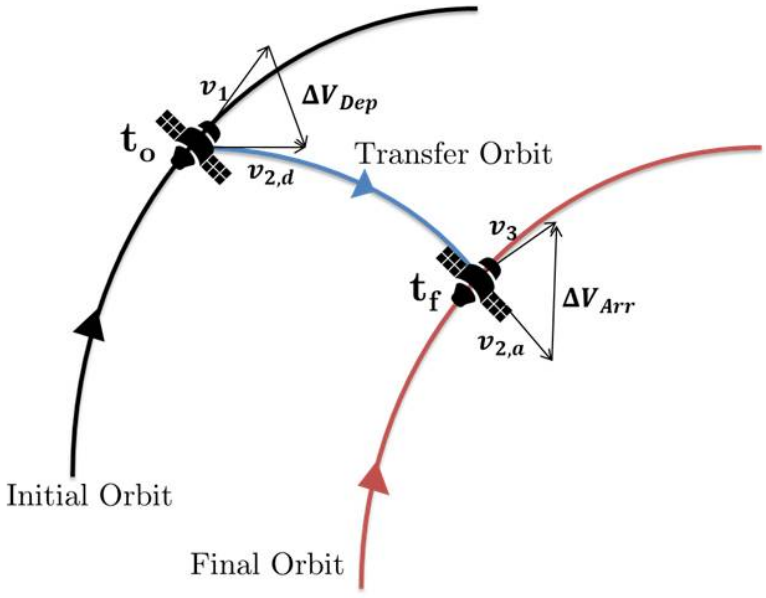

Figure 4.17: Illustration of a two-impulse transfer trajectory.

Let ΔV_{Dep} and ΔV_{Arr} be the change in velocity at initial and terminal QSOs as illustrated in Fig. 4.17.

To satisfy the necessary conditions for an optimal trajectory, we can impose following boundary conditions on the primer vector

$$\boldsymbol{p}(t_0) \equiv \boldsymbol{p}_0 = \frac{\Delta \boldsymbol{V_{Dep}}}{\Delta V_{Dep}} \tag{4.14}$$

$$\boldsymbol{p}(t_f) \equiv \boldsymbol{p}_f = \frac{\Delta \boldsymbol{V_{Arr}}}{\Delta V_{Arr}} \tag{4.15}$$

From Eq.(4.13), the primer vector can then be evaluated along the transfer orbit using a 6×6 state transition matrix solution,

$$\begin{bmatrix} \boldsymbol{p}(t) \\ \dot{\boldsymbol{p}}(t) \end{bmatrix} = \Phi(t, t_0) \begin{bmatrix} \boldsymbol{p}(t_0) \\ \dot{\boldsymbol{p}}(t_0) \end{bmatrix} \tag{4.16}$$

From Eq.(4.16) and Eq.(4.9) primer vector and its derivative at time $[t_0\ t_f]$ evaluated as

$$\boldsymbol{p}_f = \Phi_A(t_f, t_0)\boldsymbol{p}_0 + \Phi_B(t_f, t_0)\dot{\boldsymbol{p}}_0 \tag{4.17}$$

$$\dot{\boldsymbol{p}}_f = \Phi_C(t_f, t_0)\boldsymbol{p}_0 + \Phi_D(t_f, t_0)\dot{\boldsymbol{p}}_0 \tag{4.18}$$

From Eq.(4.17), we have initial primer vector derivative as

$$\dot{\boldsymbol{p}}_0 = \Phi_B^{-1}(t_f, t_0)[\boldsymbol{p}_f - \Phi_A(t_f, t_0)\boldsymbol{p}_0] \tag{4.19}$$

knowing primer vector and its derivative at the initial time, one can evaluate the primer vector along the transfer trajectory between $[t_0\ t_f]$ using

$$\dot{\boldsymbol{p}}(t) = \Phi_B(t, t_0)\Phi_B^{-1}(t_f, t_0)\boldsymbol{p}_f + [\Phi_A(t, t_0) - \Phi_B(t, t_0)\Phi_B^{-1}(t_f, t_0)\Phi_A(t_f, t_0)]\boldsymbol{p}_0 \tag{4.20}$$

Lion and Handelsman[94] proposed specific criterion that satisfy the necessary conditions for optimality when two-impulse transfer trajectories fail to satisfy the necessary conditions. Criterion for adding terminal coasts/earlier impulses and midcourse impulses are listed as follows[94, 99, 100]:

1. If $\dot{p}_0 > 0$, an initial coast will lower the transfer cost. Similarly, if $\dot{p}_f < 0$, a final coast will lower the cost.

2. If $\dot{p}_0 < 0$, implying an earlier impulse time would lower the cost (i.e., starting the transfer earlier). Likewise, $\dot{p}_f > 0$ implies an increase in transfer time lower the costs.

3. If p is greater than unity along the transfer trajectory, adding a midcourse impulse at a time when $p > 1$ reduces the transfer cost.

These are the criterion or optimality conditions for the QSO transfer analysis which follows.

4.4.2 Primer vector analysis for MMX baseline QSO transfer

This subsection analyzes the initial transfer trajectories computed from our transfer methods by applying impulse primer vector theory. Initially, we map the primer vector

magnitude and its derivative of the initial minimum ΔV cases from Table 4.6. The evaluation shows that primer vector magnitude history along the transfer trajectories for some cases of transfers is greater than unit magnitude.i.e., $p > 1$, and primer vector derivatives history suggest that the $\dot{p}$ at the impulse locations are either $\dot{p} > 0$ or $\dot{p} < 0$. These initial impulse transfer solution evaluations indicate that they do not satisfy the necessary conditions for an optimal impulse transfer trajectory. Therefore, we introduce terminal coasting times and mid-course impulses to achieve optimal transfers[94, 101].

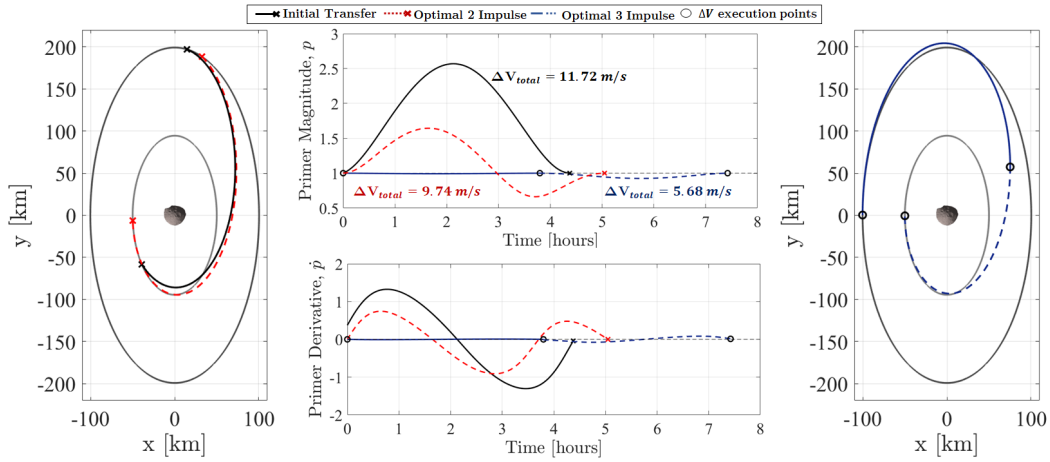

(a) Case 1

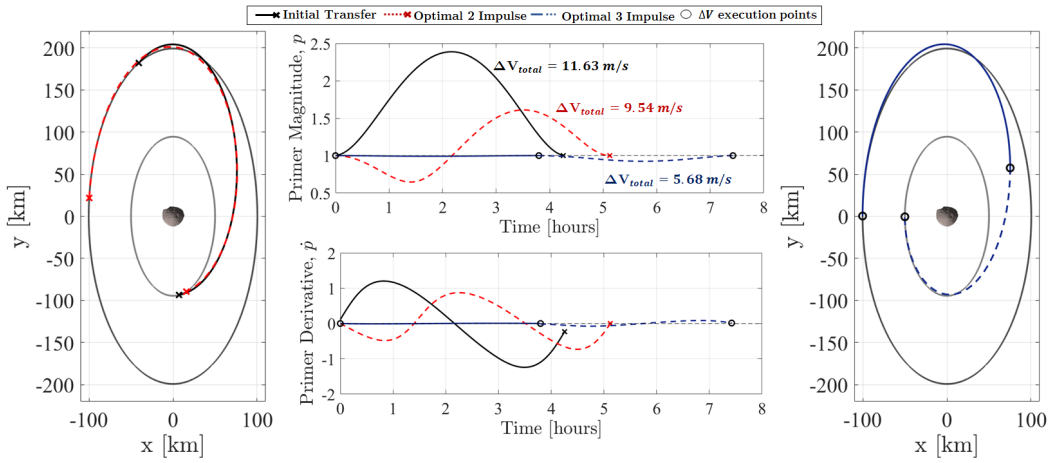

(b) Case 2

Figure 4.18: (a) QSO-H→QSO-M using initial guess from 1:7 MP-QSO transfer map. (b) QSO-H→QSO-M using initial guess from 1:10 MP-QSO transfer map.

Table 4.6: Transfer cases initial guess

Transfer	Case	Transfer Map	ΔV m/s	TOF (hours)
QSO-H→QSO-M	1	1:7 MP-QSO	11.72	4.37
	2	1:10 MP-QSO	11.63	4.25
QSO-M→QSO-La	3	1:4 MP-QSO	3.99	3.81
	4	2:9 MP-QSO	4.15	5.21
QSO-La→QSO-Lb	5	3:10 MP-QSO	6.67	18.95
	6	1:3 MP-QSO	1.74	2.84
QSO-Lb→QSO-Lc	7	1:3 MP-QSO	2.2	1.47
	8	3:8 MP-QSO	0.97	6.3

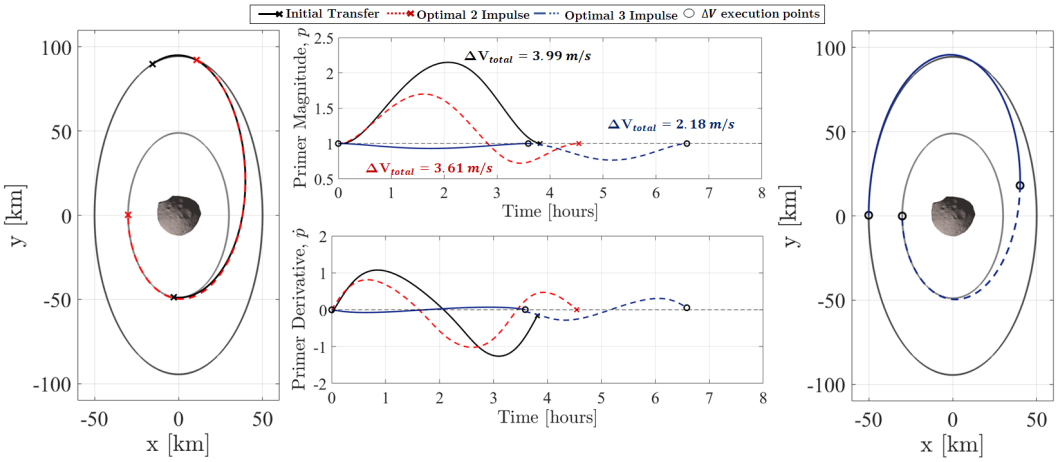

(a) Case 3

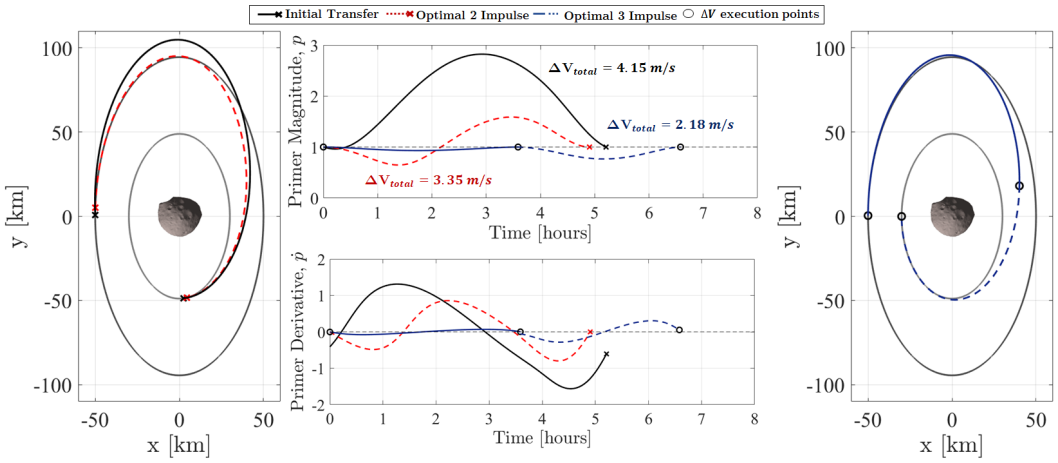

(b) Case 4

Figure 4.19: (a) QSO-M→QSO-La using initial guess from 1:4 MP-QSO transfer map. (b) QSO-M→QSO-La using initial guess from 2:9 MP-QSO transfer map.

To begin the optimization process, firstly, we use the initial conditions from the MP-QSO transfer maps as the first guess of the optimization problem. We allow the departure and arrival points on the relative QSOs to vary across all possible longitudes $\theta = \arctan(-y/x)$ around Phobos and iterate until the cost function ($\Delta V = \Delta V_{Dep} + \Delta V_{Arr}$) is minimized using a sequential quadratic programming (SQP) algorithm using fmincon/SNOPT[102].

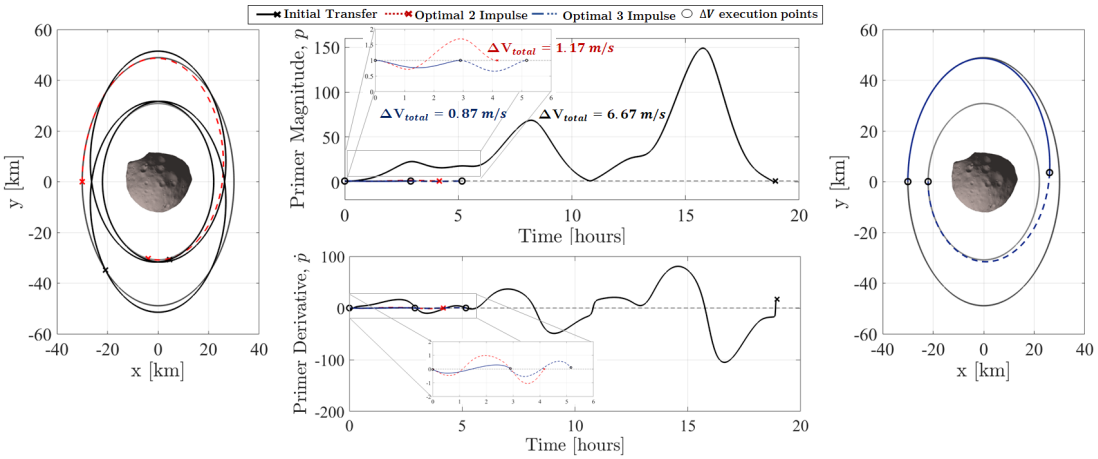

(a) Case 5

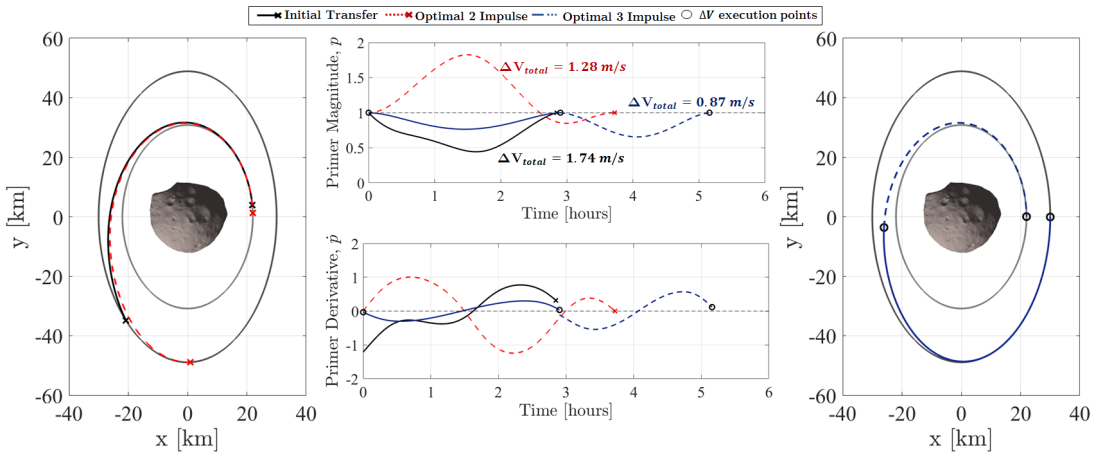

(b) Case 6

Figure 4.20: (a) QSO-La→QSO-Lb using initial guess from 3:10 MP-QSO transfer map. (b) QSO-La→QSO-Lb using initial guess from 1:3 MP-QSO transfer map.

The resulting optimal two-impulse transfer trajectories are plotted in red throughout the transfer cases. On evaluating the primer vector history of these optimal two-impulse

trajectories, we find that most transfer trajectories satisfy the optimality condition on the primer vector derivative. However, the primer vector magnitude is greater than unity, suggesting room for improvement[103]. Therefore, we further introduce a midcourse maneuver ΔV_{Mid} parallel to $\boldsymbol{p}_m$ and time (t_m) when primer vector magnitude is at its maximum (p_{max}). We reoptimize the transfer results utilizing this achieved position and time for midcourse impulse as an initial guess. We find significant changes in the transfer costs and resulting trajectories satisfy the necessary conditions for optimal impulse transfer trajectories.

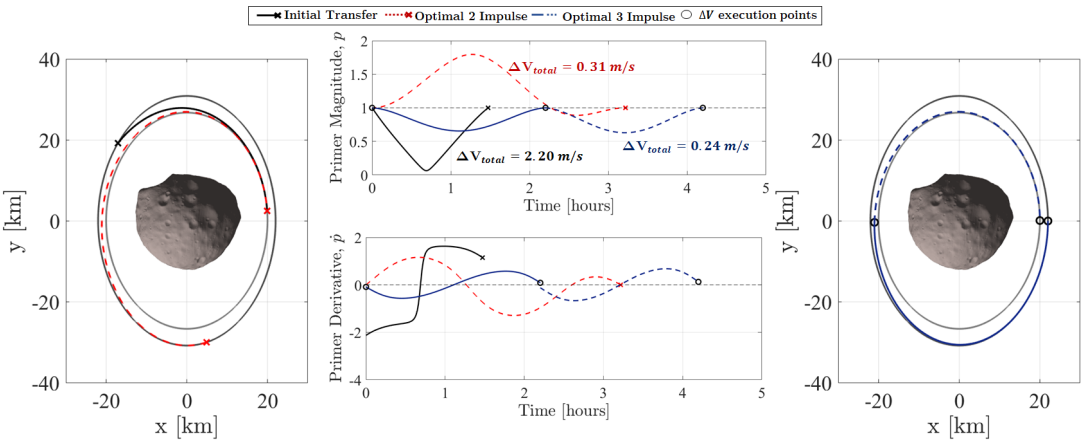

(a) Case 7

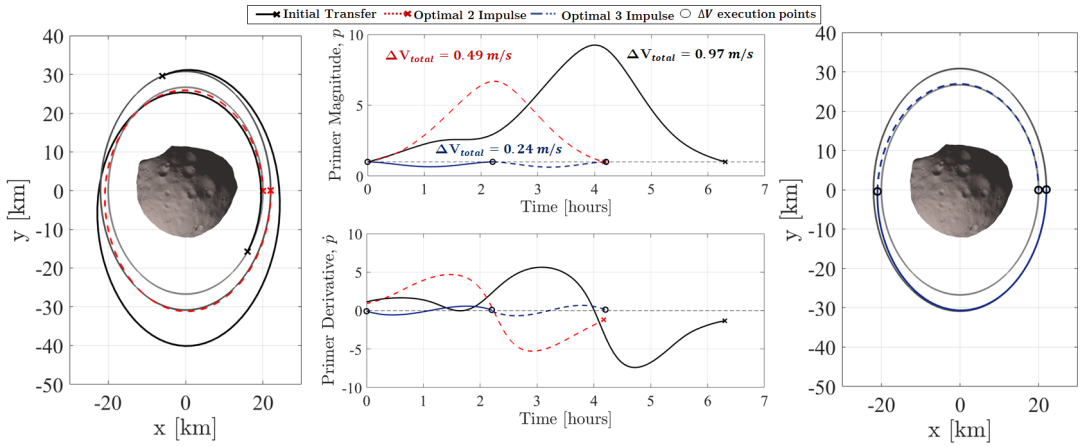

(b) Case 8

Figure 4.21: (a) QSO-Lb→QSO-Lc using initial guess from 1:3 MP-QSO transfer map. (b) QSO-Lb→QSO-Lc using initial guess from 3:8 MP-QSO transfer map.

Fig. 4.18 to 4.21 illustrates our primer vector analysis results obtained for MMX candidate transfer cases listed in Table 4.6. In the case of QSO-H to M transfer cases shown in Fig. 4.18, using the initial guess from 1:7 and 1:10 MP-QSO transfer maps, the ΔV costs of 11.72 m/s and 11.63 m/s are reduced to 5.68 m/s with a midcourse maneuver. We choose the initial guess computed from the 1:4 and 2:9 MP-QSO transfer maps that suggested minimum ΔV transfers for QSO-M to La transfer. As shown in Fig. 4.19, the optimal total ΔV cost of transfers is lowered by ΔV from 4 m/s to 2.18 m/s in cases 3 and 4. Interestingly from Fig. 4.20 and 4.21, it can be noted that transfer cases 6 and 7 using the initial guesses (black) from 1:3 MP-QSO transfer maps suggest that primer vector magnitude is less than unity throughout the transfer. However, while examining the primer vector derivatives at impulse times, they fail to satisfy the optimality condition. In both cases 6 and 7, $\dot{p}_0 < 0$ indicates an earlier impulse time lowering the transfer cost, and $\dot{p}_0 > 0$ suggests an increase in transfer time that could lower the transfer cost. Numerical simulation shows that the increase in overall time of transfer and an earlier impulse reduced the transfer cost of the two-impulse transfers. We note that primer vector magnitude of the two-impulse transfers are not optimal and addition of midcourse impulse reduced the transfer cost. Nevertheless, cases 5 and 8 with initial guesses from 3:10 and 3:8 MP-QSO transfer maps for multi-revolution transfers between QSO-La→QSO-Lb and QSO-Lb→QSO-Lc also suggest that adding a midcourse impulse lowers the total ΔV cost of the respective transfers. The key finding of this analysis is that for all of these transfer cases, the departure and arrival points for optimal three-impulse transfer trajectories are on the same periapsis (periphobian) side. However, this is not the case with two-impulse transfers.

Table 4.7: Transfer Summary

Transfer Case	Optimal 2-impulse		Optimal 3-impulse	
	ΔV m/s	TOF (hours)	ΔV m/s	TOF (hours)
1	9.74	5.04	5.68	7.42
2	9.54	5.12	5.68	7.42
3	3.61	4.54	2.18	6.58
4	3.35	4.9	2.18	6.58
5	1.17	4.16	0.87	5.16
6	1.28	3.72	0.87	5.16
7	0.31	3.21	0.24	1.68
8	0.49	4.17	0.24	1.68

A summary of impulsive transfer cases in the Table 4.7 shows that introducing a midcourse impulse has improved the optimized total ΔV of all the MMX transfer cases. In the case of QSO-H→M transfers, there is a 51% improvement of 6 m/s from the initial guess. Similarly, optimal transfer results of QSO-M→La cases suggest a 47% improvement of the total ΔV costs. On the other hand, we see a significant improvement in total ΔV costs of about 50-86% during QSO-La→Lb transfer and 75-87% improvement in QSO-Lb→Lc transfers.

In conclusion, transfer trajectories via bifurcated families of MP-QSO provide robust and safe transfer between relative QSOs. In contrast, optimal 3-impulse transfer trajectories depart and arrive at the same periphobian side, yield a lower transfer cost for the retrograde transfer orbits. Regarding the operational safety of the actual missions, a 50-80% reduction in the transfer ΔV could be a trade-off for a robust and safer transfer delivered by the proposed MP-QSO transfer method. Moreover, future missions seeking lower-ΔV transfer opportunities between stable retrograde orbits around Phobos or any small irregular planetary satellites in the solar system could use the transfer methodologies and evaluation presented in this thesis.

5 Out-of-plane Transfer Design

5.1 Introduction

In this section, we propose and demonstrate a transfer methodology using the invariant manifolds of the mid-altitude 3D-QSOs(unstable) shown in Fig. 5.1. The main idea is to connect higher-altitude and lower-altitude QSOs that are envisaged for the proximity operations of MMX. Note that several combination of $(d : n)$ exist in the mid-altitude range. For conciseness, we focus on 3D-QSOs with multiplicity $n < 30$ and bifurcations between $A_x \in [45, 55]$ km. This follows from MMX planned operations that envisage flight into a $A_x = 50\ km$ mid-altitude 3D-QSO[20, 104]. The invariant manifolds of a 3D-QSO are computed by perturbing the states along the direction of 3D-QSO's local eigenvectors. Stable and unstable invariant manifolds originating from various regions along the unstable 3D QSOs are characterized using numerical computation on multiple nodes of the periodic 3D QSO. Let $\mathbf{Y}^s(\mathbf{X}_0)$ and $\mathbf{Y}^u(\mathbf{X}_0)$ be the normalized stable and unstable eigenvectors associated with the real pair of eigenvalues of the monodromy matrix, M, evaluated in an arbitrary point $\mathbf{X}_0$.

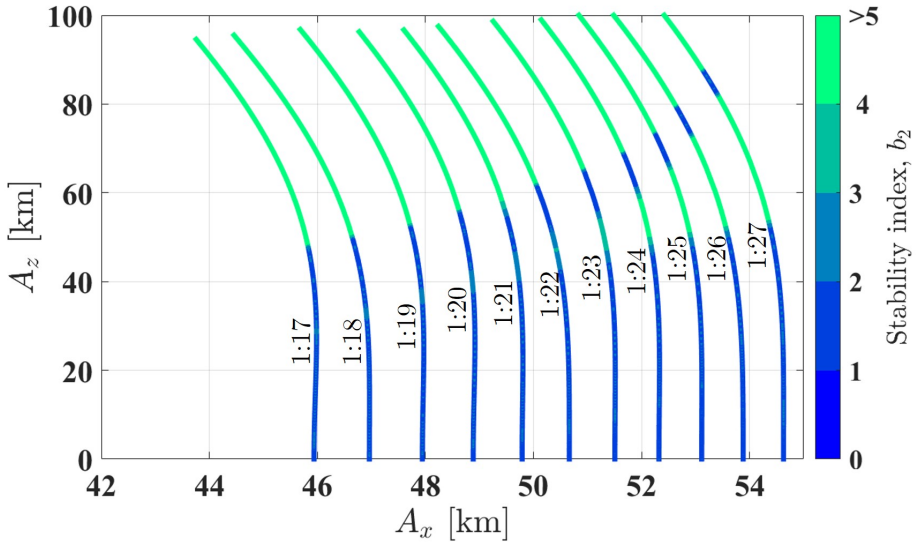

Figure 5.1: A_x vs A_z variations of mid-altitude 3D-QSO families.

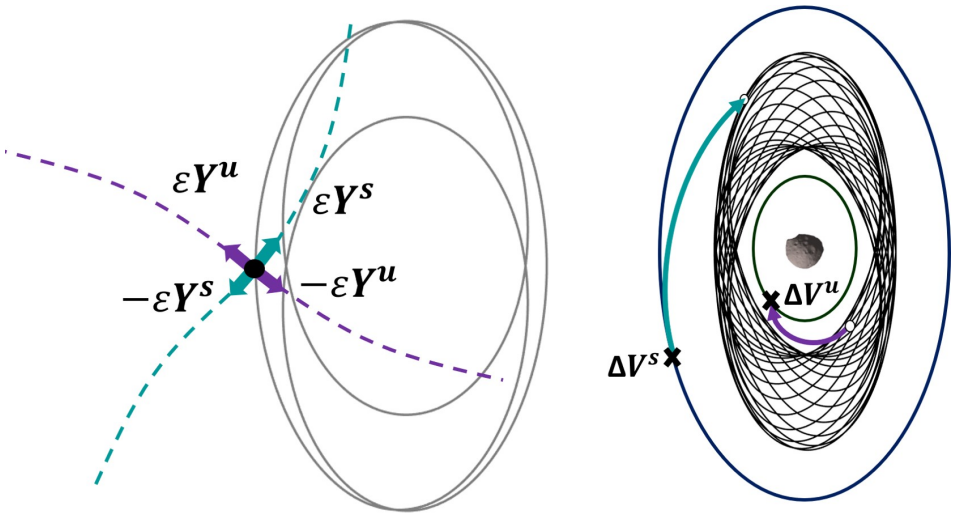

Figure 5.2: Direction of perturbed eigenvectors from a 3D-QSO and transfer method illustration.

Fig. 5.2 (Left) shows the direction of the perturbed normalized stable and unstable eigenvectors from a 3D-QSO. Here, we defined arbitrary points along 3D-QSO equally spaced in time and approximated the computation of stable and unstable manifolds locally. The computation of stable and unstable manifolds associated with an

unstable 3D-QSO can be accomplished using suitable numerical integration procedures [71, 105, 106].

Initial guesses for stable and unstable manifolds are given by

$$\mathbf{X}^s(\mathbf{X}_0) = \mathbf{X}_0 + \varepsilon \mathbf{Y}^s(\mathbf{X}_0) \tag{5.1}$$

$$\mathbf{X}^u(\mathbf{X}_0) = \mathbf{X}_0 + \varepsilon \mathbf{Y}^u(\mathbf{X}_0) \tag{5.2}$$

Where, ε is small displacement from $\mathbf{X}_0$. In this work we have displaced the initial state by $\varepsilon = 1 \times 10^{-4}$. This perturbation should be set numerically as low as possible while designing maneuver-free transfers. Propagating Eq.(5.1) backwards in time, we generate stable manifold trajectories. Similarly, propagating Eq.(5.2) forward in time, we generate unstable manifold trajectories. Small maneuvers are required in realistic mission design implementations to transition from manifold trajectories to 3D-QSO.

In this research, we use the stable eigenvectors in $-\varepsilon \mathbf{Y}^s$ direction and unstable eigenvectors in $-\varepsilon \mathbf{Y}^u$ direction to connect capture and escape trajectories from a high-altitude QSO to low-altitude QSO as illustrated in Fig. 5.2 (Right).

5.2 Transfer Methodology

The computed stable invariant manifolds obtained from the unstable 3D-QSOs will assist in capturing the spacecraft from the planar QSO to the 3D-QSO. Similarly, unstable manifolds from the unstable 3D-QSO will help the spacecraft escape from the 3D-QSO and maneuver towards lower altitude orbits. To demonstrate the transfer methodology, we consider high- and low-altitude QSOs from the MMX baseline orbits, hereby referred to as QSO-H and QSO-L, respectively. Firstly, a 3D-QSO-M (mid-altitude 3D-QSO) of desired A_z is identified. Secondly, we select number of equidistant nodes along the required unstable 3D-QSO-M and compute the local eigenvectors at each nodes to generate capture and escape trajectories. Finally, once stable and unstable manifolds are computed, we connect stable manifolds with QSO-H and unstable manifolds with QSO-L. This transfer procedure requires two transfer stages as illustrated in Figs. 5.3 and 5.4 (Capture to 3D-QSO) and Figs. 5.5 and 5.6 (Escape from 3D-QSO).

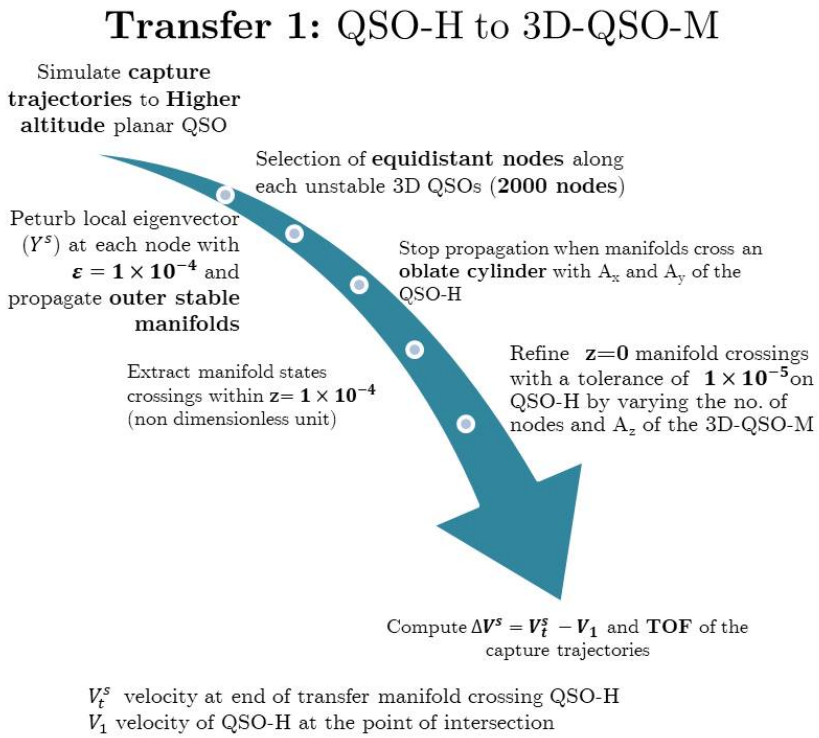

Figure 5.3: Transfer stage 1: Procedure.

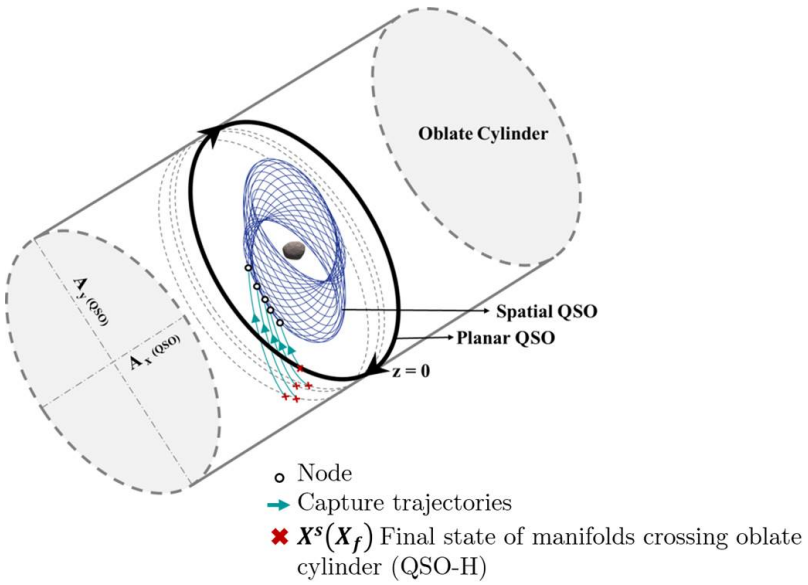

Figure 5.4: Transfer stage 1 illustration showing manifolds extraction from oblate cylinders passing through QSO-H.

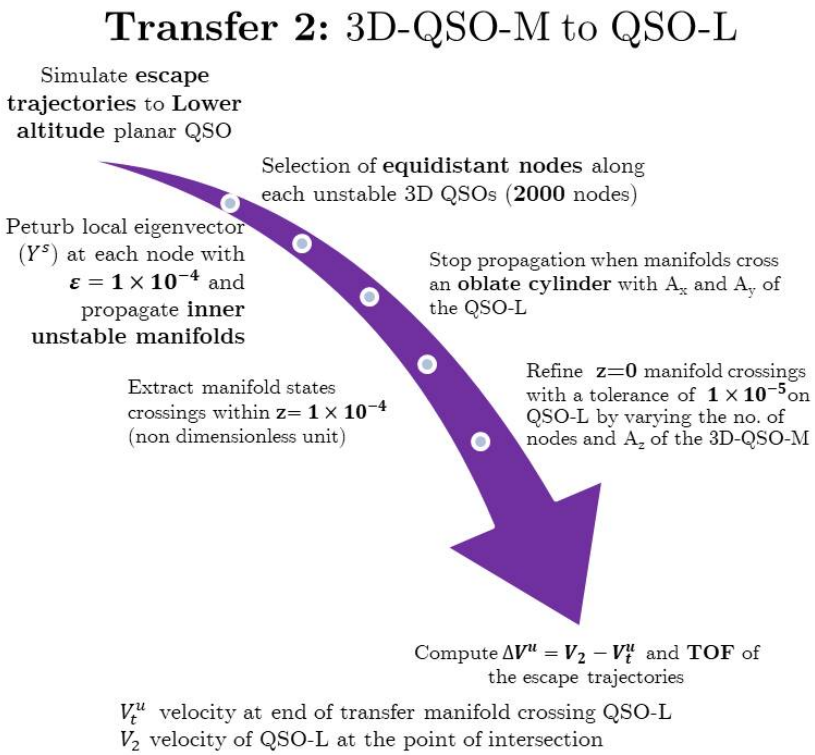

Figure 5.5: Transfer stage 2: Procedure.

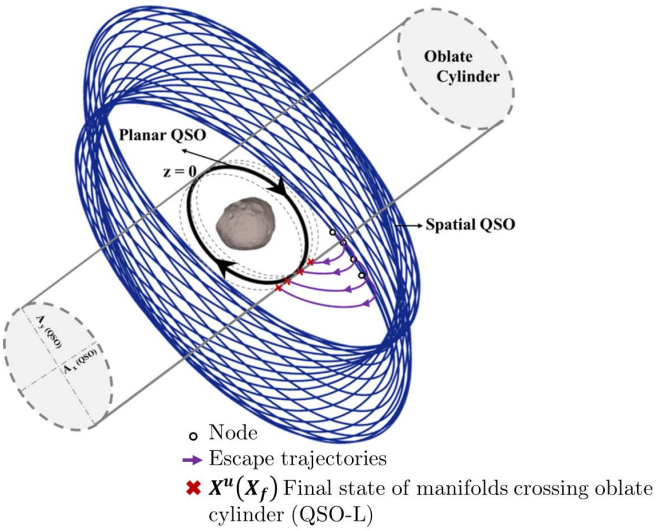

Figure 5.6: Transfer stage 2 illustration showing manifolds extraction from oblate cylinders passing through QSO-L.

The computed stable and unstable manifolds are discontinued during propagation while crossing an oblate cylinder passing through the QSO-H and QSO-L. Capture trajectories are halted when they pass through QSO-H oblate cylinder and these final states are further refined to extract trajectories that intersect QSO-H at $|z| \leq 10^{-5}$. The refined trajectories allow us to calculate the ΔV^s and TOF^s from the departing planar QSO-H. Varying the number of nodes and changing the energy of the 3D-QSO provides better $z = 0$ crossing trajectories and lower ΔV^s. Similarly, escape trajectories from the same 3D-QSO-M are halted when they pass through the QSO-L oblate cylinder and the manifolds intersecting the QSO-L are recorded and extracted further to obtain ΔV^u and TOF^u at arriving planar QSO-L.

5.3 Application to MMX Mission

Due to the significance of observing high-latitude regions of Phobos surface terrain and scientific operations, the MMX mission considers flying into a 3D-QSO around Phobos. Chapter 3 offered several 3D-QSO candidates in the lower and mid-altitude regions of the MMX baseline operational altitudes.

In this section, an application to the MMX mission will be presented followed by a station-keeping analysis for the feasible intermediate 3D-QSOs operations. The high and low altitude QSOs are QSO-H and QSO-La of MMX mission baseline orbits and are then applied to the proposed transfer method.

5.3.1 Transfer 1: QSO-H to 3D-QSO via Capture trajectories

Feasible transfers between QSO-H and 3D-QSO-M are investigated through several cases of mid-altitude 3D-QSO families of different $A_z \in [70, 120]$ km with the proposed transfer methodology. Features of 3D-QSO-M used in this study are tabulated in the Appendix A (Tables A1 to A11). Fig. 5.7 shows the xz-projection of the final states of stable manifolds passing through oblate QSO-H cylinder from different A_z of 1:23 3D-QSOs. As it can be seen, all of these capture trajectories intersect QSO-H at $z = 0$ with ΔV^s and TOF^s as tabulated in Table 5.1. It is found that transfers to 3D-QSOs from the QSO-H exists for almost all the families of mid-altitude 3D-QSOs with $\Delta V^s \in [20, 35]$ m/s and $TOF^s \in [1.93, 36.85]$ days.

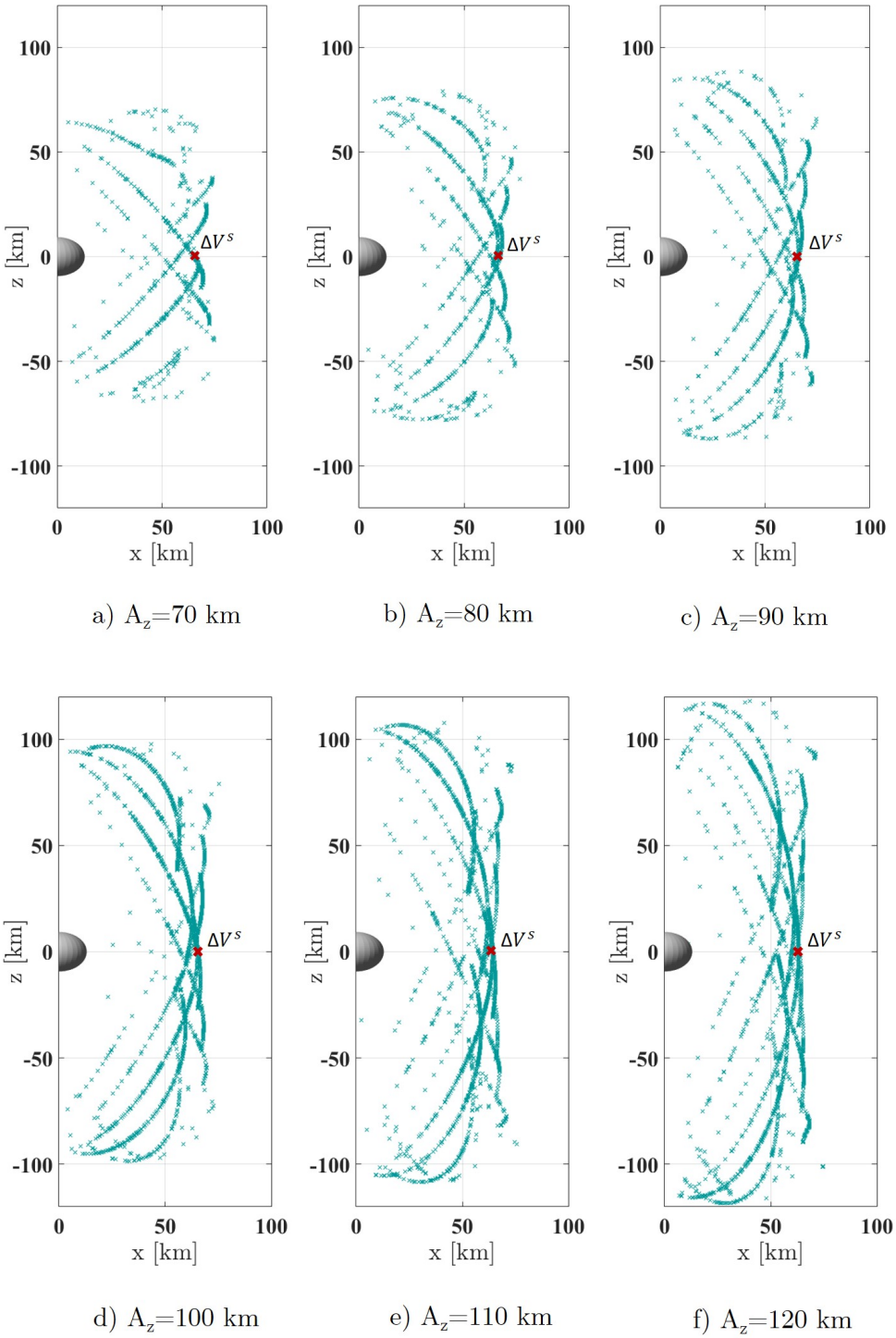

a) A_z=70 km b) A_z=80 km c) A_z=90 km

d) A_z=100 km e) A_z=110 km f) A_z=120 km

Figure 5.7: 1:23 3D-QSO stable manifold crossings at QSO-H (A_x x A_y) oblate cylinder(xz-projection).

Table 5.1: Capture trajectories from QSO-H to 3D-QSO-M.

	$A_z = 70km$		$A_z = 80km$		$A_z = 90km$		$A_z = 100km$		$A_z = 110km$		$A_z = 120km$	
3D-QSO	ΔV^s	TOF^s	ΔV^s	TOF^s	ΔV^s	TOF^s	ΔV^s	TOF^s	ΔV^s	TOF^s	ΔV^s	TOF^s
type	(m/s)	(days)	(m/s)	(days)	(m/s)	(days)	(m/s)	(days)	(m/s)	(days)	(m/s)	(days)
1:17	20.93	4.39	25.31	4.41	26.83	4.16	31.79	4.87	28.99	3.18	34.81	4.65
1:18	22.56	4.67	23.81	3.82	25.58	5.21	27.52	3.49	27.63	3.32	33.22	3.35
1:19	21.34	6.29	25.30	4.23	24.61	5.42	30.67	4.19	32.27	3.76	33.99	4.38
1:20	23.28	8.59	27.20	6.19	23.98	4.08	26.07	3.80	31.09	4.71	29.52	1.93
1:21	21.84	8.15	25.41	5.34	24.62	6.05	26.64	4.03	28.77	3.84	33.76	5.43
1:22	21.01	9.98	27.50	8.39	23.18	4.64	27.30	6.14	29.33	4.13	29.27	3.06
1:23	24.62	14.78	26.15	13.16	26.68	5.04	26.59	6.66	27.82	6.53	30.85	6.36
1:24	18.56	13.08	22.34	10.75	28.46	7.47	25.29	6.90	28.12	6.85	30.35	5.95
1:25	-	-	25.39	11.74	22.92	10.23	28.18	7.37	28.56	5.45	30.69	4.62
1:26	23.18	35.87	25.58	19.55	26.55	11.43	27.35	5.87	29.13	6.53	28.84	5.08
1:27	21.19	36.86	20.76	18.16	22.61	12.89	29.19	8.88	27.68	7.51	31.88	7.82

Table 5.2: Escape trajectories from 3D-QSO-M to QSO-L.

	$A_z = 70km$		$A_z = 80km$		$A_z = 90km$		$A_z = 100km$		$A_z = 110km$		$A_z = 120km$	
3D-QSO	ΔV^u	TOF^u	ΔV^u	TOF^u	ΔV^u	TOF^u	ΔV^u	TOF^u	ΔV^u	TOF^u	ΔV^u	TOF^u
type	(m/s)	(days)	(m/s)	(days)	(m/s)	(days)	(m/s)	(days)	(m/s)	(days)	(m/s)	(days)
1:17	16.11	5.08	19.41	3.46	20.63	3.04	22.88	1.56	26.2	1.53	28.4	1.47
1:18	-	-	18.36	3.64	20.68	3.36	22.99	1.68	-	-	-	-
1:19	-	-	18.48	3.80	20.67	2.45	22.92	3.27	25.19	1.66	27.67	1.74
1:20	-	-	-	-	-	-	22.93	2.69	25.87	1.86	27.48	1.75
1:21	-	-	18.62	4.47	20.72	4.08	22.94	2.07	25.22	3.79	27.55	2.12
1:22	-	-	-	-	-	-	-	-	25.49	2.77	28.03	2.24
1:23	-	-	-	-	-	-	22.99	2.42	25.50	4.04	27.57	3.96
1:24	-	-	-	-	-	-	-	-	25.44	3.15	27.56	4.09
1:25	-	-	-	-	-	-	-	-	25.48	4.64	27.56	4.42
1:26	-	-	-	-	-	-	-	-	25.50	8.09	27.59	4.67
1:27	-	-	-	-	-	-	-	-	-	-	27.59	2.98

5.3.2 Transfer 2: 3D-QSO to QSO-L via Escape trajectories

Similarly to the design of capture trajectories, we apply our transfer technique to detect potential manifold crossings for different families of mid-altitude 3D-QSOs intersecting oblate cylinder passing through QSO-L. The initial states of selected nodes along the mid-altitude 3D-QSOs are perturbed by a small value of ε in $-\varepsilon Y^u$ eigenvector direction allowing the spacecraft to escape 3D-QSO through the unstable manifolds connecting QSO-L. These manifolds passing the oblate QSO-L cylinder are further refined by increasing the number of nodes to extract finer $z = 0$ trajectories and calculate the required ΔV^u and TOF^u to arrive at QSO-L.

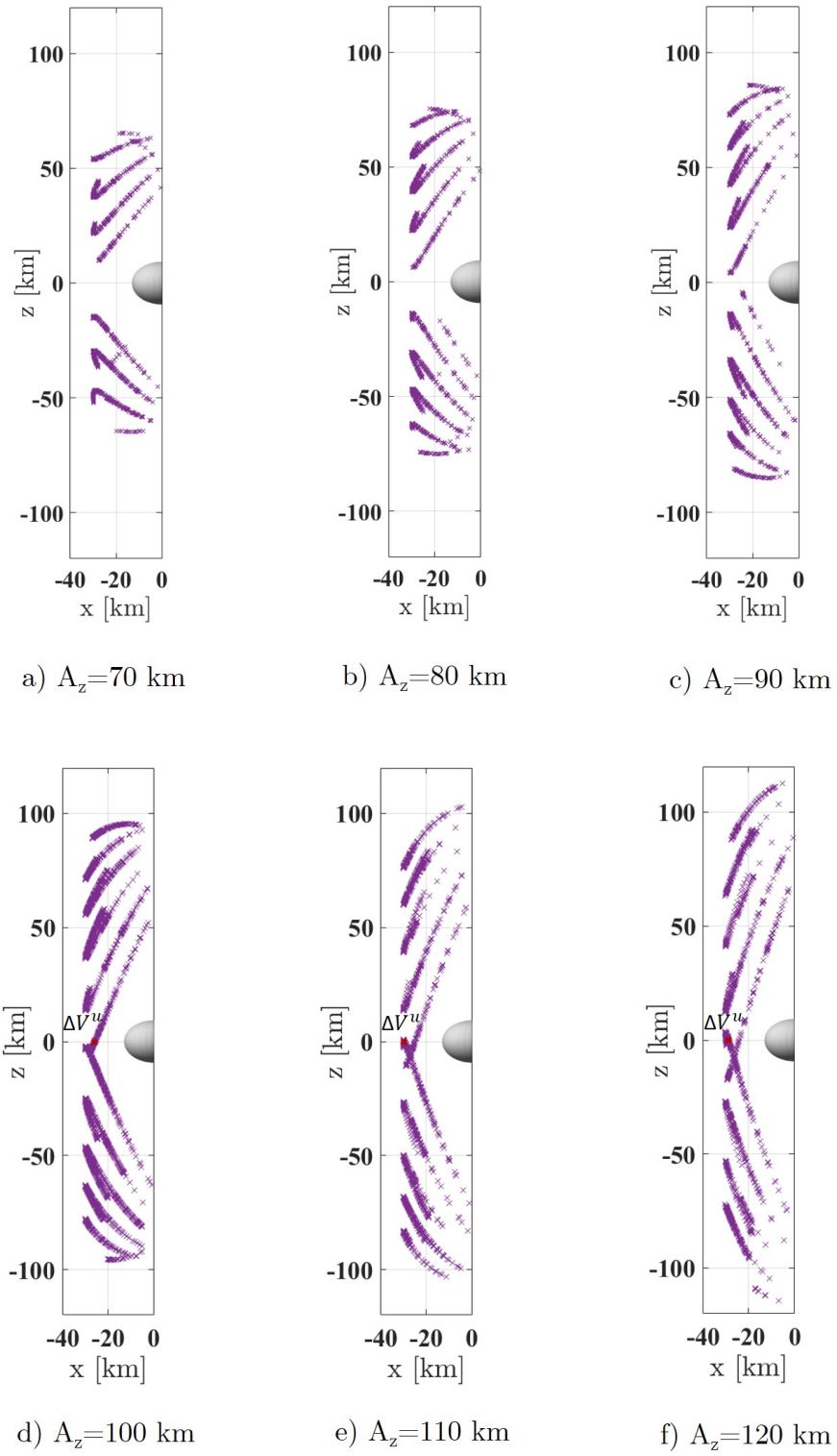

a) A_z=70 km b) A_z=80 km c) A_z=90 km

d) A_z=100 km e) A_z=110 km f) A_z=120 km

Figure 5.8: 1:23 3D-QSO unstable manifold crossings at QSO-L (A_x x A_y) oblate cylinder (xz-projection).

Fig. 5.8 shows the xz-projection of the final states of the unstable manifolds of 1:23 3D-QSO family passing through the oblate QSO-L at different z-amplitudes. Unlike the previous transfer stage, 1:23 3D-QSO at $Az \in [70, 90]$ km does not have any manifolds intersecting QSO-L at $z = 0$. As a result of our numerical analysis, ΔV^u and TOF^u required to arrive QSO-L from various mid-altitude 3D-QSOs are tabulated in Table 5.2 with $\Delta V^u \in [16, 28]$ m/s and $TOF^u \in [1.47, 8.09]$ days.

5.4 Estimating Station-keeping costs of 3D-QSO-M

Combining the results of Tables 5.1 and 5.2 could inform MMX mission designers on 3D-QSOs that would enable optimal transfers (in terms of either ΔV or TOF) between QSO-H and QSO-L. However, such an analysis would not take into consideration the orbit maintenance costs required to operate the spacecraft at higher latitudes and collect precious images for the global coverage of Phobos. Some of the existing orbital maintenance Generally, maintaining the desired spacecraft trajectory is achieved by either exploiting the chaotic dynamics of the three-body problem or through optimal control methods[107]. To better inform the selection of baseline 3D-QSOs, an orbital maintenance approach that suppresses and eliminates the growth of the relative error along the unstable eigenvector of a 3D-QSO has been implemented. Nakamiya and Kawakatsu [108] used this approach to estimate orbital maintenance of Halo orbits in the Sun-Earth system to eliminate unstable components under thrusting constraints.

Following the Hamiltonian nature of the system Eq.(2.7), the eigenvalues of the monodromy matrix, M, must occur in reciprocal pairs. In the case of 3D-QSOs, the unstable eigenvalues (λ_1) cause neighboring trajectories to diverge from the desired periodic path. As a result, impulsive maneuvers should be implemented to nullify the exponential growth of the relative error.

Let $\delta\mathbf{X_{err}}$ be a vector of initial deviations from the reference trajectory at time $t = 0$

$$\delta\mathbf{X_{err}} = [\delta x_{err}, \delta y_{err}, \delta z_{err}, \delta \dot{x}_{err}, \delta \dot{y}_{err}, \delta \dot{z}_{err}]^T \tag{5.3}$$

and $\Delta\mathbf{V}_{cm}$ be an impulsive maneuver that needs to be implemented at the same time.

$$\Delta\mathbf{V}_{cm} = [\Delta\dot{x}, \Delta\dot{y}, \Delta\dot{z}]^T \tag{5.4}$$

After one orbital period, the initial deviation vector,

$$\delta\mathbf{X_{t=0}} = \delta\mathbf{X_{err}} + \Delta\mathbf{V}_{cm} = \begin{pmatrix} 0 + \delta x_{err} \\ 0 + \delta y_{err} \\ 0 + \delta z_{err} \\ \Delta\dot{x} + \delta\dot{x}_{err} \\ \Delta\dot{y} + \delta\dot{y}_{err} \\ \Delta\dot{z} + \delta\dot{z}_{err} \end{pmatrix}, \tag{5.5}$$

is mapped forward in time by the monodromy matrix M:

$$\delta\mathbf{X_{t=T}} = M\delta\mathbf{X_{t=0}}. \tag{5.6}$$

If $U = [\overrightarrow{e_1}, \overrightarrow{e_2}, \overrightarrow{e_3}, \overrightarrow{e_4}, \overrightarrow{e_5}, \overrightarrow{e_6}]$ is a coordinate transformation such that M would be transformed into its Jordan canonical form, i.e.,

$$\Lambda = \begin{pmatrix} \lambda & 0 & 0 & 0 & 0 & 0 \\ 0 & 1/\lambda & 0 & 0 & 0 & 0 \\ 0 & 0 & \sigma & \rho & 0 & 0 \\ 0 & 0 & -\rho & \sigma & 0 & 0 \\ 0 & 0 & 0 & 0 & 1 & 1 \\ 0 & 0 & 0 & 0 & 0 & 1 \end{pmatrix} = U^{-1}\, M\, U, \tag{5.7}$$

where λ is real and greater than 1, Eq.(5.6) can be rewritten as

$$\delta\mathbf{Z}_{t=T} = \Lambda\, \delta\mathbf{Z}_{t=0}, \tag{5.8}$$

where $\delta\mathbf{Z} = \begin{pmatrix} a, & b, & c, & d, & e, & f \end{pmatrix}^T = U^{-1}\, \delta\mathbf{X}$. Accordingly, one can choose a suppressive maneuver $\Delta\mathbf{V}_{cm}$ such that

$$a_{t=T} = \lambda\, \mathbf{q}^T\, (\delta\mathbf{X}_{err} + \Delta\mathbf{V}_{cm}) = 0, \tag{5.9}$$

thus preventing the initial deviation $\delta\mathbf{X}_{err}$ to grow large along the unstable manifold of the periodic orbit. Here, $\boldsymbol{q} = \begin{pmatrix} \mathbf{q}_r^T, \mathbf{q}_v^T \end{pmatrix}^T$ is a six-dimensional vector whose components correspond to the first row of U^{-1}.

Its definition allow us to simplify Eq.(5.9) in

$$a_{err} + v_{cm}\, \mathbf{q}_v^T\, \hat{\mathbf{e}}_V = 0 \tag{5.10}$$

where

$$a_{err} = \mathbf{q}^T\, \delta\mathbf{X}_{err}, \tag{5.11}$$

v_{cm} is the magnitude of the impulsive maneuver, and $\hat{\mathbf{e}}_V$ is a three-dimensional unit vector aligned with the direction of the burn, i.e., $\Delta\mathbf{V}_{cm} = v_{cm}\, \hat{\mathbf{e}}_V$.

It is easy to minimize v_{cm} subject to the constraint Eq.(5.10) and obtain an analytical expression for the magnitude of the suppressive burn as in Eq.(5.12):

$$v_{cm} = \frac{a_{err}}{\|\mathbf{q}_v\|}. \tag{5.12}$$

As expected, the magnitude of the suppressive maneuver varies linearly with the projection of the initial deviation vector $\delta\mathbf{X}_{err}$ along $\mathbf{q}$.

In the following, we estimate the orbit maintenance costs of a 3D-QSO by considering the preliminary orbit injection errors of MMX as provided by the MMX flight dynamics team. It is assumed that these initial errors are distributed according to zero-mean Gaussian distributions with standard deviations as reported in Table 5.3. Given the Gaussian distribution of $\delta\boldsymbol{X}_{err}$, we can obtain an analytical expression for the standard deviation of a_{err} according to Eq.(5.11). Specifically, if $\mathbb{E}[\cdot]$ is the expected value operator, and

$$P_{err} = \mathbb{E}[\delta\mathbf{X}_{err}\, \delta\mathbf{X}_{err}^T] = \begin{pmatrix} \sigma_x^2 & 0 & 0 & 0 & 0 & 0 \\ 0 & \sigma_y^2 & 0 & 0 & 0 & 0 \\ 0 & 0 & \sigma_z^2 & 0 & 0 & 0 \\ 0 & 0 & 0 & \sigma_{\dot{x}}^2 & 0 & 0 \\ 0 & 0 & 0 & 0 & \sigma_{\dot{y}}^2 & 0 \\ 0 & 0 & 0 & 0 & 0 & \sigma_{\dot{z}}^2 \end{pmatrix} \tag{5.13}$$

is the covariance matrix in Cartesian coordinates, then

$$\sigma_{a_{err}}^2 = \mathbf{q}^T\, P_{err}\, \mathbf{q}. \tag{5.14}$$

Table 5.3: MMX Injection Errors

Standard Deviation	Value	Unit
σ_x	100	m
σ_y	100	m
σ_z	100	m
$\sigma_{\dot{x}}$	3	cm/s
$\sigma_{\dot{y}}$	3	cm/s
$\sigma_{\dot{z}}$	3	cm/s

Similarly,

$$\sigma^2_{v_{cm}} = \frac{\sigma^2_{a_{err}}}{||\mathbf{q}_v||^2} \tag{5.15}$$

Table 5.4 reports the 3σ values of v_{cm} extrapolated over a period of 30 days, i.e., the duration of the envisioned MMX operations in a mid-altitude 3D-QSO [20], assuming that a maneuver will have to be implemented every day due to execution errors and mismodelled dynamics. We highlight that the 3σ values of v_{cm} would depend on the location of the spacecraft along the candidate 3D-QSO and typically vary by a few cm/s. Such a difference is considered negligible for the purposes of this crude station-keeping approximation and not included in the final values of Table 5.4. Under the assumptions of our numerical simulation, it appears that the orbital maintenance cost for the 1:27 3D-QSO with $A_z = 120\ km$ is the cheapest among the candidate orbit, with an estimated maximum v_{cm} cost of 0.584 m/s for 30 days. In contrast, the most expensive orbit turned out to be the 1:17 3D-QSO ($A_z = 70\ km$) with a total v_{cm} cost of 0.937 m/s per month. All of the 3D-QSOs have orbital maintenance costs below 1 m/s per month, resulting in a plethora of valid candidate orbits for the global coverage of Phobos. This analysis suggests that the orbit maintenance costs of 3D-QSOs may play a minor role in driving the selection of an optimal staging orbit for transfers between high-altitude and low-altitude orbits around Phobos. This is further investigated in the following Section, where capture and escape trajectory costs are combined to identify the most suitable candidate orbits for out-of-plane operations.

Table 5.4: Orbital maintenance cost of 3D-QSO-M for 30 days

3D-QSO type	$A_z = 70km$ v_{cm} (m/s)	$A_z = 80km$ v_{cm} (m/s)	$A_z = 90km$ v_{cm} (m/s)	$A_z = 100km$ v_{cm} (m/s)	$A_z = 110km$ v_{cm} (m/s)	$A_z = 120km$ v_{cm} (m/s)
1:17	0.9376	0.9320	0.9283	0.9249	0.9219	0.9190
1:18	0.8860	0.8827	0.8798	0.8773	0.8750	0.8729
1:19	0.8395	0.8371	0.8349	0.8329	0.8311	0.8295
1:20	0.7972	0.7954	0.7936	0.7921	0.7906	0.7869
1:21	0.7586	0.7572	0.7558	0.7546	0.7534	0.7522
1:22	0.7235	0.7224	0.7212	0.7202	0.7191	0.7182
1:23	0.6913	0.6904	0.6895	0.6886	0.6877	0.6869
1:24	0.6617	0.6611	0.6600	0.6595	0.6588	0.6581
1:25	-	0.6341	0.6334	0.6327	0.6322	0.6314
1:26	0.6094	0.6090	0.6086	0.6086	0.6079	0.6068
1:27	0.5862	0.5859	0.5856	0.5850	0.5845	0.5840

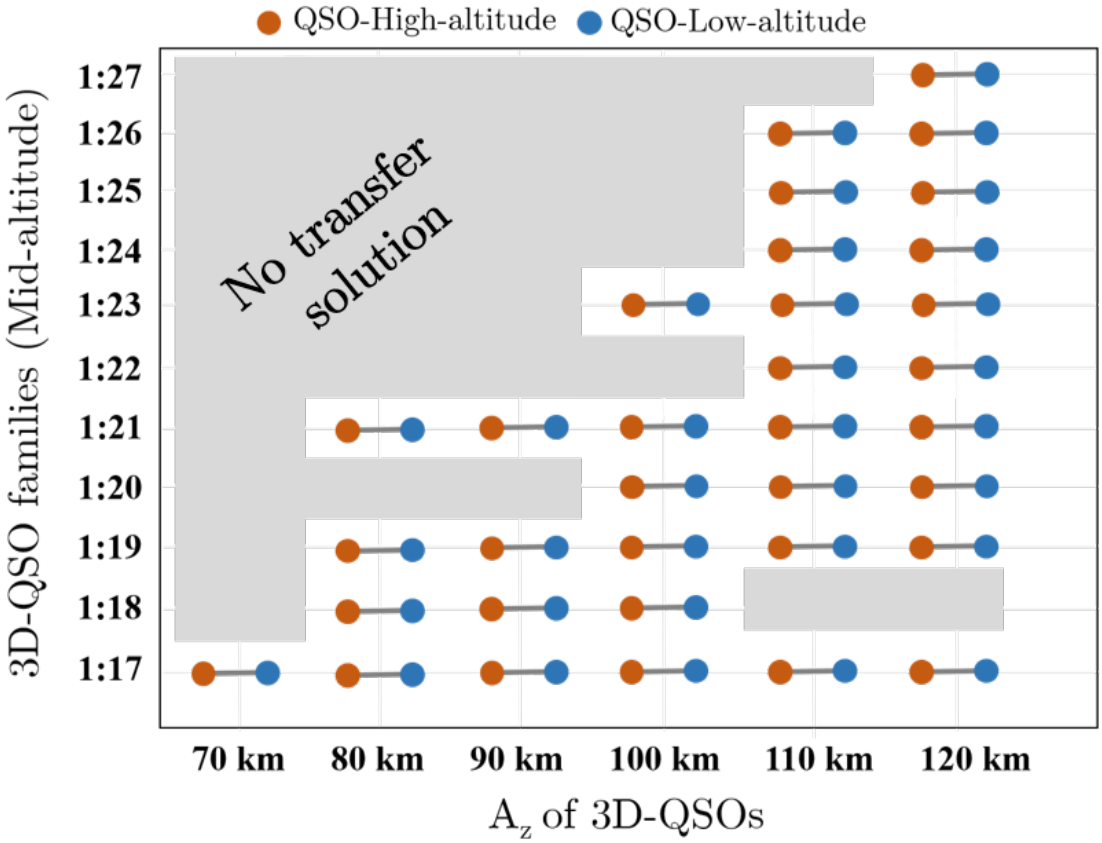

Figure 5.9: Overall transfer solution space connecting QSO-H and QSO-L.

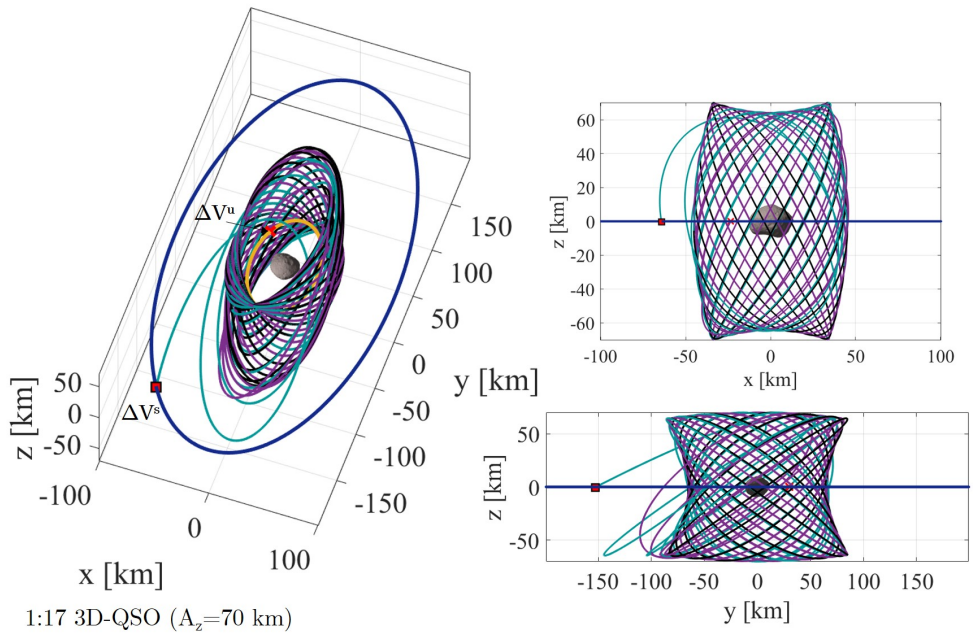

Figure 5.10: Minimum ΔV^t transfer between QSO-H to QSO-L via 3D-QSO-M. [ΔV^t= 37.04 m/s; TOF^t= 9.47 days]

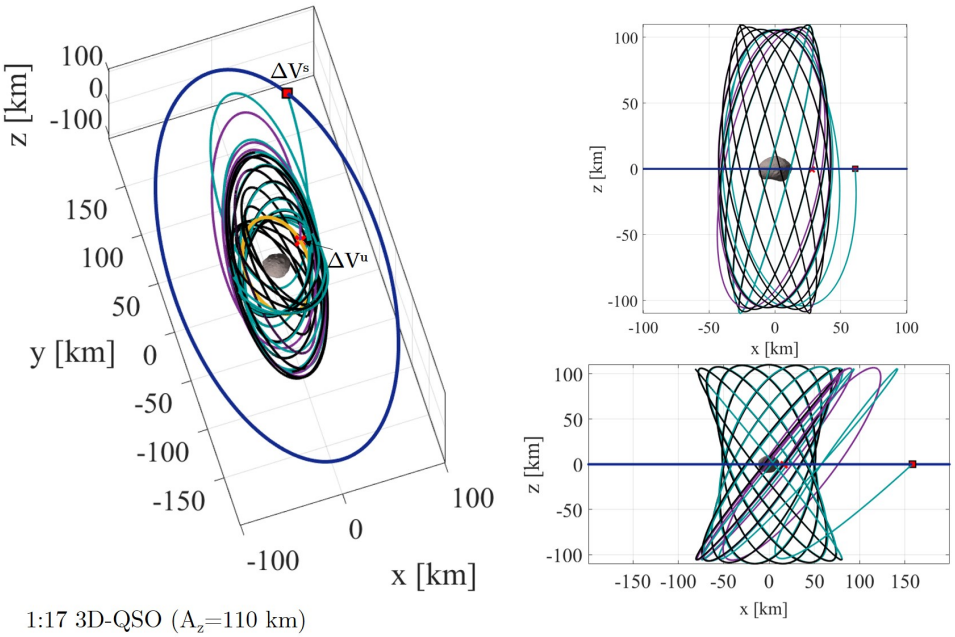

Figure 5.11: Minimum TOF^t transfer between QSO-H to QSO-L via 3D-QSO-M. [ΔV^t= 55.19 m/s; TOF^t= 4.70 days]

5.5 Results and discussions

In this section, we present the overall transfer analysis by combining the capture and escape trajectories obtained from the numerical simulations of Section 4. From Tables 5.1 and 5.2, we find several possible combinations of transfers via different families of 3D-QSOs at various energies. The overall solution space involving both the capture and escape phases connecting QSO-H and QSO-L is presented in Fig. 5.9. Interestingly, we find that the 1:17 3D-QSO family connects both QSO-H and QSO-L at all the considered values of $A_z \in [70, 120]$ km. Conversely, 1:27 3D-QSOs only permit transfer between high-altitude and low-altitude regions when $A_z = 120$ km. The minimum overall $\Delta V^t (\Delta V^s + \Delta V^u)$ and $TOF^t (TOF^s + TOF^u)$ transfer solution cases are shown in Fig. 5.10 and 5.11, respectively.

Table 5.5: Transfer cost for high-latitude coverage with 3D-QSOs

Transfer stage	Transfers via MP-QSOs min ΔV_{total}	Transfers via 3D-QSOs min ΔV_{total}	Difference min ΔV_{total}
QSO-H → QSO-La	21 m/s	37.97 m/s	16.97 m/s

By comparison with our previous investigation where only planar transfers had been considered [50], we conclude that 17 m/s of additional ΔV would be required for the MMX spacecraft to be inserted into a mid-altitude 3D-QSO and enable the detailed observations of the high-latitude regions of Phobos (Table 5.5). These intermediate 3D-QSOs are weakly to highly unstable and require additional station-keeping costs as highlighted in Section 5.

Table 5.6: Overall transfer and station-keeping cost of mid-altitude 3D-QSOs.

3D-QSO type	$A_z = 70km$ $\Delta V^t + v_{cm}$ (m/s)	$A_z = 80km$ $\Delta V^t + v_{cm}$ (m/s)	$A_z = 90km$ $\Delta V^t + v_{cm}$ (m/s)	$A_z = 100km$ $\Delta V^t + v_{cm}$ (m/s)	$A_z = 110km$ $\Delta V^t + v_{cm}$ (m/s)	$A_z = 120km$ $\Delta V^t + v_{cm}$ (m/s)
1:17	37.9737	45.6521	48.3913	55.5928	56.1084	64.1348
1:18	-	43.0563	47.1362	51.3869	-	-
1:19	-	44.6213	46.1121	54.4268	58.2922	62.4881
1:20	-	-	-	49.7909	57.7606	57.7867
1:21	-	44.7911	46.0979	50.3316	54.7476	62.0658
1:22	-	-	-	-	55.5314	58.0145
1:23	-	-	-	50.2637	54.0058	59.1082
1:24	-	-	-	-	54.2276	58.5609
1:25	-	-	-	-	54.6675	58.8815
1:26	-	-	-	-	55.2409	57.0393
1:27	-	-	-	-	-	60.0596

The results of our orbital maintenance analysis, combined with the results of Tables 5.1 and 5.2 are presented in Table 5.6 and shown only for those candidate orbits where transfer from/to QSO-H/QSO-L is permitted. It appears that the 1:17 3D-QSO with $A_z = 70\ km$ would have the cheapest overall transfer and station-keeping cost of 37.973 m/s. This is in sharp contrast with the 64.134 m/s ΔV cost observed for the same family at $A_z = 120\ km$. It can also be noted how the total ΔV cost of the transfer tends to increase for higher values of A_z, thus suggesting a mission trade-off of a few m/s of propellant per degree of maximum latitude achievable on Phobos.

6

Conclusions and Future work

This thesis investigates the utilization of bifurcated families of retrograde orbits to develop and design novel transfer trajectories connecting planar and spatial quasi-satellite orbits in the vicinity of Phobos. This work explicitly leverages the in-plane and out-of-plane period-multiplying bifurcations of the stable planar QSO family to connect relative retrograde orbits around Phobos in the Mars-Phobos Hill Problem with ellipsoidal gravity secondary framework.

This thesis began by reviewing some of the tools available in Dynamical Systems Theory for computing periodic orbits, analyzing stability, and bifurcations in preparation for numerical investigations. These preliminaries are helpful to introduce some of the fundamental terminologies that recurred throughout the thesis and lay the foundation for the numerical procedures of Chapter 3 and the development of transfer design methods presented in Chapters 4 and 5.

Chapter 3 of this work dealt with numerical procedures and systematic computation of period-multiplying bifurcated families of QSOs. More specifically, this thesis exploited the vertical and horizontal bifurcations caused due to the change in stability

indices at some resonant ratios from the planar QSO family solution. In-plane and out-of-plane bifurcated families are categorized as MP-QSOs and 3D-QSOs. By studying these bifurcated retrograde families of orbits, it was observed that varying amplitude of MP-QSOs is ideal for connecting several planar QSOs. Whereas 3D-QSOs aids in high-latitude coverage of the Phobos' surface.

Geometrical features of in-plane bifurcated MP-QSOs are further exploited to develop a novel transfer technique for a robust and safer transfer of the spacecraft in the vicinity of Phobos in Chapter 4. Specifically, MP-QSOs that bifurcate from the planar solutions and intersect both initial and final planar QSOs are identified. Later, the registered ΔV and time-of-flight values at multiple departing and arrival intersection points are evaluated using transfer maps between departing and arriving longitudes. This transfer analysis was applied to baseline QSOs in the proximity phase operations of the MMX mission. In particular, transfer maps between MMX candidate QSOs are disclosed to elucidate the transfer problem and identified minimum ΔV and TOF opportunities. By comparison with previous direct transfer results, it is found that the total transfer cost between the MMX baseline QSOs may be minimized by using MP-QSO families that intersect the departing and arrival orbits almost tangentially and with the highest possible value of the Jacobi integral. Such a conclusion contributes in several ways to our understanding of the dynamical environment around Phobos, and provide a basis for the selection of transfer ΔV execution points. In addition, this work's findings served as a more accurate initial guess for further optimization of the transfer problem. The primer vector analysis of the impulse transfer trajectories revealed that the optimal impulse solution exists only while departure and arrival ΔV execution points are at the same periphobian sides with an additional mid-course impulse.

In Chapter 5, an out-of-plane transfer strategy to insert the spacecraft into a 3D-QSO utilizing the stable and unstable manifolds emanating from unstable solutions of bifurcated out-of-plane orbits was proposed. The feasibility of connecting high-altitude and low-altitude QSOs via cheap transfer opportunities were later explored. To design an out-of-plane transfer, firstly, the desired arrival and departing QSOs are identified. This work used the MMX baseline QSOs and demonstrated the transfer strategy. Once the baseline high-low altitude QSOs are fixed, intersection of capture and escape trajectories propagated from different locations along candidate 3D-QSOs with oblate

cylinders passing through the planar orbits are then evaluated. Later the trajectories crossing the planar orbits are extracted by optimizing the number of nodes and ΔV and *TOF* for the transfer cases are calculated. This out-of-plane transfer technique provided us with a baseline to estimate the costs and time-of-flights associated with ballistic dynamics between high-altitude and low-altitude QSOs. To further narrow the design space of mid-altitude out-of-plane trajectories, a simple orbit maintenance strategy was implemented to nullify the growth of orbit injection errors along the unstable eigenvectors of candidate 3D-QSOs. The final candidates are ranked based on MMX scientific requirements, transfer analyses, and station-keeping costs. It is found that intermediate 3D-QSOs can be maintained with as little as 1 m/s per month. As a result of this investigation, it was found that transfers from high-altitude to low-altitude regions around Phobos would be possible via intermediate 1:17 3D-QSOs that demands a minimum ΔV cost of 37.973 m/s and a minimum time of flight of less than 5 days.

6.1 Recommendations for Future Research

This work's findings could serve as initial guesses for real-ephemeris implementations to be adopted for the actual MMX mission design. The transfer methodologies and analysis presented in this work can be extended for any future missions that seek lower ΔV transfer opportunities between stable retrograde orbits around Phobos or any small irregular planetary satellites in the solar system.

The identified transfer trajectories can be improved further using appropriate optimization techniques that would allow us to simulate and account for more-realistic dynamics and engineering constraints. In particular, introducing two bifurcated families of QSOs as transfer orbit for a three-impulse robust transfer can potentially minimize the total transfer cost and aid in safer transfer. Future research should focus on developing guidance and control laws that effectively mitigate the effects of navigation, perturbation and missed thrust errors during the transfers.

Appendices

Appendix A

Specifications of mid-altitude 3D-QSOs are tabulated in Tables A1 to A11.

Table A1: 1:17 3D-QSO

A_z	A_xxA_y (km)	C	b_2	T (days)
70 km	45.15x85.39	-5.371	906.34	5.038
80 km	44.65x84.67	-6.576	3307.6	5.048
90 km	44.05x83.73	-7.967	9350.67	5.056
100 km	43.39x82.63	-9.515	21710.05	5.063
110 km	42.65x81.35	-11.289	44735.28	5.069
120 km	41.86x79.96	-13.249	82287.09	5.074

Table A2: 1:18 3D-QSO

A_z	A_xxA_y (km)	C	b_2	T (days)
70 km	45.94x87.42	-5.422	751.38	5.355
80 km	45.43x86.70	-6.609	3045.57	5.365
90 km	44.82x85.76	-7.994	9292.02	5.374
100 km	44.13x84.63	-9.57	23108.35	5.381
110 km	43.39x83.35	-11.337	49377.18	5.387
120 km	42.61x81.97	-13.291	93596.54	5.392

Table A3: 1:19 3D-QSO

A_z	A_xxA_y (km)	C	b_2	T (days)
70 km	47.16x89.64	-5.484	572.19	5.673
80 km	46.69x88.94	-6.678	2670.5	5.683
90 km	46.12x88.63	-8.051	8705.01	5.692
100 km	45.42x86.93	-9.623	22798.28	5.699
110 km	44.73x85.67	-11.384	50552.69	5.705
120 km	43.96x84.3	-13.333	98768.61	5.71

Table A4: 1:20 3D-QSO

A_z	A_xxA_y (km)	C	b_2	T (days)
70 km	48.17x91.52	-5.557	399.82	5.991
80 km	47.72x90.82	-6.733	2128.47	6.001
90 km	47.16x89.90	-8.112	7613.75	6.01
100 km	46.52x88.80	-9.672	20944.81	6.017
110 km	45.81x87.54	-11.43	48334.03	6.023
120 km	45.64x86.17	-13.376	97443.73	6.028

Table A5: 1:21 3D-QSO

A_z	A_xxA_y (km)	C	b_2	T (days)
70 km	49.02x93.55	-5.624	244.67	6.309
80 km	48.56x92.88	-6.801	1578.75	6.319
90 km	48.61x91.98	-8.167	6161.52	6.328
100 km	47.37x90.90	-9.726	18016.79	6.335
110 km	46.67x89.67	-11.479	43328.2	6.341
120 km	45.91x88.31	-13.42	90112.77	6.347

Table A6: 1:22 3D-QSO

A_z	A_xxA_y (km)	C	b_2	T (days)
70 km	49.74x95.31	-5.694	126.4	6.627
80 km	49.27x94.62	-6.862	1049.28	6.637
90 km	48.71x93.74	-8.221	4589.68	6.646
100 km	48.07x92.66	-9.777	14394.05	6.653
110 km	47.36x91.42	-11.529	36260.72	6.66
120 km	46.59x90.07	-13.465	77878.35	6.665

Table A7: 1:23 3D-QSO

A_z	A_xxA_y (km)	C	b_2	T (days)
70 km	50.73x97.17	-5.793	53.48	6.945
80 km	50.32x96.53	-6.916	604.29	6.955
90 km	49.78x95.66	-8.276	3106.37	6.964
100 km	49.15x94.59	-9.849	10713.43	6.971
110 km	48.46x93.38	-11.594	28266.11	6.978
120 km	47.71x92.04	-13.53	62874.75	6.983

Table A8: 1:24 3D-QSO

A_z	A_xxA_y (km)	C	b_2	T (days)
70 km	51.57x98.78	-5.941	15.32	7.264
80 km	51.20x98.19	-6.976	285.71	7.273
90 km	50.68x97.32	-8.333	1848.08	7.285
100 km	50.07x96.26	-9.811	6986.68	7.29
110 km	49.39x95.05	-11.62	19647.98	7.296
120 km	48.65x93.71	-13.554	45622.47	7.301

Table A9: 1:25 3D-QSO

A_z	A_xxA_y (km)	C	b_2	T (days)
70 km	-	-	-	-
80 km	51.95x99.96	-7.043	91.68	7.591
90 km	51.44x99.12	-8.387	894.38	7.6
100 km	50.84x98.09	-9.931	3958.5	7.608
110 km	50.16x96.89	-11.67	12091.8	7.613
120 km	49.42x95.57	-13.595	29419.15	7.62

Table A10: 1:26 3D-QSO

A_z	A_xxA_y (km)	C	b_2	T (days)
70 km	53.02x102.15	-5.982	8.16	7.9
80 km	52.59x101.50	-7.13	7.16	7.91
90 km	52.08x100.68	-8.444	290.73	7.918
100 km	51.48x99.64	-9.985	1738.24	7.926
110 km	50.80x98.46	-11.717	6017.82	7.932
120 km	50.06x97.13	-13.638	15673.02	7.938

Table A11: 1:27 3D-QSO

A_z	A_xxA_y (km)	C	b_2	T (days)
70 km	53.88x103.80	-6.054	29.33	8.218
80 km	53.49x103.18	-7.191	8.41	8.228
90 km	52.99x102.35	-8.515	22.64	8.237
100 km	52.41x101.36	-10.036	416.74	8.244
110 km	51.75x100.18	-11.764	1944.19	8.251
120 km	51.03x98.88	-13.683	5760.89	8.256

Bibliography

[1] Burns, J. A., "The dynamical evolution and origin of the Martian moons," *Vistas in Astronomy*, Vol. 22, 1978, pp. 193–210.

[2] Basilevsky, A., Lorenz, C., Shingareva, T., Head, J., Ramsley, K., and Zubarev, A., "The surface geology and geomorphology of Phobos," *Planetary and Space Science*, Vol. 102, 2014, pp. 95–118.

[3] Singer, S. F., "The Origin of the Moon and Geophysical Consequences*," *Geophysical Journal International*, Vol. 15, No. 1-2, 1968, pp. 205–226.

[4] Murchie, S. L., Britt, D. T., Head, J. W., Pratt, S. F., Fisher, P. C., Zhukov, B. S., Kuzmin, A. A., Ksanfomality, L. V., Zharkov, A. V., Nikitin, G. E., Fanale, F. P., Blaney, D. L., Bell, J. F., and Robinson, M. S., "Color heterogeneity of the surface of Phobos: relationships to geologic features and comparison to meteorite analogs." *Journal of Geophysical Research*, Vol. 96, 1991, pp. 5925–5945.

[5] Hunten, D. M., "Capture of Phobos and Deimos by photoatmospheric drag," *Icarus*, Vol. 37, No. 1, 1979, pp. 113–123.

[6] Pajola, M., Lazzarin, M., Dalle Ore, C. M., Cruikshank, D. P., Roush, T. L., Magrin, S., Bertini, I., La Forgia, F., and Barbieri, C., "Phobos as a D-type Captured Asteroid, Spectral Modeling from 0.25 to 4.0 μm," *The Astrophysical Journal*, Vol. 777, No. 2, 2013.

[7] Citron, R. I., Genda, H., and Ida, S., "Formation of Phobos and Deimos via a giant impact," *Icarus*, Vol. 252, 5 2015, pp. 334–338. 10.1016/J.ICARUS.2015.02.011.

[8] Rosenblatt, P., Charnoz, S., Dunseath, K. M., Terao-Dunseath, M., Trinh, A., Hyodo, R., Genda, H., and Toupin, S., "Accretion of Phobos and Deimos in an extended debris disc stirred by transient moons," *Nature Geoscience*, Vol. 9, No. 8, 2016, pp. 581–583.

[9] Pratt, W. and Hopkins, J., "Comparison of Deimos and Phobos as Destinations for Human Exploration and Identification of Preferred Landing Sites," AIAA SPACE Forum, American Institute of Aeronautics and Astronautics, Sep 2011.

[10] Murchie, S. L., Britt, D. T., and Pieters, C. M., "The value of Phobos sample return," *Planetary and Space Science*, Vol. 102, 2014, pp. 176–182.

[11] Sagdeev, R. Z. and Zakharov, A. V., "Brief history of the Phobos mission," *Nature*, Vol. 341, No. 6243, 1989, pp. 581–585.

[12] Marov, M. Y., Avduevsky, V. S., Akim, E. L., Eneev, T. M., Kremnev, R. S., Kulikov, S. D., Pichkhadze, K. M., Popov, G. A., and Rogovsky, G. N., "Phobos-Grunt: Russian sample return mission," *Advances in Space Research*, Vol. 33, 2004, pp. 2276–2280.

[13] Marov, M. Y., "Phobos-Soil space project: A new stage of the Russian planetary program," *Solar System Research*, Vol. 44, No. 1, 2010, pp. 1–4.

[14] Kawakatsu, Y., Kuramoto, K., Ogawa, N., Ikeda, H., Ono, G., Sawada, H., Imada, T., Otsuki, M., Otake, H., Muller, R., Zacny, K., Satoh, Y., Yamada, K., Mary, S., Grebenstein, M., and Yoshikawa, K., "Mission definition of Martian Moons exploration (MMX)," *70th International Astronautical Congress*, Washington D.C, USA, October 2019.

[15] Lee, P., Bicay, M., Colaprete, A., Elphic, R., Genova, A., Hine, B., Horanyi, M., Jaroux, B., Korsmeyer, D., Lewis, B. S., Worden, P., Ames, N., and Field, M., "Phobos And Deimos Mars Environment (PADME): A LADEE-Derived Mission to Explore Mars Moons and the Martian Orbital Environment." *45th Lunar and Planetary Science Conference*, Texas, USA, 2014.

[16] Murchie, S. L., Chabot, N. L., Buczkowski, D. L., Eng, D. A., Peplowski, P. N., Ernst, C. M., Seelos, F. P., Horanyi, M., Castillo-Rogez, J. C., Chmielewski, A. B.,

Maki, J. N., Trebi-Ollenu, A., Ehlmann, B. L., Klingelhoefer, G., Arvidson, R. E., Spence, H. E., and Christian, J. A., "Mars-Moons Exploration, Reconnaissance, and Landed Investigation (MERLIN)," *2016 IEEE Aerospace Conference*, 2016, pp. 1–18. 10.1109/AERO.2016.7500754.

[17] Prettyman, T. H., Diniega, S., and Raymond, C. A., "PANDORA - Unlocking the mysteries of the Moons of Mars," *AAS/Division for Planetary Sciences Meeting Abstracts*, Vol. 46, Arizona, USA, 2014.

[18] Oberst, J., Wickhusen, K., Willner, K., Gwinner, K., Spiridonova, S., Kahle, R., Coates, A., Herique, A., Plettemeier, D., Díaz-Michelena, M., Zakharov, A., Futaana, Y., Pätzold, M., Rosenblatt, P., Lawrence, D. J., Lainey, V., Gibbings, A., and Gerth, I., "DePhine – The Deimos and Phobos Interior Explorer," *Advances in Space Research*, Vol. 62, No. 8, 2018, pp. 2220–2238.

[19] Koschny, D., Svedhem, H., and Rebuffat, D., "Phootprint - A Phobos sample return mission study," *40th COSPAR Scientific Assembly*, Vol. 40, Jan. 2014.

[20] Kawakatsu, Y., Kuramoto, K., Usui, T., Ikeda, H., Yoshikawa, K., Sawada, H., Ozaki, N., Imada, T., Otake, H., Maki, K., Otsuki, M., Muller, R., Zacny, K., Satoh, Y., Mary, S., Grebenstein, M., Tokaji, A., Yuying, L., Franquesa, F., Pushparaj, N., and Chikazawa, T., "System definition of Martian Moons Exploration (MMX)," *71st International Astronautical Congress*, October 2020.

[21] Usui, T., Kuramoto, K., and Kawakatsu, Y., "Martian Moons eXploration (MMX): Japanese Phobos Sample Return Mission," *42nd COSPAR Scientific Assembly*, Vol. 42, California, USA, July 2018.

[22] Kuramoto, K., Kawakatsu, Y., and Fujimoto, M., "Martian Moons eXploration (MMX) : an overview of its science," *European Planetary Science Congress*, Berlin, Germany, Sept. 2018.

[23] Fujiya, W., Furukawa, Y., Sugahara, H., Koike, M., Bajo, K.-i., Chabot, N. L., Miura, Y. N., Moynier, F., Russell, S. S., Tachibana, S., Takano, Y., Usui, T., and Zolensky, M. E., "Analytical protocols for Phobos regolith samples returned by the Martian Moons eXploration (MMX) mission," *Earth, Planets and Space*, Vol. 73, No. 1, 2021, pp. 120.

[24] Scheeres, D. J., wal, S. V., Olikara, Z., and Baresi, N., "Dynamics in the Phobos environment," *Advances in Space Research*, Vol. 63, 1 2019, pp. 476–495.

[25] Jackson, J., "Retrograde Satellite Orbits," *Monthly Notices of the Royal Astronomical Society*, Vol. 74, No. 2, 1913, pp. 62–82.

[26] Benest, D., "Effects of the mass ratio on the existence of retrograde satellites in the circular restricted problem." *Astronomy and Astrophysics*, Vol. 32, 1974, pp. 39–46.

[27] Benest, D., "Effects of the mass ratio on the existence of retrograde satellites in the circular restricted problem. II," *Astronomy and Astrophysics*, Vol. 45, No. 2, 1975, pp. 353–363.

[28] Benest, D., "Effects of the mass ratio on the existence of retrograde satellites in the circular restricted problem. III," *Astronomy and Astrophysics*, Vol. 53, No. 2, 1976, pp. 231–236.

[29] Benest, D., "Effects of the mass ratio on the existence of retrograde satellites in the circular restricted problem. IV. Three-dimensional stability of plane periodic orbits." *Astronomy and Astrophysics*, Vol. 54, No. 2, 1977, pp. 563–568.

[30] Hénon, M., "Numerical exploration of the restricted problem, V," *Astronomy and Astrophysics*, Vol. 1, 1969, pp. 223–238.

[31] Hénon, M., "Vertical Stability of Periodic Orbits in the Restricted Problem. I. Equal Masses," *Astronomy and Astrophysics*, Vol. 28, 1973, pp. 415.

[32] Hénon, M., "Vertical Stability of Periodic Orbits in the Restricted Problem. II. Hill's Case," *Astronomy and Astrophysics*, Vol. 30, 1974, pp. 317.

[33] Wiesel, W. E., "Stable orbits about the Martian moons," *Journal of Guidance, Control, and Dynamics*, Vol. 16, 1993, pp. 434–440.

[34] Mikkola, S., Innanen, K., Wiegert, P., Connors, M., and Brasser, R., "Stability limits for the quasi-satellite orbit," *Monthly Notices of the Royal Astronomical Society*, Vol. 369, No. 1, 2006, pp. 15–24.

[35] Zamaro, M. and Biggs, J. D., "Natural motion around the Martian moon Phobos: the dynamical substitutes of the Libration Point Orbits in an elliptic three-body problem with gravity harmonics," *Celestial Mechanics and Dynamical Astronomy*, Vol. 122, 2015, pp. 263–302.

[36] Zamaro, M. and Biggs, J. D., "Identification of new orbits to enable future mission opportunities for the human exploration of the Martian moon Phobos," *Acta Astronautica*, Vol. 119, 2016, pp. 160–182.

[37] Scott, C. J. and Spencer, D. B., "Transfers to sticky distant retrograde orbits," *Journal of Guidance, Control, and Dynamics*, Vol. 33, 2010, pp. 1940–1946. 10.2514/1.47792.

[38] Scott, C. and Spencer, D., "Stability Mapping of Distant Retrograde Orbits and Transports in the Circular Restricted Three-Body Problem," 2012, pp. 1–21. 10.2514/6.2008-6431.

[39] Capdevila, L., Guzzetti, D., and Howell, K., "Various transfer options from Earth into Distant Retrograde Orbits in the vicinity of the Moon," *Advances in the Astronautical Sciences*, Vol. 152, 2014, pp. 3659–3678.

[40] Mingotti, G., Topputo, F., and Bernelli-Zazzera, F., "Transfers to distant periodic orbits around the Moon via their invariant manifolds," *Acta Astronautica*, Vol. 79, 2012, pp. 20–32.

[41] Demeyer, J. and Gurfil, P., "Transfer to Distant Retrograde Orbits Using Manifold Theory," *Journal of Guidance, Control, and Dynamics*, Vol. 30, No. 5, 2007, pp. 1261–1267.

[42] Oshima, K. and Yanao, T., "Spatial unstable periodic quasi-satellite orbits and their applications to spacecraft trajectories," *Celestial Mechanics and Dynamical Astronomy*, Vol. 131, No. 6, 2019, pp. 23.

[43] Ming, X. and Shijie, X., "Exploration of distant retrograde orbits around Moon," *Acta Astronautica*, Vol. 65, 9 2009, pp. 853–860.

[44] Parrish, N.L., P. J. S. H. S. and Heiligers, M., "Low-thrust transfers from distant retrograde orbits to L2 halo orbits in the earth-moon system," *6th International Conference on Astrodynamics Tools and Techniques*, Darmstadt, Germany, March 2016.

[45] Lam, T. and Whiffen, G. J., "Exploration of distant retrograde orbits around Europa," *15th AAS/AIAA Space Flight Mechanics Meeting*, Colorado, USA, January 2005.

[46] Lam, T., Hirani, A., and Kangas, J., "Characteristics of transfers to and captures at Europa," *16th AAS/AIAA Space Flight Mechanics Meeting*, Florida, USA, January 2006.

[47] Russell, R. P., "Primer vector theory applied to global low-thrust trade studies," *Journal of Guidance, Control, and Dynamics*, Vol. 30, 2007, pp. 460–472.

[48] Ichinomiya, K., Baresi, N., Kawakatsu, Y., and Yanao, T., "Quasi-satellite orbit transfers via multi-revolutional periodic orbits," *29th AAS/AIAA Space Flight Mechanics Meeting*, Hawaii, USA, January 2019.

[49] Canalias, E. Lorda, L. and Hekma, E., "Transfers Between Planar and Three-Dimensional Quasi Satellite Orbits in the Vicinity of Phobos," *29th AAS/AIAA Space Flight Mechanics Meeting*, Hawaii, USA, January 2019.

[50] Pushparaj, N., Baresi, N., Ichinomiya, K., and Kawakatsu, Y., "Transfers around Phobos via bifurcated retrograde orbits: Applications to Martian Moons eXploration mission," *Acta Astronautica*, Vol. 181, 2021, pp. 70–80.

[51] Pushparaj, N., Baresi, N., and Kawakatsu, Y., "Transfers and orbital maintenance of spatial retrograde orbits for Phobos exploration," *Acta Astronautica*, Vol. 189, 2021, pp. 452–464.

[52] Robin, I. and Markellos, V., "Numerical determination of three-dimensional periodic orbits generated from vertical self-resonant satellite orbits," *Celestial Mechanics*, Vol. 21, No. 4, 1980, pp. 395–434.

[53] Lara, M., Russell, R., and Villac, B., "Classification of the distant stability regions at Europa," *Journal of Guidance, Control, and Dynamics*, Vol. 30, 2007, pp. 409–418.

[54] Vaquero, M. and Howell, K. C., "Design of transfer trajectories between resonant orbits in the Earth-Moon restricted problem," *Acta Astronautica*, Vol. 94, 2014, pp. 302–317.

[55] Chen, H., Canalias, E., Hestroffer, D., and Hou, X., "Effective stability of quasi-satellite orbits in the spatial problem for phobos exploration," *Journal of Guidance, Control, and Dynamics*, Vol. 43, 2020, pp. 2309–2320. 10.2514/1.G004911.

[56] Szebehely, V. and Grebenikov, E., "Theory of Orbits-The Restricted Problem of Three Bodies." *Soviet Astronomy*, Vol. 13, Oct. 1969, pp. 364.

[57] Scheeres, D. J., *Orbital motion in strongly perturbed environments: Applications to asteroid and Comet Orbiters*, Springer, 2014.

[58] MacMillan, W. D., *The theory of the potential*, McGraw-Hill Book Company, inc., New York, 1930.

[59] Scheeres, D. J., "Dynamics about Uniformly Rotating Triaxial Ellipsoids: Applications to Asteroids," *Icarus*, Vol. 110, 1994, pp. 225–238.

[60] Willner, K., Shi, X., and Oberst, J., "Phobos' shape and topography models," *Planetary and Space Science*, Vol. 102, 2014, pp. 51–59.

[61] Press, W. H., Teukolsky, S. A., Vetterling, W. T., and Flannery, B. P., *Numerical recipes : the art of scientific computing*, Cambridge University Press, 2007.

[62] Doedel, E. J., "AUTO: a program for the automatic bifurcation analysis of autonomous systems," *Congressus Numerantium*, Vol. 30, 1981, pp. 265–284.

[63] Doedel, E., Keller, H. B., and Kernrvez, J., "Numerical Analysis and Control of Bifurcation Problems (II): Bifurcation in Infinite dimensions," *International Journal of Bifurcation and Chaos*, Vol. 01, No. 04, 1991, pp. 745–772.

[64] Seydel, R., *Practical Bifurcation and Stability Analysis*, Springer Science Business Media, 2009.

[65] Mittelmann, H. D., "A Pseudo-Arclength Continuation Method for Nonlinear Eigenvalue Problems," *SIAM Journal on Numerical Analysis*, Vol. 23, 10 1986, pp. 1007–1016.

[66] Yuying, L., Pushparaj, N., Kawakatsu, Y., and Fujimoto, M., "Point-to-Point Jumping Dynamics on Phobos by Prograde Orbit Families," *AAS/AIAA Astrodynamics Specialist Conference*, 2020.

[67] Howell, K. C., "Three-dimensional, Periodic, 'Halo' Orbits," *Celestial Mechanics*, Vol. 32, 1984, pp. 53–71.

[68] Broucke, R., "Stability of periodic orbits in the elliptic, restricted three-body problem," *AIAA Journal*, Vol. 7, 1969, pp. 1003–1009.

[69] Breakwell, J. and Brown, J., "The 'halo' family of 3-dimensional periodic orbits in the restricted3-body problem," Vol. 20, 1976, pp. 389–404.

[70] Bray, T. A. and Goudas, C. L., "Doubly symmetric orbits about the collinear Lagrangian points," *Astronomical Journal*, Vol. 72, March 1967, pp. 202.

[71] Koon, W. S., Lo, M. W., Marsden, J. E., and Ross, S. D., *Dynamical Systems, the Three-Body Problem and Space Mission Design*, Marsden Books, Wellington, 2011.

[72] Campbell, E. T., *Bifurcations from families of periodic solutions in the circular restricted problem with application to trajectory design*, Ph.D. thesis, Purdue University, Jan. 1999.

[73] Hénon, M., "Exploration numérique du problème restreint. II. Masses égales, stabilité des orbites périodiques," *Annales d'Astrophysique*, Vol. 128, 1965, pp. 992.

[74] Davoust, E. and Broucke, R., "A manifold of periodic orbits in the planar general three-body problem with equal masses," *Astronomy and Astrophysics*, Vol. 112, 1982, pp. 305–320.

[75] Canalias, E., Lorda, L., and Laurent-Varin, J., "Design of Realistic Trajectories for the Exploration of Phobos," *AAS/AIAA Space Flight Mechanics Meeting*, Florida, USA, 2018.

[76] Ikeda, H., Mitani, S., Mimasu, Y., Ono, G., Nigo, K., and Kawakatsu, Y., "Orbital Operations Strategy in the Vicinity of Phobos," *ISTS/ISSFD*, Ehime, Japan, 2017.

[77] Pousse, A., Robutel, P., and Vienne, A., "On the co-orbital motion in the planar restricted three-body problem: the quasi-satellite motion revisited," *Celestial Mechanics and Dynamical Astronomy*, Vol. 128, No. 4, 2017, pp. 383–407.

[78] Clohessy, R. S. and Wiltshire, "The Clohessy-Wiltshire Equations of Relative Motion," *Journal of Aerospace Sciences*, Vol. 27, 1960, pp. 653–658.

[79] Kogan, A., "Distant satellite orbits in the restricted circular three-body problem," *Cosmic Research*, Vol. 24, 1989, pp. 705–710.

[80] Lidov, M. and Vashkov'yak, M., "Perturbation theory and analysis of the evolution of quasi-satellite orbits in the restricted three-body problem," *Cosmic Research*, Vol. 31, 1993, pp. 187–207.

[81] Lidov, M. L. and Vashkov'yak, M. A., "On quasi-satellite orbits in a restricted elliptic three-body problem," *Astronomy Letters*, Vol. 20, No. 5, 1994, pp. 676–690.

[82] Lara, M., "Design of distant retrograde orbits based on a higher order analytical solutiont," *Acta Astronautica*, Vol. 161, 2019, pp. 562–578.

[83] Baresi, N., Dei Tos, D., Ikeda, H., and Kawakatsu, Y., "Trajectory design and maintenance of the martian moons exploration mission around phobos," *Journal of Guidance, Control, and Dynamics*, Vol. 44, 2020, pp. 996–1007.

[84] Baresi, N., *Spacecraft Formation Flight on Quasi-Periodic Invariant Tori*, Ph.D. thesis, University of Colorado Boulder, 2017.

[85] Cabral, F., "On the Stability of Quasi-Satellite Orbits in the Elliptic Restricted Three-Body Problem," *Masters Thesis, Universidade T´ecnica de Lisboa*, 2011.

[86] Canalias, E., Lorda, L., Martin, T., Laurent-Varin, J., Charles, J. B., Marty, and Mimasu, Y., "Trajectory analysis for the Phobos proximity phase of the MMX mission," *International Symposium on Space Technology and Science, ISTS/ISSFD*, Ehime, Japan, June 2017.

[87] Russell, R. P., "Global search for planar and three-dimensional periodic orbits near Europa," *Advances in the Astronautical Sciences*, Vol. 123 I, 2006, pp. 647–672.

[88] Villac, B. F., *Dynamics in the Hill problem with applications to spacecraft maneuvers*, Ph.D. thesis, University of Michigan, 2003.

[89] Lawrence, D. J., Peplowski, P. N., Beck, A. W., Burks, M. T., Chabot, N. L., Cully, M. J., Elphic, R. C., Ernst, C. M., Fix, S., Goldsten, J. O., Hoffer, E. M., Kusano, H., Murchie, S. L., Schratz, B. C., Usui, T., and Yokley, Z. W., "Measuring the Elemental Composition of Phobos: The Mars-moon Exploration with GAmma rays and NEutrons (MEGANE) Investigation for the Martian Moons eXploration (MMX) Mission," *Earth and Space Science*, Vol. 6, No. 12, 2019.

[90] Lawden, D. F., *Optimal Trajectories for Space Navigation*, Butterworths, London, 1963.

[91] Prussing, J. E., *Optimal Spacecraft Trajectories*, Oxford University Press, 2017.

[92] Bokelmann, K. and Russell, R., "Optimization of Impulsive Europa Capture Trajectories using Primer Vector Theory," *Journal of the Astronautical Sciences*, Vol. 67, No. 2, 2020, pp. 485–510.

[93] Carter, T. E., "Necessary and sufficient conditions for optimal impulsive rendezvous with linear equations of motion," *Dynamics and Control*, Vol. 10, No. 3, 2000, pp. 219–227.

[94] Lion, P. M. and Handelsman, M., "Primer vector on fixed-time impulsive trajectories," *AIAA Journal*, Vol. 6, No. 1, 1968, pp. 127–132.

[95] Jezewski, D. J. and Rozendaal, H. L., "An efficient method for calculating optimal free-space n-impulse trajectories," *AIAA Journal*, Vol. 6, No. 11, 1968, pp. 2160–2165.

[96] Glandorf, D. R., "Lagrange multipliers and the state transition matrix for coasing arcs," *AIAA Journal*, Vol. 7, No. 2, 1969.

[97] Batin, R. H., *An Introduction to the Mathematics and Methods of Astrodynamics*, Revised Edition, AIAA Education Series, New York, 1997.

[98] Betts, J. T., *Practical Methods for Optimal Control and Estimation Using Nonlinear Programming, Second Edition*, Society for Industrial and Applied Mathematics, 2010.

[99] Jezewski, D. J., "Primer vector theory applied to the linear relative-motion equations," *Optimal Control Applications and Methods*, Vol. 1, No. 4, 1980, pp. 387–401.

[100] Eckel, K. G., "Optimal impulsive transfer with time constraint," *Acta Astronautica*, Vol. 9, No. 3, 1982, pp. 139–146.

[101] Iorfida, E., Palmer, P. L., and Roberts, M., "A Hamiltonian approach to the planar optimization of mid-course corrections," *Celestial Mechanics and Dynamical Astronomy*, Vol. 124, No. 4, 2016, pp. 367–383.

[102] Gill, P. E., Murray, W., and Saunders, M. A., "SNOPT: An SQP Algorithm for Large-Scale Constrained Optimization," *SIAM Rev.*, Vol. 47, No. 1, Jan. 2005, pp. 99–131.

[103] Damario, L. A. and Edelbaum, T. N., "Minimum impulse three-body trajectories," *AIAA Journal*, Vol. 12, No. 4, 1974, pp. 455–462.

[104] Baresi, N., Dell'Elce, L., Cardoso dos Santos, J., and Kawakatsu, Y., "Long-term evolution of mid-altitude quasi-satellite orbits," *Nonlinear Dynamics*, Vol. 99, No. 4, 2020, pp. 2743–2763.

[105] Pushparaj, N., Baresi, N., and Kawakatsu, Y., "Transfers around phobos using invariant manifolds of unstable quasi-satellite orbits," *71st International Astronautical Congress*, October 2020.

[106] Pushparaj, N., Baresi, N., and Kawakatsu, Y., "Design of transfer trajectories between planar and spatial quasi-satellite orbits," *AIAA Scitech 2020 Forum*, Florida, USA, 2020.

[107] Shirobokov, M., Trofimov, S., and Ovchinnikov, M., "Survey of Station-Keeping Techniques for Libration Point Orbits," *Journal of Guidance, Control, and Dynamics*, Vol. 40, No. 5, 2017, pp. 1085–1105.

[108] Nakamiya, M. and Kawakatsu, Y., "Maintenance of halo orbits under the thrusting constraints," *Journal of Guidance, Control, and Dynamics*, Vol. 35, 2012, pp. 1224–1229.